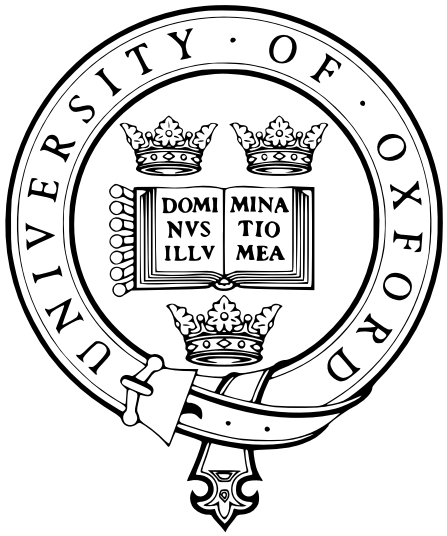
Droplet-Based Microfluidics as a Novel Method of Magnetic Field Effect Detection Associated with Avian Navigation

Laurynas Paškevičius

St Hilda's College
University of Oxford



A Thesis submitted for the degree of
Master of Science by Research

Physical and Theoretical Chemistry Laboratory
South Parks Road, Oxford
October 23, 2024

“Visi mes iš ateities ir dar į ją sugrįšim."

Žygimantas Kudirka, *Open House Vilnius*, 2021

Abstract

Each year, millions of migratory songbirds embark on long-distance seasonal migrations, navigating and orientating their flight across the globe with remarkable precision using the Earth's magnetic field as their guide [1–5]. Studies suggest that there exists a light-driven magnetic compass located in the retinas of migratory birds, which relies on the spin dynamics of photoinduced radical pairs (RPs) in the photoreceptor flavoprotein cryptochrome (Cry) [6–11]. Experimentally, the applications of magnetic fields on Cry RPs have been shown to reduce the efficiency of the interconversion between the singlet and triplet spin states [12–14] — referred to as magnetic field effects (MFEs) — that alter the chemical yields and rate kinetics explained by the radical pair mechanism (RPM) [15, 16].

Chapter 1 starts by introducing the physical foundations of the Earth's magnetic field. The first observations of avian magnetosensitivity are then revealed through studies on migratory songbirds' behavioural responses to magnetic fields. Finally, a preface into the photochemistry and structure of Cry flavoproteins — the currently postulated photosensitive protein, responsible for the navigation abilities of migratory songbirds — completes the introductory chapter to avian magnetoreception.

Chapter 2 delves into the quantum mechanical approaches to magnetosensitivity of spin, along with a description of the RPM that explains how the interaction between two spins results in MFEs. The sensitivity to magnetic fields of singlet-triplet spin state interconversion is explored through hyperfine and Zeeman interactions of electron spins of RPs with spins of magnetic nuclei and applied magnetic fields, respectively. Throughout the chapter, a particular attention is drawn to how MFEs can be studied through fluorescence spectroscopy.

Chapter 3 presents droplet-based microfluidics as a novel technique for analysing Cry flavoproteins. As standard approaches to optical spectroscopy of Crys require substantial amounts of protein sample, microfluidics emerges as an attractive experimental method that tackles this issue by encapsulating picolitre volumes of photoactive samples through automated, high-throughput generation of monodisperse microdroplets. The chapter begins by outlining the necessary foundations of fluid mechanics of relevance to microflows, followed by a description of the experimental technique and data analysis procedure.

Chapter 4 reveals the results from spectroscopic characterisation of three flavin model systems:

1. flavin adenine dinucleotide (FAD) in citric buffer of pH 2.3 to elucidate intramolecular RPM mechanisms using microfluidics and investigate the effects of continuous laser illumination on sample degradation within microdroplets;

2. flavin mononucleotide (FMN) with ascorbic acid ($AscH_2$) in pH 3 and pH 7 to examine MFEs in high field and low field regions, resulting from intermolecular electron transfer;

3. riboflavin (RF) with tryptophan (Trp) in pH 7 to assess how reducing the sample volume further from 80 μm to 50 μm in microdroplet diameter influences the development of MFEs.

Chapter 5 serves to validate the successful development of the microdroplet fluorescence technique by presenting the first-ever recordings of avian Cry fluorescence in microdroplets. The chapter demonstrates the necessary developments put in place to accommodate the screening of Cry4a flavoproteins, along with experimental results on domestic chicken (*Gallus gallus*) mutant *Gg*Cry4a W369F acquired in continuous flow of microdroplets.

Contents

FRONT MATTER

Abstract **v**

Table of Contents **vii**

Acknowledgements **xi**

Abbreviations **xiii**

Physical Constants **xv**

MAIN MATTER

1 Introduction **1**
1.1 Background and Motivation 1
1.2 Physical Foundations of the Earth's Magnetic Field 2
1.2.1 Geocentric Magnetic Dipole Model of the Earth 2
1.2.2 Direction of the Geomagnetic Field 3
1.3 Biological Magnetoreception 4
1.4 Flavoprotein Cryptochrome 7
1.4.1 Molecular Foundation of Flavins 8
1.4.2 Chemistry of Isoalloxazine Electron Transfers 8
1.4.3 Photochemistry of Flavins 10
1.4.4 Structure of Cryptochromes 12
1.5 Focus of Thesis 14

2 Quantum Mechanics of Spin **16**
2.1 Electron Spin 17
2.1.1 Single Spin Systems 17
2.1.2 Two Spin Systems 19
2.1.3 Interaction Between Spins 21
2.1.4 Mechanisms of Singlet-Triplet Interconversion 28
2.2 Magnetic Field Effects in Cryptochromes 32
2.2.1 Radical Pair Mechanism 32
2.2.2 Magnetic Sensitivity of Radical Pairs 34
2.3 Summary and Outlook 36

3 Methodologies of Droplet-Based Microfluidics **37**
3.1 Introduction to Microfluidic Technology 39

3.2 Laws of Fluid Motions . . . 40
3.2.1 The Continuity Hypothesis . . . 41
3.2.2 The Navier-Stokes Equation . . . 44
3.3 Physics of Microdroplet Formation . . . 47
3.3.1 Interface Formation of Two-Phase Microflows . . . 48
3.3.2 Dimensionless Numbers . . . 50
3.3.3 Droplet Breakup Modes in Microfluidic Chips . . . 52
3.4 Droplet Transport Phenomena . . . 54
3.4.1 Film Lubrication and Microdroplet Velocity . . . 54
3.4.2 Microflow fields and mixing currents . . . 55
3.5 Working Principles of Microdroplet Fluorescence Experiment . . . 56
3.5.1 Experimental Apparatus and Data Acquisition Process . . . 57
3.5.2 Data Analysis . . . 60
3.6 Summary and Outlook . . . 63

4 Magnetic Field Effects in Flavin Model Systems 65
4.1 Flavin Adenine Dinucleotide in Citric Acid . . . 66
4.1.1 Photochemistry of $F-AH_2^+$ Radical Pairs . . . 66
4.1.2 Description of the Experimental Conditions . . . 67
4.1.3 $F-AH_2^+$ Fluorescence Emission . . . 67
4.1.4 Power Dependence Measurements . . . 68
4.1.5 MARY Results and Discussion . . . 68
4.2 Flavin Mononucleotide and Ascorbic Acid . . . 70
4.2.1 Photochemistry of $FMN-AscH_2$ . . . 71
4.2.2 pH Dependence of $FMN-AscH_2$ . . . 71
4.2.3 Description of the Experimental Conditions . . . 72
4.2.4 $FMN-AscH_2$ Fluorescence Emission . . . 72
4.2.5 MARY Results and Discussion . . . 73
4.2.6 Test of Microdroplet Generation Reproducibility . . . 75
4.3 Riboflavin and Tryptophan . . . 76
4.3.1 Photochemistry of RF−TrpH . . . 77
4.3.2 Description of the Experimental Conditions . . . 77
4.3.3 RF−TrpH Fluorescence Emission . . . 78
4.3.4 MARY Results and Discussion . . . 78
4.4 Summary and Outlook . . . 80

5 Avian Cryptochrome Magnetosensitivity on Droplet-Based Microfluidics 82
5.1 Point Mutations in Cryptochrome 4a . . . 82
5.2 Development of the Microdroplet Fluorescence Experimental Setup . . . 84
5.2.1 Minimisation of the Tubing Length . . . 84
5.2.2 Improving the Stability of Sample Stage Holder . . . 85
5.3 Mutant Chicken Cryptochromes in Microdroplets . . . 86
5.3.1 Photochemistry of *Gg*Cry4a W369F . . . 86
5.3.2 Sample Preparation Protocol . . . 86
5.3.3 Description of the Experimental Conditions . . . 87
5.3.4 *Gg*Cry4a W369F Microdroplet Fluorescence . . . 88

5.3.5 Attempts at Measuring Magnetic Field Effects on *Gg*Cry4a W369F 89
5.4 Conclusions and Future Work 89

Bibliography **91**

BACK MATTER

List of Figures **99**

List of Tables **102**

APPENDIX

A Quantum Mechanical Spin Dynamics Simulation on Radical Pairs **105**
A.1 Introduction to Density Matrix Formalism 105
A.2 Details of the Quantum Spin Dynamics Simulation 108
A.3 *MATLAB* Code 109

B Spherical Shape of Droplets and Minimisation of Surface Area **113**
B.1 Second Law of Thermodynamics 113
B.2 Principle of Minimum Energy 113
B.3 Surface Tension and Geometrical Surface Energy Minimisation 115

C Supplementary Material for Chapter 4 **117**
C.1 Applied Flow Pressures for the FMN−$AscH_2$ Model System 117
C.2 Fluorescence Spectra of RF−TrpH Model System 118

D *Poster for the Conference "Lab-on-a-Chip and Microfluidics Asia 2023"* **119**

E *Poster for the Conference "18^{th} Symposium on Magnetic Field and Spin Effects in Chemistry and Related Phenomena"* **120**

Acknowledgements

I owe my gratitude to many people who helped me along the way these past few years. First and foremost, I want to express my warmest thanks to my supervisors for accepting me into your fantastic groups and changing my life forever. The child I once was could never have dreamed to be a part of the University of Oxford.

Prof. Stuart Mackenzie, thank you for your immense support and for bringing me into the community of microfluidics. Your intellectual depth has always been a source of admiration for me. I can only hope that the print I have left in your group will play a part in pioneering this method further and beyond the expected.

Prof. Peter Hore, it has been an absolute pleasure representing your group abroad and thank you for providing me the opportunity to fulfill my lifelong dream to see Japan. Your wisdom never ceased to nourish my curiosity and ignite new ideas which, without a doubt, contributed to the scientist I am today.

Prof. Christiane Timmel, I am truly fascinated by your charisma — you always light up the room with your contagious laugh and positivity. Thank you for making me feel welcome and for encouraging me to always strive forward. This has been a truly immersive experience and I will never see birds the same way ever again!

To the joint Mackenzie-Timmel-Hore group, thank you all for fostering such a friendly environment. Dr. Patrick Murton, thank you for taking me under your wing and teaching me everything I know about microfluidics. You are a true inspiration and I wish you success wherever the world of Physics takes you next. Dr. Lewis Antill, your support has been like a comforting shoulder to me. May South Korea bless your family with the happiest of days. Carl Olavesen, I could not have asked for a better partner to join Oxford together! Thank you for all the coding lessons and, most importantly, being a true friend. I have learned so much from you and I am excited to see you and Ramesh build a future together. Dan Cubbin, you are a true leader with the greatest sense of humour. It seems like you can crack any problem thrown at you, even that of a microfluidic nature! Thank you for all the help, I cannot wait to see what you accomplish next. Pip Benjamin, thank you for being my lunch buddy and for holding my back as a fellow physicist. You are such an interesting person and I hope you achieve everything your heart desires. Laila Shah, thank you for all the fun nights we have spent together and for introducing me to Mia Whitefield. It is always a blast being around you and I only wish we had more time to create more memories. Tommy

Pitcher, Ana Štuhec, Jamie Gravell and Dr. Angela Gehrckens, I have always looked up to you in the group and admired your cleverness. Listening to you convey your thoughts on various topics of science during our Tuesday meetings always inspired me, and I hope to be as intelligent as you are one day. Will Parry and Jiahan Zhao, thank you being my Part II combo. May athletics and New York bring new colours to your lives like never before!

To my family at St Hilda's College, I have had an absolute blast in Oxford. Amy Bennett, my partner in crime, meeting you has been an incredible experience from day 1. Know that you have made yourself a lifelong friend who will always wait for you (そしてスズさん!) in Paris. To my fellow matriculation buddies — Sam Hodgson, Constantin Treuleben, Jade Léopoldine, Amelia Wyckoff, Floor Stoelinga, Steve Chung and Hannah Evans — you have made Oxford my home. Meeting every single one of you has made me better in some way and I cannot wait to see you all again. Qiandai Wang, Benjamin Sanetra, Luna Wu and Sara Naqvi — thank you for all the lovely times spent together. Don't forget to keep up the Hilda's spirit beating in your hearts!

To my 75 and Bully lot, you guys have dropped into my life like a bomb. Thank you for the unforgettable nights we have spent together and the craziest parties of my life. To Gabija Drazdauskaitė and Mo Al-Shubbar, you have changed London forever for me. Thank you for bringing me into your unstoppable dream team — I will see you both in San Francisco! To Vainius Kriščiūnas, none of this would be possible without you. I am absolutely thrilled to call you my best friend and I am excited to walk through life with you. Finalement, à mon 인연, merci de m'avoir révélé le beauté de l'amour, je n'aurais jamais cru le vivre un jour. J'espère que nos chemins se croiserons de nouveau.

Brangi Paškevičių šeimyna, be Jūsų pagalbos ir pasitikėjimo visa ši kelionė niekada nebūtų įvykusi. Mama, Tu esi didžiausias mano įkvėpimo šaltinis, kuriuo niekada nenustoju didžiuotis. Lukai, Tu — mano didžiausias ramstis ir geriausias draugas. Dėkui, kad visada esi šalia ir nenustoji manimi pasitikėti. Kotryna, be Tavo lietuvių kalbos įgūdžių aš niekad nebūčiau laimėjęs *Kitas 100* stipendijos ir atvykęs į Oksfordą — lieku Tau amžinai skolingas. Močiute, Tavo nenutrūkstamas rūpestis ir nesibaigiantis atsidavimas mane saugo ir lydi kiekvieną dieną. Myliu ir apkabinu Jus visus.

I hereby dedicate this thesis to each and every single person mentioned above.

Abbreviations

AH	Adenine
$AscH_2$	Ascorbic acid
BET	Back electron transfer
CCD	Charge-coupled device
COC	Cyclic olefin copolymer
Cry	Cryptochrome
cw	Continuous wave
DNA	Deoxyribonucleic acid
Er	*Erithacus rubecula* (European robin)
ET	Electron transfer
FAD	Flavin adenine dinucleotide
FMN	Flavin mononucleotide
FQY	Fluorescence quantum yield
Gg	*Gallus gallus* (domestic chicken)
GPS	Global positioning system
HF	Hyperfine
HFE	High field effect
HOMO	Highest occupied molecular orbital
IR	Infrared
ISC	Intersystem crossing
LED	Light emitting diode
LFE	Low field effect
LUMO	Lowest occupied molecular orbital
MFE	Magnetic field effect
MARY	Magnetically altered reaction yield
PMT	Photomultiplier tube
RF	Riboflavin
RP	Radical pair
RPM	Radical pair mechanism
SCRP	Spin-correlated radical pair
Uv/Vis	Ultraviolet-Visible light
Trp	Tryptophan

Physical Constants

Avogadro constant, N_A	$6.022 \times 10^{-23}\ \mathrm{mol}^{-1}$
Bohr magneton, μ_B	$9.274 \times 10^{-24}\ \mathrm{J\,T}^{-1}$
Boltzmann constant, k_B	$1.381 \times 10^{-23}\ \mathrm{T}^{-1}\,\mathrm{s}^{-1}$
Electron gyromagnetic ratio, γ_e	$1.761 \times 10^{11}\ \mathrm{m\,s}^{-2}$
Electron mass, m_e	$9.109 \times 10^{-31}\ \mathrm{kg}$
Elementary charge, e	$1.602 \times 10^{-19}\ \mathrm{C}$
Free electron g-value, g_e	-2.0023
Gravitational acceleration, g	$9.806\ \mathrm{m\,s}^{-2}$
Planck's constant, h	$6.626 \times 10^{-34}\ \mathrm{m}^2\,\mathrm{kg\,s}^{-1}$
Reduced Planck's constant, $\hbar$	$1.055 \times 10^{-34}\ \mathrm{m}^2\,\mathrm{kg\,s}^{-1}$
Vacuum permeability, μ_0	$1.256 \times 10^{-6}\ \mathrm{N\,A}^{-2}$

MAIN MATTER

Chapter 1

Introduction

1.1 Background and Motivation

Each year, millions of migratory songbirds set off on an extraordinary journey of seasonal migration in search of conditions vital for their survival and breeding [2, 17–20]. Birds — such as the European robin — perform long-distance travel ranging over thousands of kilometers, in tune with the annual cycle of seasonal change, to take advantage of different resources available during particular seasons of the year, including food and a thermally adapted environment. Over the years, studies have shown that numerous migratory species can do this with an extreme degree of precision [1–4], proving that animals return to their places of origin, *e.g.* mating and resting areas, from thousands of kilometers away [21, 22]. This suggests that migratory animals can pinpoint a relatively small target from great distances, well outside the scope of direct sensory perception. It is possible to track the precise migration routes of migratory species on Earth by making use of the latest cutting-edge technology available to humans, such as remote sensing, satellite and GPS tracking [23, 24]. However, the unresolved riddle still present to this day is *how* they accomplish these navigational journeys.

There currently exist two hypotheses explaining the backbone mechanism of such long haul navigation: the chemical hypothesis, which suggests that migratory terrestrial animals follow the distribution of volatile substances in the atmosphere [25] and/or the distribution of soluble components in seawater for aquatic animals [26, 27]; and the geomagnetic hypothesis, which assumes that animals use the geomagnetic field parameters for precise migration [28, 29]. While ongoing research continues to explore the chemical hypothesis, its physical foundations remain unclear [30]. On the

other hand, we have a comprehensive understanding of the physical properties of the geomagnetic field, taking into account both their geographical variability and temporal fluctuations. This research project examines the fascinating quantum properties behind the biophysical avian compass by focusing on the geomagnetic hypothesis. For this reason, it is important to start by laying out the fundamentals of the Earth's magnetic field, which is one of the core factors that animals rely on during migration.

1.2 Physical Foundations of the Earth's Magnetic Field

The planet Earth is surrounded by an enormous magnetic field called the *magnetosphere*. Nearly all of Earth's geomagnetic field originates in the fluid outer core, where, like boiling water on a stove, convective forces induced by heat flow from the inner core constantly stir molten electrically-conducting iron-nickel alloy [31–34]. Driven by the Earth's rotation, this enormous dense mass of metal experiences the *Coriolis effect*[1], generating a complex spiral movement of the fluids. This produces electrical currents hundreds of kilometers wide and flowing at thousands of kilometers per hour as the Earth rotates [34–36], which, based on the principles of electromagnetism, produces the geomagnetic field. This mechanism is known as the *geodynamo process* [34, 37, 38], and it provides a potentially significant geographic framework for animals to navigate across the world.

1.2.1 Geocentric Magnetic Dipole Model of the Earth

The most basic way to describe the geomagnetic field is by referring to it as a geocentric magnetic dipole model placed at the center of the Earth and tilted by 11° with respect to Earth's rotation axis [39] (see **Figure 1.1a**). However, the actual field of the Earth is far more complex than a simple dipole model: the geomagnetic poles that fit best the geocentric dipole do not align with the measured magnetic poles at which the magnetic field lines are vertical, nor do they align with the actual geographic poles that form the rotational axis of the Earth [40, 41].

[1] Based on classical mechanics, the *Coriolis effect* explains that objects in motion experience an inertial force acting on them if they are in a non-inertial reference frame. In the case of the Earth, the inertial force tends to align fluid motions around the Earth's rotational axis.

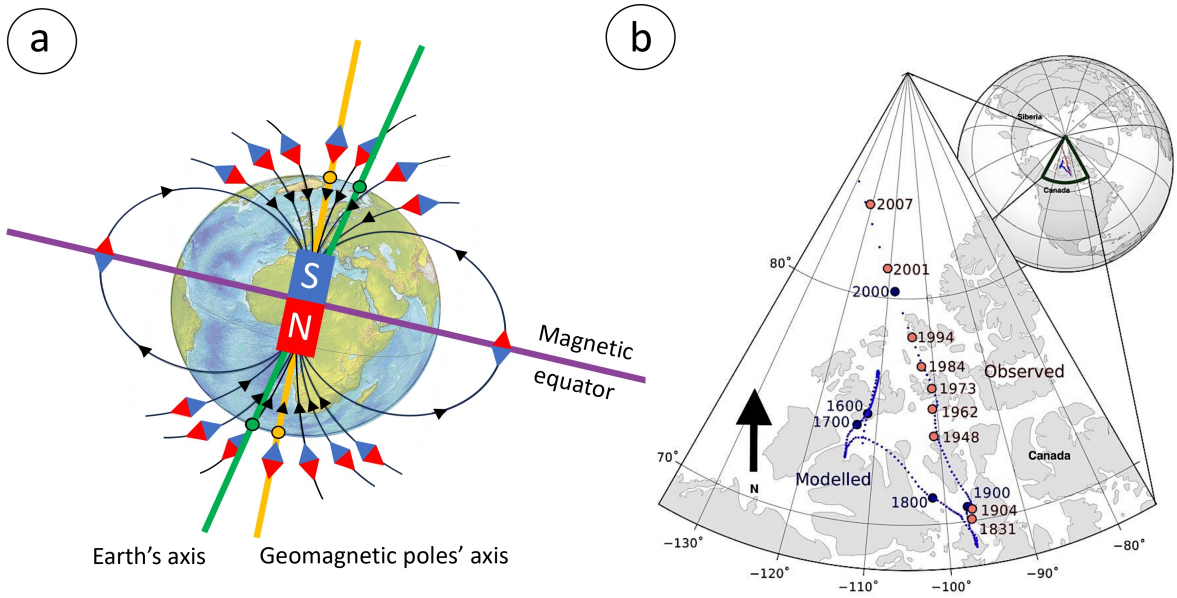


Figure 1.1 (a) Relationship between the geographic Earth's poles (green line), the geomagnetic poles (yellow line) and the magnetic equator (purple line) with magnetic field lines. (b) The movement of Earth's north magnetic pole across the Canadian Arctic. Red circles are observed magnetic pole positions, blue circles are modelled positions (reproduced with permission from article [39]).

Therefore, comparing the Earth's magnetic field to a dipole model is only a *first-order approximation* of the system [42, 43]. Interestingly, these poles are not stationary and they wander independently of one another around the Earth's rotational axis due to the moving of the molten core that generates the Earth's magnetic field [31, 44–47] (see **Figure 1.1b**). This means that the Earth's magnetic field evolves in time, and deriving tractable models to describe it as accurately as possible is of practical importance for animal navigation.

1.2.2 Direction of the Geomagnetic Field

At any location on the surface of the Earth, the direction of the geomagnetic field can be described by a three-dimensional vector, typically measured in the *North-East-Down* coordinate system (see **Figure 1.2**). It constitutes a set of basis vectors that are scaled such that if the Earth's field were a perfect dipole, they would add up to an orthonormal set of vectors on the sphere. Such a system gives rise to two angles, which are traditionally used to describe the precise direction of the geomagnetic field: *magnetic inclination* (also known as the *dip angle*) and *declination* (or the *magnetic variation*). The *inclination* is the angle that the geomagnetic field is tilted with respect

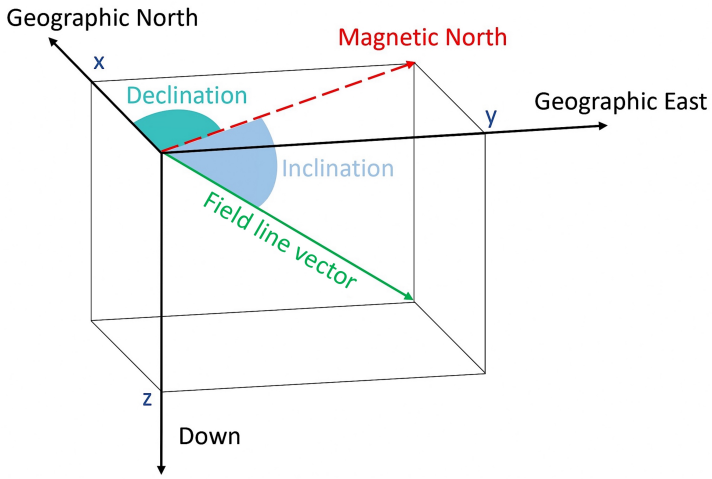


Figure 1.2 Illustration of the North-East-Down coordinate system used to describe the direction of the magnetic field. The magnetic inclination is the angle between the Earth's surface and the magnetic field lines. Magnetic declination is the angle between the magnetic north of the compass and the true north. Note that the labels *north* and *east* refer to the hemisphere in which the pole is found.

to the surface of the Earth and is measured downwards from the horizontal tangent surface to the field vector. It is used to reference geographical latitude and it varies from $-90°$ at the south magnetic pole to $+90°$ at the north magnetic pole, which balances out to $0°$ at the magnetic equator. The *declination* reflects the tilt of the Earth's magnetic field with respect to its axis of rotation and measures the angle between geographic north and the field vector projected onto the horizontal plane. It is used to determine the direction along the Earth's surface toward geographical north (also known as *true north*) and can be used to determine longitude. This is possible by comparing magnetic north with true north using the sun and stars and leads to longitudinal positioning through comparison with the characteristic geographic variation of the declination.

1.3 Biological Magnetoreception

The Earth's magnetic field has been used for navigation throughout human history, dating back to before the Han dynasty (206 BCE — 220 AD) to at least the ancient civilizations around 4^{th} century BCE, when the Chinese built early compasses using lodestones, which are naturally occurring magnetized minerals of magnetite [48]. The earliest mention of a magnetic compass and its use appears in *The Book of the Devil*

Valley Master [48], where the author notes the compass — or *south pointer* as the Chinese called it — could be carried with jade hunters to prevent them from getting lost during their journeys.

However, the use of magnetic compasses is not exclusively restricted to humans; in fact, many different animals use magnetic sensing — from molluscs [49–51], insects [52–56], fish [57, 58] and amphibians [59–63] to migratory species, such as turtles [64–67], birds [68–75], and mammals [76–81]. This fascinating sense and ability of organisms to perceive and respond to Earth's magnetic field is known as *magnetoreception*. Animals' physiological responses to natural environmental factors of the geomagnetic field have captivated scientists since as early as the mid-to-late 1800s, when a Russian zoologist Alexander von Middendorff put forward the idea that insects and birds could rely on the geomagnetic field for navigational purposes [82]. However, it was not until the 1960s that the first established findings of European robins to sense both the strength and direction of Earth-strength magnetic fields emerged [83]. Since that time, different mechanisms of magnetoreception have been explored extensively across various field strengths, spanning both gaseous and condensed phases [1] and including intramolecular systems exposed to microtesla fields [84].

Behavioural Experiments on Migratory Birds

Migratory birds, specifically European robins (*Erithacus rubecula*), have become model systems for studying the mechanisms of animal magnetoreception. In order to understand the exact mechanism by which birds migrate, scientists first started by deciphering the different navigational pointers available to migratory birds across different stages of their journeys. Researchers first revealed that migratory songbirds are able to read celestial cues and can demonstrate the ability to use the position of the sun, stars, and various geographical landmarks, like the night sky, throughout their course of navigation [85–87]. In the late 1940s, Kramer placed red-backed Shrikes (*Lanius collurio*) and blackcaps (*Sylvia atricapilla*) into circular cages with paper funnels around their internal walls and an ink pad base, such that when a bird hops forward, distinct black prints from the bird's claws are left imprinted on the paper [83]

(see **Figure 1.3a**). He then documented the traces left to determine the direction of birds' hopping under the night sky, which seemed to correspond with their seasonal migratory direction (see **Figure 1.3b**). Later studies by Wiltschko & Wiltschko confirmed that some migratory birds adapt their orientation direction when the magnetic field surrounding the cage is redirected by a coil system without changing its intensity or inclination [87–89].

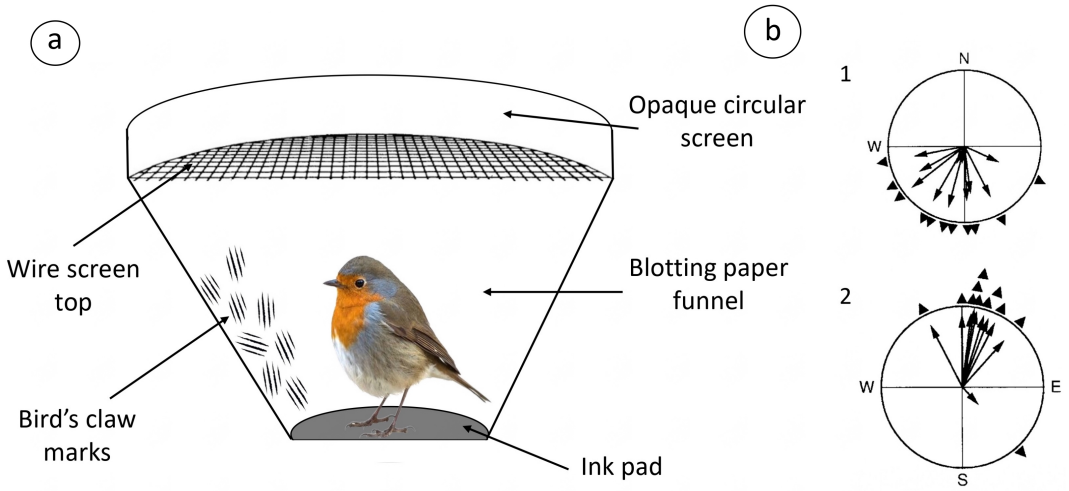


Figure 1.3 (a) Side view of the circular cage model for tracking birds' directional preference of flight under the night sky. The paper funnel acts as the main source of data as traces of birds' claws soaked with ink are left upon hopping. (b) Experimental findings of European robins' headings under 565 nm green light. The arrows represent the mean vectors of individual birds and the triangles at the periphery of the circle give mean headings of individual birds averages over two different measurements, recorded for geomagnetic fields of 1. Autumn 2000; 2. Spring 2001 (reproduced with permission from article [89]).

Even when weather conditions were poor and these geophysical pointers were not available to them, many birds were still seen to complete their journeys effortlessly [90]. This hinted at the presence of an additional mechanism integrated into the bird's physiology, functioning independently of the typical use of vision. In 1978, Schulten *et al.* proposed a light-driven magnetic compass sense in living organisms, relying on radical pairs (RPs) [8], further reinforcing European robins' previously recorded ability to perceive the intensity and direction of Earth-level magnetic fields [5]. Subsequent behavioral studies of exposure to different wavelengths of light (see **Figure 1.4b**) have demonstrated that birds became disorientated when placed under a red li-

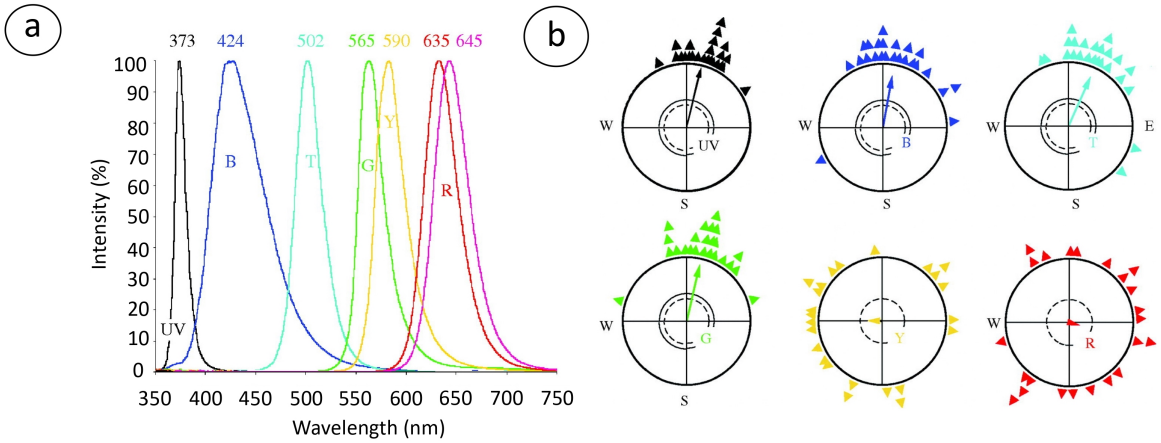


Figure 1.4 (a) Spectra of light-emitting diodes used to determine wavelength dependencies and map bird orientation patterns. (both (a) and (b) reproduced with permission from article [91]). (b) European robins' orientation during spring migration under finite bandwidth light of different wavelengths [91]. The results indicate that birds orientate well under exposure to green and blue light, but not under other wavelengths of light.

ght environment but would swiftly regain their sense of direction following exposure to blue or green light[2], further proving that this magnetic sensing capability indeed relies on blue light [92]. Moreover, this dependence on wavelength strongly implied that the source of magnetoreception resided within the bird's eyes. Thus, in 2000, Ritz, Adem, and Schulten proposed the photoreceptor flavoprotein *cryptochrome* (*Cry*) as the possible magnetoreceptor molecule that is considered to be responsible for orientation *via* magnetic fields, found in the retinal tissue of migratory birds [9–11].

1.4 Flavoprotein Cryptochrome

The name flavin refers to the yellow, water-soluble chromophoric[3] group of protein cofactors that occur naturally in animals and plants. Flavin-dependent blue-light-responsive proteins (Crys) play a fundamental role in biology as they are found to take part in regulatory mechanisms, such as photoregulation of circadian rhythms in animals [93] and light-dependent flowering induction in relation to day length [94]. They are also believed to mediate bioluminescence [95], photosynthesis [96] and the magnetic compass sense in certain animals [2–4, 64–81].

[2]Orientation under green light is debatable — recent studies done by collaborators in Germany suggest that blackcaps cannot orientate under green light.

[3]Chromophores are defined as molecules which can absorb light in the visible, near-IR or near-UV region, thereby emitting color as a result of such absorption.

1.4.1 Molecular Foundation of Flavins

Most flavoproteins consist of a vitamin B_2 cofactor named *riboflavin* (*RF*) either in the form of *flavin mononucleotide* (*FMN*) or *flavin adenine dinucleotide* (*FAD*) [97], as shown in **Figure 1.5**. Their distinctive feature is a tricyclic heterocycle chromophore called *7,8-dimethylisoalloxazine* which can undergo oxidation-reduction reactions as photo-induced electron acceptors [98]. Their rich chemical properties come from their ability to absorb UV and blue light [94, 99] and form three redox states by either catalysing the two-electron dehydrogenation of various substrates or by accepting a single electron in a two-step process *via* their different radical states [100].

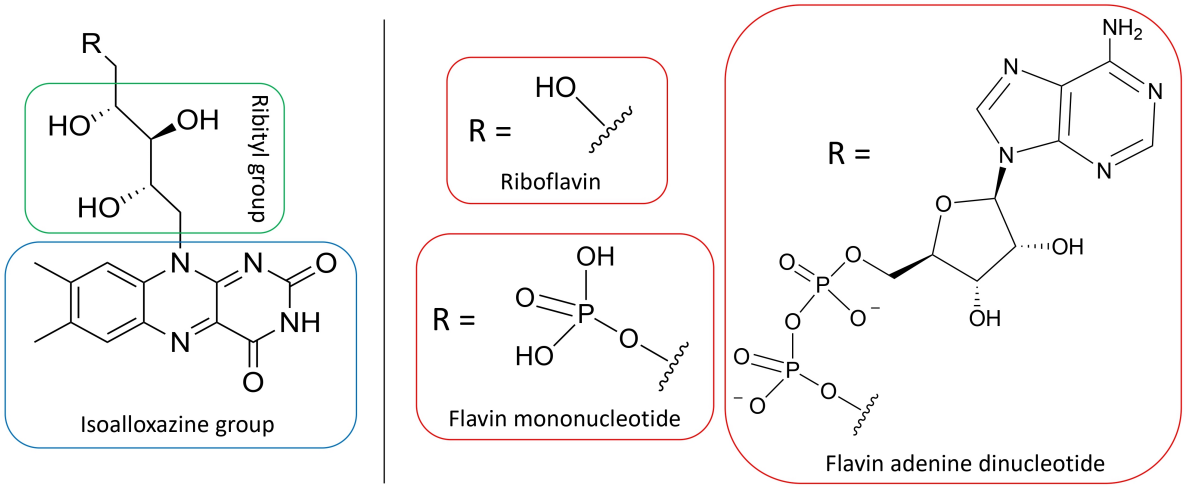


Figure 1.5 The structure of flavins. All flavins contain the tricyclic heterocycle isoalloxazine. The flavin moiety is attached with an adenosine diphosphate to form FAD. It is also found as FMN, which is a phosphorylated form of RF.

1.4.2 Chemistry of Isoalloxazine Electron Transfers

The reactive areas of flavins are associated with the chemistry of the isoalloxazine ring. Both of these molecules can undergo reversible reduction, accepting electrons from an electron donor, producing molecules that are inherently different in their spectroscopic and photophysical properties. For isoalloxazines, this can lead to the formation of three possible redox states, namely the oxidised *quinone*, the one-electron reduced *semiquinone*, and the two-electron fully-reduced *hydroquinone*, as shown in **Figure 1.7**.

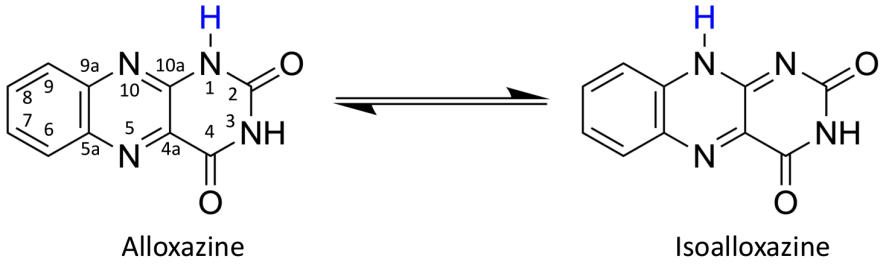


Figure 1.6 Proton transfer tautomerism of alloxazine and isoalloxazine. The exchanged hydrogen atom is depicted in blue.

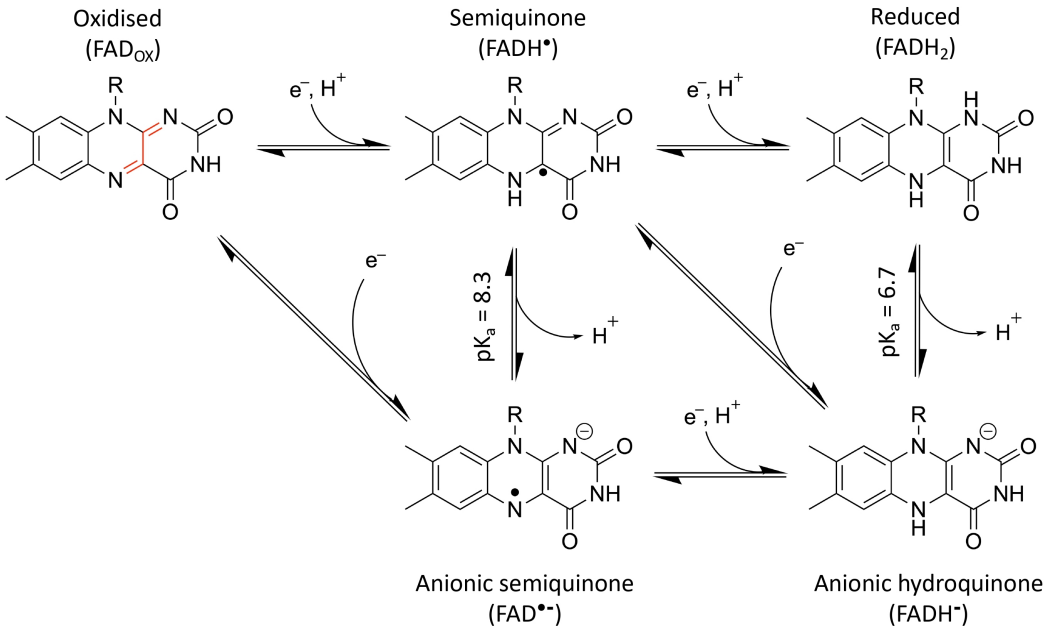


Figure 1.7 Redox and protonation states of the 7,8-dimethylisoalloxazine ring [101]. The initial moiety of interaction with an electron is indicated in red in the oxidised form of isoalloxazine. For the detailed structure of *R*, refer to FAD structure shown in **Figure 1.5**.

Understanding flavin cofactor molecular interactions in terms of molecular redox centres is essential in flavoprotein chemistry, with particular applications to Crys for magnetoreception purposes. The interconversion between these redox states is driven by the acceptance of electrons from suitable electron donors. Oxidised forms of flavins can thus form the stable semiquinone radical FADH$^{\bullet}$ which is particularly important in electron transfer (ET) processes in Cry proteins.

Each redox state of the isoalloxazine moiety attains acid-base equilibrium based on the specific pH of the solution. Within the pH range of $3 - 9$, in which most proteins are stable and functional [102], flavins predominantly exist in their neutral and anionic

states. In contrast, at pH < 1, a significant amount of cationic state is produced, thus unable to further participate in the oxidation-reduction mechanisms.

1.4.3 Photochemistry of Flavins

The spectral characteristics of the non-covalently bound flavins are greatly influenced by their redox state. Each state of the isoalloxazine moiety is spectroscopically distinct, allowing the progression of ET between the different states to be followed over time by absorption spectroscopy. In the fully oxidised form, flavins display two absorption bands (see **Figure 1.8**); the first one is seen peaking at $\sim$ 450 nm, corresponding to the electronic $\pi \rightarrow \pi^*$ transition between the highest occupied molecular orbital (HOMO) and the lowest unoccupied molecular orbital (LUMO) [103]. This band is attributed to the $S_0 \rightarrow S_1$ transition, where S_0 and S_1 refer to the ground and excited singlet states, respectively [104, 105]. The second band is in the UV region peaking at $\sim$ 375 nm which corresponds to the electronic $n \rightarrow \pi^*$ transition, and is referred to as $S_0 \rightarrow S_2$ transition [105, 106]. Both of these bands are characteristic absorption peaks of flavins found in flavoproteins [107].

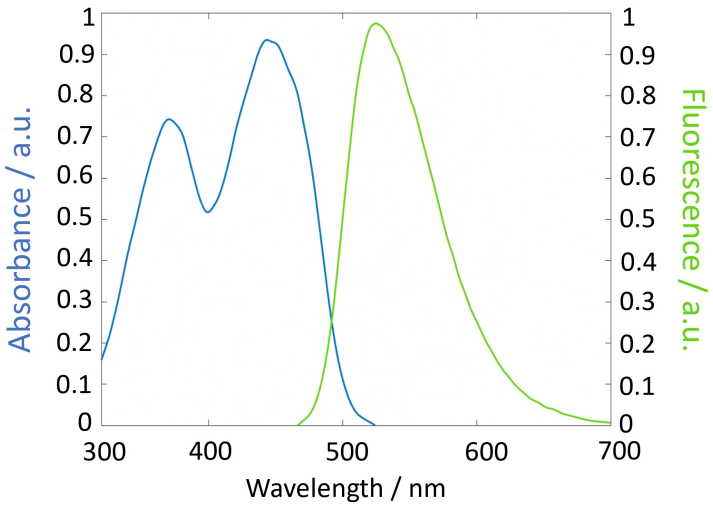


Figure 1.8 Experimental absorption and fluorescence spectra of an aqueous solution of oxidised FMN. Both spectra have been normalised for better visual comparison.

Upon absorption of photons, the formation of the excited flavin state can lead to complex photophysics observed in free solution or bound inside a protein, such as fluorescence, photoreduction, intersystem crossing (ISC)[108–110]. In solution, the oxidised FMN redox state is highly fluorescent with lifetimes of the singlet excited

state in the range of a dozen nanoseconds [111]. Experimental results show that FMN in water exhibits a fluorescence band peaking at ∼530 nm (see **Figure 1.8**) with a fluorescence-quantum yield (FQY) of $\phi_{\mathrm{F}} = 0.26$ [112, 113].

However, in proteins, nearby electron donors have the capacity to serve as *quenchers*[4], which results in diminished fluorescence intensity commonly noted in some of the redox states of flavins. In many cases, this occurs because of flavin photoreduction processes involving nearby aromatic amino acids: the radical pair state between an excited flavin (Fl) and tryptophan (Trp) $^{1,3}\mathrm{Fl}^{\bullet-}\mathrm{TrpH}^{\bullet+}$ lies energetically between the neutral ground state and the singlet excited state (see **Figure 1.9**). In other words, a competition between the three possible pathways for the excited singlet flavin state $^{1}\mathrm{Fl}^{*}$ to decay back to the ground state $^{1}\mathrm{Fl}$ takes place:

1. the formation of an intermediate flavin-tryptophan radical pair state $^{1,3}\mathrm{Fl}^{\bullet-}\mathrm{TrpH}^{\bullet+}$ followed by back-transfer of an electron (left-hand pathway of **Figure 1.9**);
2. emission of fluorescence and deexcitation to the ground state flavin $^{1}\mathrm{Fl}$ (middle pathway of **Figure 1.9**);
3. ISC to the triplet state $^{3}\mathrm{Fl}^{*}$ (right-hand pathway of **Figure 1.9**).

Although ISC is frequently observed in aqueous solutions of flavins, ETs from nearby aromatic amino acids towards the flavin in protein occur rapidly, typically within a picosecond, thus surpassing ISC in efficiency [108, 109, 114–116].

The existence of these intrinsic amino acid reactants inside the Cry protein thus prevents the formation of long-lived singlet flavin excited states $^{1}\mathrm{Fl}^{*}$. As ET out-competes the ISC — which can be as fast as ∼10 ns [109, 117] with considerable quantum yields [118] — the accumulation of this state is thus impeded. Therefore, it has been proposed that the presence of ET-quenchers for the singlet flavin excited state $^{1}\mathrm{Fl}^{*}$ imposes a significant selection pressure on flavoenzymes [119].

[4] In photochemistry, *fluorescence quenching* is known as a decrease in fluorescence intensity from an excited state of a molecule, which can happen through energy transfers, further excited-state reactions, or the formation of other intermediates.

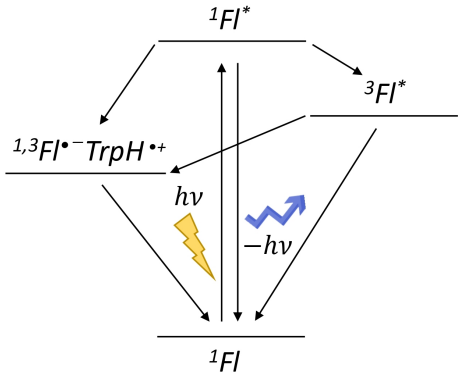


Figure 1.9 A simplified diagram illustrating photochemical excitation and decay processes in oxidised flavins. Excitation of the ground state ^{1}Fl leads to the population of $^1Fl^*$ excited state, which can return to the ground state through fluorescence, to the triplet state ^{3}Fl *via* ISC, or to a charge-separated flavin radical state $^1Fl^{\bullet-}TrpH^{\bullet+}$. The triplet state $^3Fl^*$ can decay non-radiatively to $^3Fl^{\bullet-}TrpH^{\bullet+}$ excited state or decay back to the singlet ground state ^{1}Fl *via* phosphorescence.

In the majority of flavoproteins, photoinduced radical states quickly undergo charge recombination, usually within picoseconds [120], leading to the eventual thermal dissipation of photon energy. Consequently, these closed reaction cycles do not result in long-lived photochemical products but instead prevent their formation.

1.4.4 Structure of Cryptochromes

Crys belong to the family of flavoproteins which consist of light-oxygen-voltage (LOV) proteins and blue-light absorbing FAD (BLUF) proteins. Cry's structural sequence bears great resemblance to DNA photolyases[5] (PL): they are single domain proteins with a conserved photolyase homology region (PHR) predominantly composed of α-helices, along with a single region of β-sheets situated close to the N-terminus of the photoreceptor. In the case of Cry4a flavoprotein, the ET originates from a chain of four conserved Trp residues (namely, Trp_A W395, Trp_B W372, Trp_C W318 and Trp_D W369), starting at the nearest residue to the FAD cofactor Trp_A [6]. Trps connect to the isoalloxazine moiety with an average spacing[6] of ∼5 Å, which leads to ultrafast

[5]Photolyases are monomeric proteins comprised of 450-550 amino acids and two noncovalently bound chromophore cofactors. They are responsible for repairing damage to DNA caused by exposure to UV light.

[6]Distances between each Trp residue and the isoalloxazine moiety were measured in *PyMOL* software for *Gg*Cry4a.

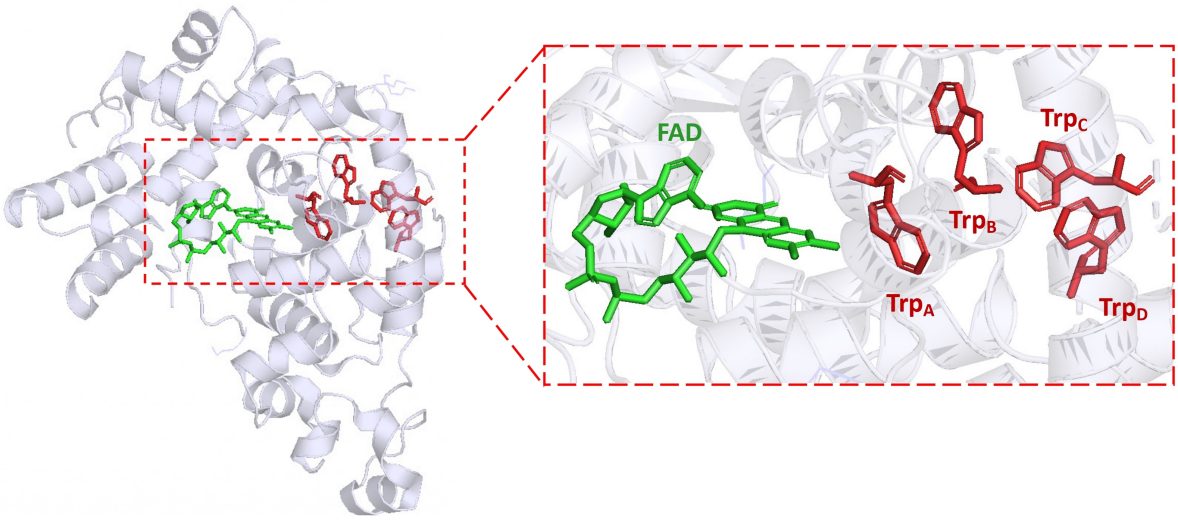


Figure 1.10 Homology model of the chicken cryptochrome 4a protein (*Gg*Cry4a) (drawn from PDP ID entry 6PTZ using *PyMOL* software [121]). The zoomed inset depicts the *Gg*Cry4a protein FAD cofactor (green) and the neighboring Trp residues Trp_A W395, Trp_B W372, Trp_C W318 and Trp_D W369 (red).

ETs [122]. The Trp tetrad is one of the central components in forming magnetically sensitive RPs, making them essential to the geomagnetic magnetoreception hypothesis. [15].

As mentioned in **Section 1.3**, Cry proteins are found in the retinal tissue of migratory birds. They are found in double cone segments residing in the retina of European robins and domestic chickens [123]. Such arrangement of Cry4a proteins makes it a strong candidate for the receptor molecule for the avian magnetic compass for multiple reasons:

1. Crys are known to absorb electromagnetic radiation in the visible, so light needs to reach the receptor molecule and induce the formation of magnetically sensitive intermediates. Therefore, the eye is an ideal location for the optimal collection of photons [9, 124];

2. The stacked disk membrane conformation in the avian retina ensures an alignment of Crys in the same direction within each receptor cell, thus permitting Crys to function as a cohesive unit [123];

3. The spherical arrangement of the eye provides a widespread distribution of the double cones across the entire retinal hemisphere, ensuring that the formed magnetically sensitive intermediates are in different alignments with the geomagnetic field [123].

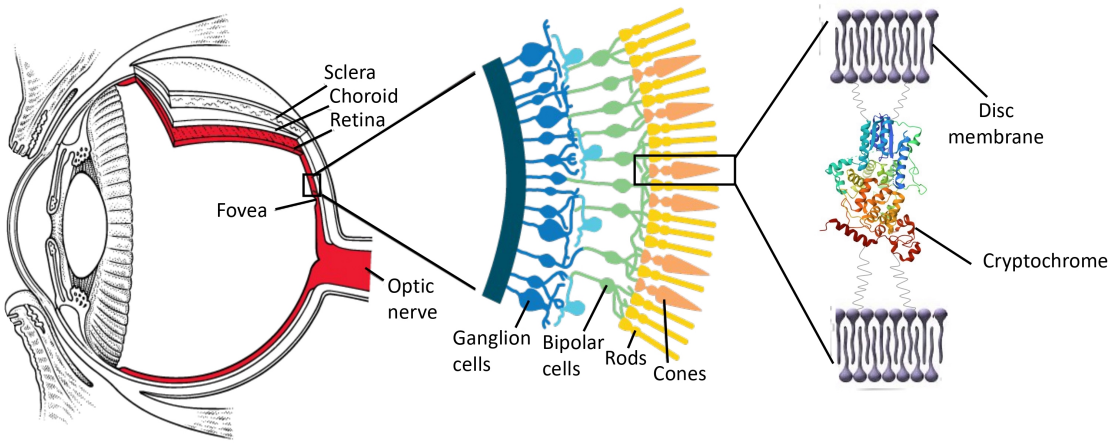


Figure 1.11 Schematic cross-section illustration of the localisation of the Cry protein inside a bird's retinal tissue, where light impulses inside the eye's optical system are converted into electrical signals (reproduced with permission from the article [125]). The retina consists of multiple cell layers and the primary signals arising in the rod and cone outer segments are passed to the bipolar and ganglion cells. Inside the cone segments, the primary magnetosignal is generated in the receptor protein Cry.

1.5 Focus of Thesis

This thesis aims to present the development of a novel technique designed to advance our understanding of the principles that explain avian navigation and improve experimental methodologies in this field.

Chapter 1 presented the photochemistry of Cry proteins and their interaction with the geomagnetic field which are thought to be the primary driving forces of avian magnetoreception. The underlying principles behind the navigational abilities of migratory animals are governed by quantum mechanics. This is further explored in **Chapter 2** which covers the necessary foundations of quantum mechanics that explain the mechanism of long-haul avian migration.

Chapter 3 describes the laws of fluid motions that govern microflows in droplet-based microfluidic devices that were used during this research project to acquire experimental data. In addition, it explains how pL samples of Cry4a are enclosed within microdroplets to record magnetically-sensitive measurements and how the subsequent data analysis process of each individual microdroplet is carried out.

Chapter 4 covers the results of confocal fluorescence microscopy measurements on thousands of microdroplets as a demonstration of the capabilities of the microdroplet fluorescence experimental technique. For this, three model systems are presented, each showing the successful development of the microfluidic instrument for magnetically-sensitive measurements in high-throughoput microdroplet flows.

Chapter 5 reports the developmental process required for the experimental technique to perform measurements on Cry flavoproteins. This chapter presents the first ever-recorded studies on microflows of mutant domestic chicken Crys (*Gg*Cry4a W369F) using droplet-based microfluidic technology. In addition, **Chapter 5** summarises the projects main highlights and breakthroughs in the development of the new microdroplet fluorescence technique, and proposes topics for further research avenues.

Chapter 2

Quantum Mechanics of Spin

Behavioural experiments on European robins (as described in **Section 1.3**) revealed that the internal avian compass depends on the interaction with light within a narrow spectrum of specific wavelengths [89, 91]. The plausible magnetoreceptive protein Cry4a seems to fulfill the needed requirements that could explain the backbone mechanism of avian navigation (as specified in **Section 1.5**). It was thus suggested that birds could detect directional information from the influence of the geomagnetic field on the coherent spin dynamics of short-lived, photo-induced RP reaction intermediates [8, 126].

A *spin-correlated radical pair* (SCRP) is a transient reaction intermediate made up of two radicals, both of which contain unpaired electrons. The electrons of RPs have a spin angular momentum, giving each separate radical a magnetic moment. Both radicals are typically produced as part of the same reaction, meaning their spin angular momentum is conserved and the spins assume either a singlet or triplet quantum state. Both of these states in which the RP is found can be altered by magnetic fields, thereby influencing the interconversion between the two states [16].

It is important to mention that RPs are integral to the leading geomagnetic hypothesis of avian magnetoreception. Therefore, the following chapter describes the principles of quantum mechanics related to RP formation and interaction in Cry flavoproteins, which thus govern the magnetic sensitivity that is thought to explain the mechanism of bird migration.

2.1 Electron Spin

The property of spin is the intrinsic form of angular momentum found in elementary particles, such as electrons. However, it does not represent the classical spinning motion and it is purely a quantum mechanical concept.

In classical physics, the angular momentum measures how much *motion* an object has around a given axis. This is usually split between two contributions: angular momentum from *spinning*, where the spinning axis goes through the object's center of mass, and *orbital* angular momentum, where the axis is located outside the centre of mass. An appropriate demonstration of this is using the planet Earth as an example, as it has some angular momentum associated with spinning around its own axis, as well as the angular momentum it has from orbiting the sun.

In quantum physics, any particle possessing a non-zero quantum spin will always have angular momentum, regardless of whether or not it is classically spinning or orbiting. Initially, this appears somewhat perplexing; one might question how a stationary particle can retain angular momentum. While the concept of intrinsic angular momentum may seem counter-intuitive, it can be compared to the intrinsic energy of stationary masses under special relativity given by:

$$E = mc^2. \tag{2.1}$$

This implies that a particle experiencing no forces and remaining motionless still possesses energy. Similarly, according to the principles of quantum mechanics, even stationary particles can exhibit intrinsic angular momentum, which is often referred to as their quantum spin.

2.1.1 Single Spin Systems

In quantum mechanics, angular momentum is quantised. This means that spin cannot take on arbitrary values but instead is restricted to discrete and well-defined quantities described by two quantum numbers: the spin quantum number, s, and the spin projection quantum number, m_s. The definition of these numbers arises from the eigenstates

of the quantum mechanical operator for the square magnitude of the total spin angular momentum, $\hat{S}^2 = \hat{S}_x^2 + \hat{S}_y^2 + \hat{S}_z^2$, and the projection operator of the spin along an arbitrary z-axis, S_z [127], such that:

$$\hat{S}^2 \left|s, m_s\right\rangle = s(s+1)\hbar^2 \left|s, m_s\right\rangle , \tag{2.2}$$

$$\hat{S}_z \left|s, m_s\right\rangle = m_s \hbar \left|s, m_s\right\rangle , \tag{2.3}$$

where $\hbar$ is the reduced Planck constant. s can take on any positive integer or half-integer values and m_s is defined in the range $m_s = s, s-1, ..., -s$. For electrons and Fermion particles, s is defined as $s = \frac{1}{2}$, thus yielding the values of $m_s = \pm\frac{1}{2}$. This means that there exist two possible projections onto the z-axis in the $|s, m_s\rangle$ basis, commonly denoted as:

$$\left|\frac{1}{2}, \frac{1}{2}\right\rangle = |\alpha\rangle , \qquad \left|\frac{1}{2}, -\frac{1}{2}\right\rangle = |\beta\rangle . \tag{2.4}$$

These two electronic spin states are orthogonal and frequently referred to as *spin up* for $|\alpha\rangle$ and *spin down* for $|\beta\rangle$ based on their orientation that reveals itself when a particle encounters a magnetic field, as shown in **Figure 2.1**.

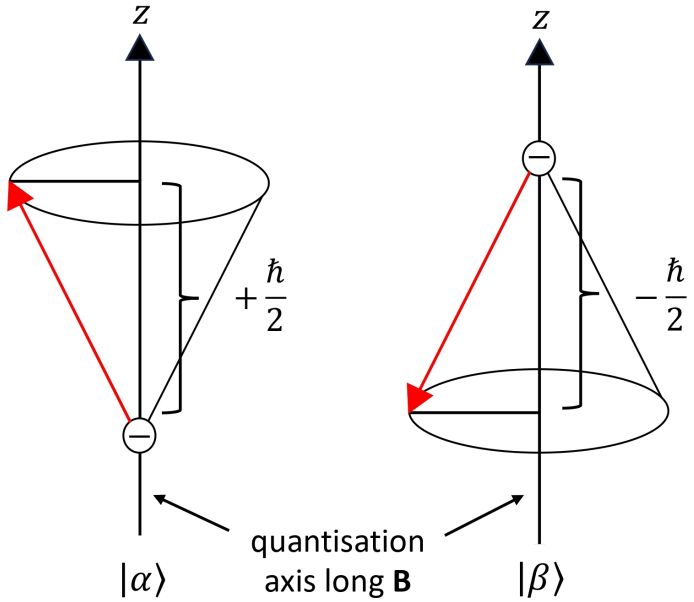


Figure 2.1 Vector representation of the two possible orientations of the vector model of an electron with spin-$\frac{1}{2}$ in a magnetic field. The spin magnetic moment, having an absolute magnitude of $\frac{\hbar}{2}$, can align *up* for $|\alpha\rangle$ and *down* for $|\beta\rangle$ (see **Equation 2.4**) in the direction of the magnetic field. Their precession around the magnetic field is further described in **Section 2.1.4**.

2.1.2 Two Spin Systems

If we consider now a system with two sources of spin, namely $\mathbf{s}_1$ and $\mathbf{s}_2$, the total spin angular momentum operator, $\hat{\mathbf{S}}$, can be expressed as a sum of each individual spin operators:

$$\hat{\mathbf{S}} = \hat{\mathbf{s}}_1 + \hat{\mathbf{s}}_2. \tag{2.5}$$

Analogously to a single spin system, a two-spin system can be projected onto an arbitrary z-axis using the associated spin projection operator, $\hat{S}_z$:

$$\hat{S}_z = \hat{s}_{1z} + \hat{s}_{2z}. \tag{2.6}$$

A system with multiple sources of intrinsic angular momentum will experience interaction among these different forms of angular momentum. According to the Heisenberg uncertainty principle[1], it is impossible to determine the precise values of certain pairs of operators, such as two-spin projections, at the same time. This means that $\hat{\mathbf{S}}$ and $\hat{s}_{1z,2z}$ do not commute[2]; to describe the interactions of a two-spin system, there is a necessity to use either a *coupled* or *uncoupled* representation of the system.

Uncoupled Representation

The uncoupled basis treats both spins of the system as separate vectors of the form $|s_1, m_{s1}; s_2, m_{s2}\rangle$, without considering their interaction. This makes it convenient for analysing the properties of each spin separately as the total angular momentum is undefined, whereas the z-components of each of the spins are precisely described in this basis.

The total spin quantum number, S, for a combined system of two spins is dictated by the Clebsch-Gordan series [128]:

[1] The probabilistic nature of quantum mechanics states that there is a limit to how precisely a pair of two unique physical properties can be known. The product of the uncertainties of two observables, A and B, each of which has its associated operator, $\hat{A}$ and $\hat{B}$, is given by $\sigma_A \sigma_B \geq \frac{\hbar}{2}$, where $\sigma_A = \sqrt{\left\langle \hat{A}^2 \right\rangle - \left\langle \hat{A} \right\rangle^2}$ [128].

[2] The commutator of two operators, $\hat{A}$ and $\hat{B}$, is defined as $[A, B] = AB - BA$. If the commutator is zero, the operators commute, implying that the observables they represent can be measured simultaneously with arbitrary precision [128].

$$S = s_1 + s_2, s_1 + s_2 - 1, ..., |s_1 - s_2|. \tag{2.7}$$

Therefore, for two electrons with $s_1 = s_2 = \frac{1}{2}$ spin quantum numbers, their two spin species can couple in four ways when their individual spins $|\alpha\rangle$ and $|\beta\rangle$ combine [128], summarised in **Table 2.1**.

Spin orientation	m_{s1}	m_{s2}	M_S	$\|s_1, m_{s1}; s_2, m_{s2}\rangle$
$\uparrow\uparrow$	$\frac{1}{2}$	$\frac{1}{2}$	1	$\|\alpha_1\alpha_2\rangle$
$\uparrow\downarrow$	$\frac{1}{2}$	$-\frac{1}{2}$	0	$\|\alpha_1\beta_2\rangle$
$\downarrow\uparrow$	$-\frac{1}{2}$	$\frac{1}{2}$	0	$\|\beta_1\alpha_2\rangle$
$\downarrow\downarrow$	$-\frac{1}{2}$	$-\frac{1}{2}$	-1	$\|\beta_1\beta_2\rangle$

Table 2.1 The uncoupled basis for a two spin-$\frac{1}{2}$ system.

Coupled Representation

The coupled basis reveals the collective behaviour of both spin particles if they have strong correlation. This means that the new states formed *via* interaction of both spin particles are eigenstates of the total spin angular momentum, $\hat{S}^2$, and its projection, M_S. Thus, the individual spin angular moments, s_{1z} and s_{2z}, are left undefined and the basis set is now $|s_1, s_2, S, M_S\rangle$.

Using this notation for two electrons, the total spin quantum number can yield values of $S = 1$ or $S = 0$, depending on the relative orientations of their spins [128]:

- S=0 gives a single possible outcome as $M_S = 0$, thus corresponding to an anti-symmetric combination of the two spins:

$$|0,0\rangle = \frac{1}{\sqrt{2}}\left(|\alpha_1\rangle \otimes |\beta_2\rangle - |\beta_1\rangle \otimes |\alpha_2\rangle\right) = \frac{1}{\sqrt{2}}\left(|\alpha_1\beta_2\rangle - |\beta_1\alpha_2\rangle\right); \tag{2.8}$$

- S=1 yields three possible values of M_S, namely $\{1, 0, -1\}$, thus corresponding to the following symmetric combinations:

$$\begin{aligned} |1,1\rangle &= |\alpha_1\rangle \otimes |\alpha_2\rangle = |\alpha_1\alpha_2\rangle\,; \\ |1,0\rangle &= \frac{1}{\sqrt{2}}\left(|\alpha_1\rangle \otimes |\beta_2\rangle + |\beta_1\rangle \otimes |\alpha_2\rangle\right) = \frac{1}{\sqrt{2}}\left(|\alpha_1\beta_2\rangle + |\beta_1\alpha_2\rangle\right); \\ |1,-1\rangle &= |\beta_1\rangle \otimes |\beta_2\rangle = |\beta_1\beta_2\rangle\,. \end{aligned} \tag{2.9}$$

Thus, the *singlet state* $|S\rangle$ is defined as $|0,0\rangle$, and the three *triplet states* $|T_+\rangle$, $|T_0\rangle$, $|T_-\rangle$ correspond to $|1,1\rangle$, $|1,0\rangle$, $|1,-1\rangle$, respectively, named based on their spin multiplicities, which are summarised in **Table 2.2**. Such systems characterise the behaviour of coupled electron spins, which describe the mechanism of action behind avian magnetoreception that is further discussed in **Section 2.2.1**. The coupled scheme can be visually represented using the vector model shown in **Figure 2.2**.

Spin multiplicity	Coupled basis	S	M_S	$\lvert s_1, s_2, S, M_S\rangle$
$\lvert S\rangle$	$\lvert 0,0\rangle$	0	0	$\frac{1}{\sqrt{2}}(\lvert\alpha_1\beta_2\rangle - \lvert\beta_1\alpha_2\rangle)$
$\lvert T_+\rangle$	$\lvert 1,1\rangle$	1	1	$\lvert\alpha_1\alpha_2\rangle$
$\lvert T_0\rangle$	$\lvert 1,0\rangle$	1	0	$\frac{1}{\sqrt{2}}(\lvert\alpha_1\beta_2\rangle + \lvert\beta_1\alpha_2\rangle)$
$\lvert T_-\rangle$	$\lvert 1,-1\rangle$	1	-1	$\lvert\beta_1\beta_2\rangle$

Table 2.2 The coupled basis for a two spin-$\frac{1}{2}$ system.

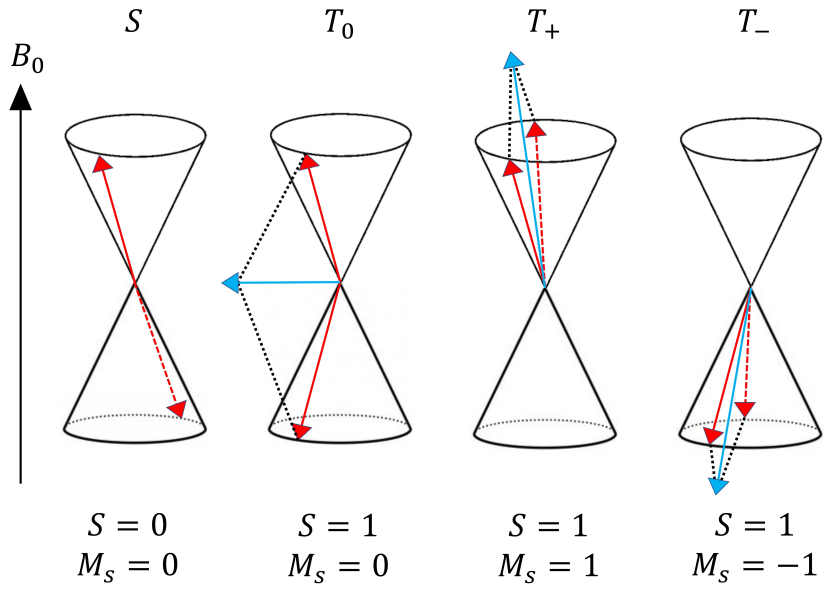


Figure 2.2 Vector model representation of the singlet and triplet spin states. Red arrows represent individual spin states, while blue arrows illustrate their combined result. The resultant vector has a magnitude of $\sqrt{2}\hbar$ and 0 for the triplet and singlet states, respectively. The vectors rotate at a constant angle around the cones represented above.

2.1.3 Interaction Between Spins

The application of a magnetic field influences the spin dynamics of a RP, typically altering its product yields and lifetime. The initial spin state will determine the specific outcome of applying an external magnetic field on RPs, as well as the observable of focus within the RP. This subchapter describes the various dominant interactions involved in RP formation and how they alter the overall spin dynamics.

Zeeman Interaction

Spin and orbital rotations of an electron are the two contributions to the electron's angular momentum. If the electron is viewed as a classical rigid body, rotating an electrically charged particle about an axis with an angular momentum, $\mathbf{L}$, gives its magnetic dipole moment, $\boldsymbol{\mu}$:

$$\boldsymbol{\mu} = -\frac{e}{2m_e}\mathbf{L}, \tag{2.10}$$

where e is the unit of elementary charge and m_e is the electron mass.

In **Equation 2.10** the angular momentum, $\mathbf{L}$, may represent the *spin* angular momentum, the *orbital* angular momentum, or the *total* angular momentum. The ratio between the true spin magnetic moment and its prediction *via* this model is depicted by the dimensionless free electron g-factor[3], g_e, equal to ≈ 2:

$$\boldsymbol{\mu} = -g_e\frac{e}{2m_e}\mathbf{L}. \tag{2.11}$$

As spin does not have a classical analogue, the angular momentum, $\mathbf{L}$, can be referred to as the spin angular momentum, $\mathbf{s}$. Therefore, by analogy, the electron spin magnetic moment can be expressed as:

$$\hat{\boldsymbol{\mu}}_{\boldsymbol{s}} = g_e\gamma_e\hat{\boldsymbol{s}}, \tag{2.12}$$

where the constant $-\frac{e}{2m_e}$ is expressed as the gyromagnetic ratio, γ_e, for simplicity.

A magnetic moment in a magnetic field possesses potential energy in the following form:

$$E_p = -\boldsymbol{\mu}\cdot\mathbf{B}, \tag{2.13}$$

where $\mathbf{B}$ is the magnetic field vector and E_p is the energy of interaction, the value of which depends on the orientation of the magnetic moment. If we consider the magnetic field direction to be in the z-axis, **Equation 2.13** can be simplified to:

$$E_p = -\mu_z B_0, \tag{2.14}$$

[3]The g-factor of a free electron is derived to be precisely 2 according to Dirac's relativistic quantum mechanics [129]. However, a more precise value of ≈ 2.0023 can be found through the use of quantum electrodynamics principles [130, 131]

where B_0 is the magnitude of $\mathbf{B}$.

This classical expression of potential energy can be rewritten in the quantum realm by constructing the eigenstates of the energy of the interaction Hamiltonian, $\hat{H}_{Zeeman}$, by using the uncoupled electron basis [132]:

$$\begin{aligned}\hat{H}_{Zeeman}\left|s, m_s\right\rangle &= -\mu_z B_0 \left|s, m_s\right\rangle \\ &= -g_e \gamma_e \hat{s}_z B_0 \left|s, m_s\right\rangle .\end{aligned} \tag{2.15}$$

By comparison with **Equation 2.3**, we can thus describe the Hamiltonian in the following way:

$$\begin{aligned}\hat{H}_{Zeeman}\left|s, m_s\right\rangle &= -g_e \gamma_e B_0 m_s \hbar \left|s, m_s\right\rangle \\ &= g_e \mu_B B_0 m_s \left|s, m_s\right\rangle ,\end{aligned} \tag{2.16}$$

where the gyromagnetic ratio can be expressed in terms of the Bohr magneton, $\mu_B = -\gamma_e \hbar$. Therefore, the eigenvalues of the Zeeman interaction energy for an isolated electron spin are

$$E_{Zeeman} = g_e \mu_B B_0 m_s. \tag{2.17}$$

Because an electron possesses the values of $m_s = \pm\frac{1}{2}$, the external magnetic field causes a splitting in the energy levels of the two $|\alpha\rangle$ and $|\beta\rangle$ spin states based on their orientation along the z-axis, known as the *Zeeman effect*. However, this is not the case at zero field, where both states are degenerate.

In terms of a coupled basis consisting of two spin-$\frac{1}{2}$ particles, $\hat{\boldsymbol{s}}$, $\hat{s}_z$, s and m_s can be substituted with the corresponding operators and quantum numbers associated with the *total* spin angular momentum, $\hat{\boldsymbol{S}}$, $\hat{S}_z$, S and M_s, respectively. In this representation, the Hamiltonian of a two electron system in a magnetic field can be expressed in the following way:

$$\begin{aligned}\hat{H}_{Zeeman}\left|S, M_S\right\rangle &= -g_e \gamma_e \hat{S}_z B_0 \left|S, M_S\right\rangle \\ &= g_e \mu_B B_0 M_S \left|S, M_S\right\rangle\end{aligned} \tag{2.18}$$

Based on the Clebsch-Gordan series outlined in **Section 2.1.2**, $S = \{0, 1\}$ and $M_S = \{\{0\}, \{-1, 0, 1\}\}$, yielding a total of four possible electronic spin states. The energy of eigenstates with $M_S = 0$ corresponds to electronic states $|S\rangle$ and $|T_0\rangle$ and does

not change with an applied magnetic field. However, the energy of eigenstates with $M_S = \pm 1$ corresponds to $|T_\pm\rangle$ electronic states which become energetically separated from $|S\rangle$ and $|T_0\rangle$ as the strength of the applied magnetic field increases. Nevertheless, the triplet states are degenerate at zero field before diverging with the increase in the applied magnetic field, just as they are for the one-electron system.

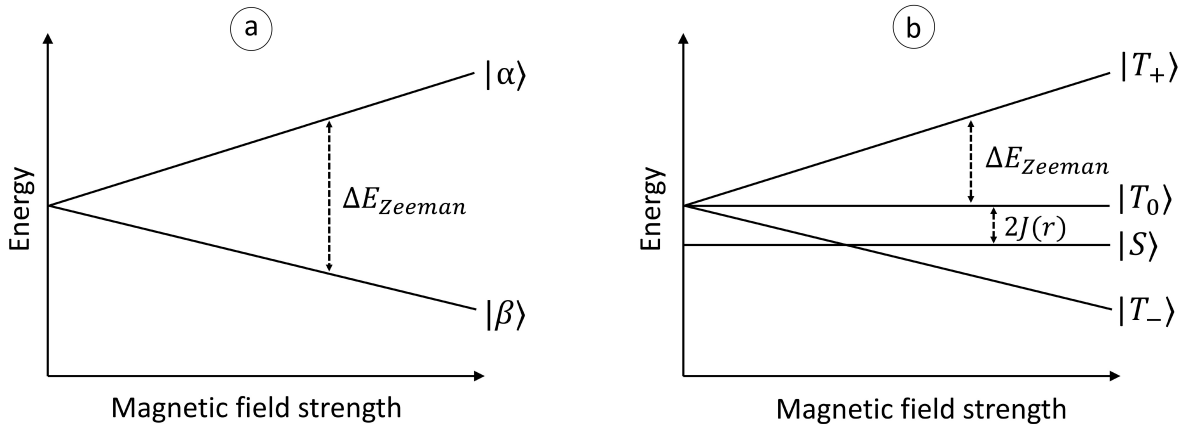


Figure 2.3 The change in energy of the different electronic states resulting from the Zeeman effect differs for (a) a system with one electron, leading to an increase in energy of $|\alpha\rangle$ and a decrease in energy of $|\beta\rangle$ as the magnetic field strength increases, and (b) a system with two electrons, where the energy of the $|S\rangle$ and $|T_0\rangle$ states is constant, but $|T_+\rangle$ and $|T_-\rangle$ states vary equivalently to the $|\alpha\rangle$ and $|\beta\rangle$ states. The exchange interaction lifts the degeneracy between the $|S\rangle$ and $|T\rangle$ states and separates them by $2J$.

Exchange Interaction

The Pauli exclusion principle states that no two identical fermions[4] can occupy the same quantum state [133]. In other words, identical fermions, such as two electrons, cannot occupy the same location in space with the same quantum number. Therefore, the arrangements of two electrons in space varies based on their spin alignment (parallel for triplet states and antiparallel for singlet state). This causes the triplet and singlet states to exhibit different average energies which primarily rely on the exchange coupling, J, [134], and lifts their degeneracy even when the electrons do not experience any magnetic field [128]. This is known as the *exchange interaction* and the Hamiltonian describing this interaction is given by [128]:

$$\hat{H}_{Ex} = -2J(r)\hat{\boldsymbol{S}}_1 \cdot \hat{\boldsymbol{S}}_2, \tag{2.19}$$

[4]Fermion is a type of elementary particle possessing half-integer values of spin ($\frac{1}{2}$, $\frac{3}{2}$, and so on). Examples of fermions include electrons, protons, neutrons and quarks.

where r represents the distance between the two molecules. The inter-electron coupling results in an energy difference between the $|S\rangle$ and $|T\rangle$ states, which quantitatively describes how the interaction depends on the distances between the molecules. This can be understood by the exchange integral of the overlap of the two electron wavefunctions over all space [113, 132]:

$$J(r) \approx J_0\, exp\left(-\frac{r}{r_J}\right), \tag{2.20}$$

where r is the inter-radical separation, r_J is a characteristic range parameter over which the exchange interaction decays, and J_0 is the magnitude of the exchange interaction at $r = 0$. As the separation between the two electrons increases, $J(r)$ is assumed to decay exponentially. The energy difference between the $|S\rangle$ and $|T\rangle$ states is described as the following [128, 134]:

$$\Delta E = \langle S|\hat{H}_{Ex}|S\rangle - \langle T|\hat{H}_{Ex}|T\rangle = 2J(r). \tag{2.21}$$

This is known as the *Pauli repulsion* which removes the degeneracy of the $|S\rangle$ and $|T\rangle$ states, shown in **Figure 2.3b**.

Dipolar Coupling

The interaction between electron spins in a RP occurs through the magnetic dipole-dipole coupling of their magnetic moments through space. The Hamiltonian of this coupling is defined by the following [128, 132]:

$$\hat{H}_{Dip} = \hat{\boldsymbol{S}}_1^T \cdot \boldsymbol{D} \cdot \hat{\boldsymbol{S}}_2, \tag{2.22}$$

where $\boldsymbol{D}$ is the dipolar coupling tensor, describing the coupling strength between spins $\boldsymbol{S}_1$ and $\boldsymbol{S}_2$. When both spins are aligned parallel to each other, the dipolar interaction energy is maximised. In return, when spins are placed perpendicularly to one another, the dipolar coupling between them is at a minimum. Although these two cases portray limiting situations in terms of the relative spin positions, in reality, a system of two spins can be orientated in different directions in space, meaning that the strength of the dipolar interaction will vary. This directional dependence leads to an anisotropy in the energy levels of the triplet states, thereby lifting their degeneracy even in the absence of a magnetic field.

However, in solution, molecules are in constant stochastic movement due to their thermal energy and Brownian motion. As a result, dipolar interactions between electron spins in a RP suspended in liquids are averaged out over time to net zero, leaving the triplet states of the RP nearly degenerate in the absence of other interactions.

Hyperfine Coupling

In a similar manner to how the electron's spin magnetic moment can interact with an external field, it can also couple with the spin magnetic moments of other particles, for instance, the nuclei. These inherent interactions between unpaired electrons and nuclear spins are defined as *hyperfine couplings*, which in their most general form, are expressed as the following [132]:

$$\hat{H}_{HF} = \hat{\boldsymbol{S}}^T \cdot \boldsymbol{A} \cdot \hat{\boldsymbol{I}}, \tag{2.23}$$

where $\hat{\boldsymbol{S}}^T$ represents the transposed electron spin operator, $\hat{\boldsymbol{I}}$ is the nuclear spin operator, and $\boldsymbol{A}$ is the 3x3 hyperfine coupling tensor that mathematically describes hyperfine couplings in the x, y, z directions. This tensor can be split into two components, based on their interactions with the particles that surround the system — namely, the *isotropic* and *anisotropic* components.

From a quantum mechanical perspective, there exists a small probability that the electron penetrates into the nuclear region. This is where the *isotropic* hyperfine coupling arises, primarily describing the interaction between the nuclear spin and the electronic density at the nucleus. It is defined as the *Fermi contact interaction* and its isotropic hyperfine constant is expressed as [128]:

$$a_{Iso} = -\frac{2}{3}\mu_0\gamma_e\gamma_n|\Psi(0)|^2, \tag{2.24}$$

where μ_0 is the vacuum permeability, γ_e and γ_n are gyromagnetic ratios of the electron and the nucleus, respectively, and $|\Psi(0)|^2$ is the probability density of finding an electron at the nucleus.

The second contribution to the hyperfine interaction results from a classical dipole-dipole interaction associated with the electron and nuclear spins in the region located

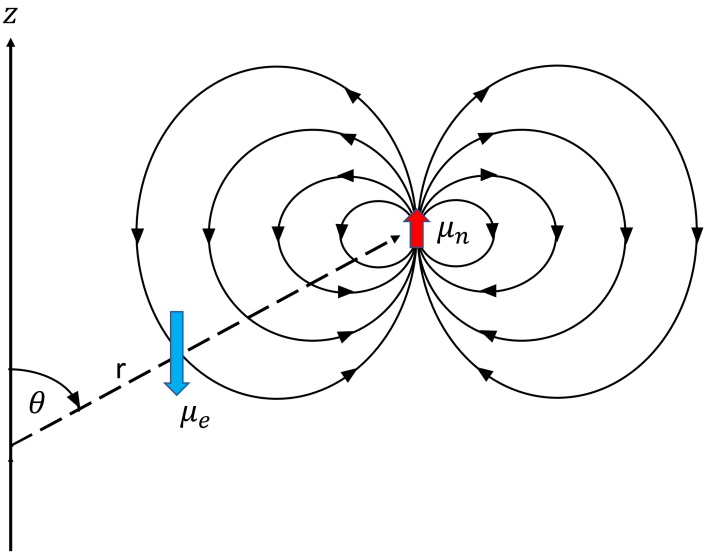


Figure 2.4 Interaction of the aligned magnetic dipoles moments μ_e (shown in blue) and μ_n (shown in red) originating from an electron and nuclear spins, respectively. The vector μ_e represents the state $M_S = -\frac{1}{2}$ and the vector μ_n indicates the state $M_I = \frac{1}{2}$. The angle θ is formed between the inter-dipole vector r and the applied magnetic field B.

outside of the nucleus, known as the *anisotropic* hyperfine coupling. According to classical electromagnetism [128], the associated anisotropic hyperfine coupling constant is dependent on the relative distance separating the magnetic moments of the electron and nucleus:

$$\boldsymbol{A}_{ani} = \frac{\mu_0 \gamma_e \gamma_n}{4\pi} \left(\frac{r^2 \boldsymbol{I} - 3\boldsymbol{r}\,\boldsymbol{r}}{r^5} \right), \tag{2.25}$$

where $\boldsymbol{r}$ describes the interspin vector with magnitude r, as depicted in **Figure 2.4**, and $\boldsymbol{I}$ is the identity matrix.

This gives us the *total* hyperfine coupling tensor which can be written as follows:

$$\boldsymbol{A} = a_{Iso} \cdot \boldsymbol{I} + \boldsymbol{A}_{Ani}. \tag{2.26}$$

It is important to note that the anisotropic component of the hyperfine coupling can be disregarded in solution as rapid tumbling averages the orientational dependence to zero [15]. However, it is essential in stationary systems, such as rigid retinal cells, where radicals have considerably less liberty to move around freely. This aspect is highly pertinent for the radical pair mechanism (RPM, further described in **Section 2.2.1**) as the highly abundant and magnetically active ^{1}H and ^{14}N isotopes are a typical source of hyperfine interactions in organic radicals.

2.1.4 Mechanisms of Singlet-Triplet Interconversion

The RP is formed in a singlet or triplet spin state of a coupled two-electron system because they inherit the spin states from the precursor, where there is significant interaction between the electron spins. Each radical's distinct electronic and nuclear environments cause their individual electrons to experience unique intraradical couplings, causing the singlet and triplet states to oscillate. As a result, this gives rise to the inherent magnetosensitivity of Crys, thus altering the reactions yields and rates of Cry photoreduction processes. This subchapter describes the different mechanisms that influence the interconversion between the singlet and triplet electronic states when electrons interact with external magnetic fields.

Hyperfine Mechanism

Once particles, such as electrons, are placed in a magnetic field, their nuclear magnetic moment will couple to the external magnetic field. This induces a *torque* on the magnetic moment, causing it to precesses around the applied magnetic field, given by the following:

$$\vec{\tau} = \vec{\mu} \times \vec{B}. \tag{2.27}$$

The magnetic moment, $\vec{\mu}$, is a vector quantity with a direction parallel to the angular momentum. For a fixed magnetic moment, this torque tends to align the spin magnetic moment with the direction of the magnetic field, as this configuration represents the lowest energy state.

However, in **Section 2.1.2**, it has been argued that $\hat{\mathbf{S}}$ and $\hat{s}_{1z,2z}$ do not commute. This means that sometimes we cannot simultaneously determine the vector magnitude of the overall spin and the z-projection of each of its components. The exerted torque prompts the spin magnetic moment to precess *around* the magnetic field direction in a cone-shaped loop (see **Figures 2.2** and **2.5**), rather than aligning directly with it [135]. Taking this into account, the exerted torque, which is perpendicular to the angular momentum, produces a change in the angular momentum, $d\boldsymbol{L}$, causing it to precess around an arbitrary z-axis. If we call φ the respective precession angle (*cf.*

Figure 2.5), the overall effect of the torque can be expressed as follows:

$$\begin{aligned} \tau &= \frac{d\boldsymbol{L}}{dt} \\ &= \boldsymbol{L} sin\theta \frac{d\varphi}{dt} \\ &= \frac{g_e e}{2m_e} \boldsymbol{L}\boldsymbol{B} sin\theta, \end{aligned} \tag{2.28}$$

where the second equation comes from **Figure 2.5** and the third equality from comparison with **Equation 2.27**.

The frequency at which the spin magnetic moment precesses around the magnetic field is known as the *Larmor frequency*, ω_L, which can be expressed in terms of the applied magnetic field strength, B_0, using **Equation 2.28**:

$$\begin{aligned} \omega_L &= \frac{d\varphi}{dt} \\ &= \frac{g_e e}{2m_e} B_0. \end{aligned} \tag{2.29}$$

With the help of **Equation 2.16**, we can express the Larmor frequency in terms of the Bohr magneton:

$$\omega_L = \frac{\mu_B g_e B_0}{\hbar}. \tag{2.30}$$

If we now consider two radicals that have different chemical compositions, their respective electron and nuclear spins will experience different magnetic fields upon coupling. As explained in **Section 2.1.3**, the presence of a nearby nucleus can modify the effective magnetic field, $\boldsymbol{B}_{Eff}$, that an electron experiences. This means that the electron's local magnetic field is also influenced by the contributions from nuclear magnetic moments. We can thus say that:

$$\boldsymbol{B}_{Eff} = \boldsymbol{B} + \boldsymbol{B}_{HF}, \tag{2.31}$$

where $\boldsymbol{B}_{HF}$ is the magnetic field generated through hyperfine interactions.

Depending on the chemical enviornment of each radical, we can, therefore, evaluate their overall difference in precession frequencies[5] of the electron spins:

$$\Delta\omega_0 = \omega_1 - \omega_2 = \frac{g\mu_B}{\hbar} \Delta B_{Eff}. \tag{2.32}$$

[5]This assessment is made assuming that both coupled electrons have an equal electron g-factor.

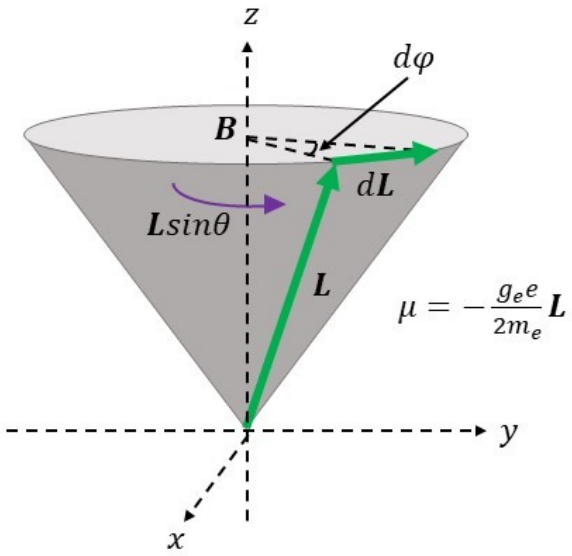


Figure 2.5 Dynamic conception of the spin-$\frac{1}{2}$ state. The angular momentum vector precesses retaining a constant component along an arbitrary z-axis.

This difference in precession frequencies (when $\Delta\omega_0 \neq 0$) can lead to the mixing of spin electronic states, if $\Delta\omega_0$ matches the energy difference between the $|S\rangle$ and $|T_{0,\pm}\rangle$ states. When $\boldsymbol{B} \sim \boldsymbol{B}_{Eff}$, which is typically referred to as the *low field region*, all $|S\rangle$ and $|T_{0,\pm}\rangle$ states can interconvert [136] because of their relatively close gaps in energy (see **Figure 2.3b**). This leads the electron and nuclear spin vectors to precess around the *resultant* angular momentum, which essentially may not be the z-axis. But when $|\boldsymbol{B}| \gg \boldsymbol{B}_{Eff}$, known as the *high field region*, the spins align with the external magnetic field, $\boldsymbol{B}$, and precess around the z-axis. This way only the mixing of $|S\rangle$ and $|T_0\rangle$ at frequency $\Delta\omega_0$ can happen [84], as the $|T_{\pm}\rangle$ states are too energetically isolated from one another due to the Zeeman interaction (see **Section 2.1.3**).

Δg Mechanism

Mixing between the singlet and triplet states can also occur if the electrons experience the same effective magnetic field, $\boldsymbol{B}_{Eff}$. This can happen if a divergence in the Larmor frequencies of the different spins exists, which is possible if the g-values of the two electrons vary [137]. In such a case, the Δg *mechanism* arises due to the coupling between the electrons' spin and orbital angular momentum.

When $g_1 \neq g_2$, the difference in Larmor frequencies can be expressed as follows [137]:

$$\Delta\omega = \frac{(g_1 - g_2)\,\mu_B B_0}{\hbar} = \frac{\Delta g \mu_B B_0}{\hbar}. \tag{2.33}$$

However, for carbon-centered RPs, typically involving organic molecules with light atoms (such as ^{1}H, ^{12}C, ^{14}N, ^{16}O, etc.), the contribution of spin-orbit coupling to spin dynamics is small, typically leading to $\Delta g < 0.001$ [137]. As a result, a significant source of spin mixing due to the Δg mechanism can be anticipated only at magnetic field strengths over 100 mT. Therefore, this mechanism can be disregarded for the work conducted in this thesis, as the highest magnetic field applied is 30 mT.

Spin Relaxation

While the hyperfine and Δg mechanisms enable coherent interconversion of the various spin electronic states, where the total spin is preserved, there exists a mechanism that disrupts the phase coherence through *spin relaxation*, thereby diminishing the magnetic sensitivity of RPs. As described in **Section 2.1.3**, molecules in solution are subjected to stochastic thermal motion, which induces random transitions between the electronic spin states [135]. In the high field region, where the Zeeman interaction dominates, two types of relaxation can happen, termed the *longitudinal* and *transverse* relaxations.

The relaxation of the populations of energy levels can be explained through rapid molecular motions that contribute to changes in hyperfine and anisotropic dipolar couplings within the coupled spin systems. This causes time-dependent fluctuations in the effective magnetic field and induces spin flip transitions [138]. Such relaxation is defined by a loss in exchange energy through dynamic interactions between the radicals in solution.

Stochastic motion can also cause relaxation of spin coherence which are described by spin flip-flop transitions without any exchange of energy of the spin system. This relaxation process involves one of the spins to flip from the $|\alpha\rangle$ to the $|\beta\rangle$ state, which provides the energy for a second spin to flip in the inverse way — from the $|\beta\rangle$ to the $|\alpha\rangle$ state [138].

2.2 Magnetic Field Effects in Cryptochromes

To think that magnetic fields as weak as the Earth's ($30-60\ \mu$T) are capable of significantly altering chemical reaction yields initially seems unconvincing, especially taking into account that the interaction between the Earth's magnetic field and a single radical pair species under physiological conditions is many orders of magnitude smaller than its thermal energy, k_BT [1, 2, 12, 15, 84, 113, 139].

The development of the radical pair mechanism (RPM) has allowed for a theoretical explanation of the fact that magnetic fields are observed to have an effect on the spin dynamics of chemical reactions (see **Appendix A**). The RPM describes how an external magnetic field can alter chemical yields by interacting with the spin state of a pair of radicals, for which the theoretical background has been presented in **Section 2.1**. The following subchapter explains the photochemical cycle involving Cry proteins and how they react to magnetic fields.

2.2.1 Radical Pair Mechanism

Because the systems of study presented in this thesis vary[6], it is useful to consider a simplified radical pair mechanism (RPM, shown in **Figure 2.6**), which comprises of an electron acceptor, A, and an electron donor, D. The radical pair mechanism is activated following blue light photoillumination at 450 nm of the ground singlet state, ^{1}A, which, based on the conservation of angular momentum, produces the excited singlet state, ^{1}A*. From here, three distinct reaction pathways are possible:

1. the excited singlet state, ^{1}A*, can fluoresce back to ground state, ^{1}A, and emit fluorescence (pathway denoted $h\nu'$ in **Figure 2.6**);

2. the excited singlet state, ^{1}A*, can undergo an *electron transfer* (ET) process, during which it can accept an electron from an electron donor, D, to form a spin-correlated radical pair, ^{1}[A$^{\bullet -}-$ D$^{\bullet +}$] (pathway denoted ET^S in **Figure 2.6**);

[6]The specific molecular formulation of the electron acceptor and donor will be precisely indicated for each model system in **Chapters 4** and **5**. However, to introduce the RPM, it is convenient to use a simplified scheme highlighting the different steps involved in radical pair generation.

3. the excited singlet state, $^1A^*$, can undergo *inter-system crossing* (ISC) to form the triplet excited state, $^3A^*$ (pathway denoted ISC in **Figure 2.6**).

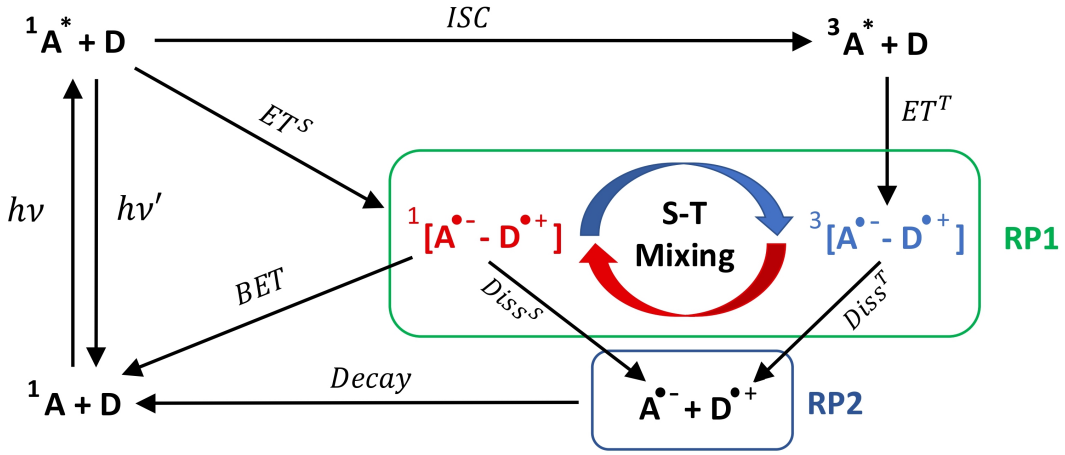


Figure 2.6 A simplified radical pair mechanism photocycle with an electron acceptor, A, and an electron donor, D. Following photoillumination, ^{1}A can absorb a photon and get photoexcited to the singlet excited state $^1A^*$ (step $h\nu$). It can then fluoresce back to the ground state (step $h\nu'$), undergo intersystem crossing to form the triplet photoexcited state $^3A^*$ (step ISC) or undergo electron transfer to produce RP1 $^1[A^{\bullet-}-\ D^{\bullet+}]$ in the singlet state (step ET^S). It can then produce a back-electron transfer (step BET) and decay back to the ground state or interconvert to the $^3[A^{\bullet-}-\ D^{\bullet+}]$ triplet state. Similarly, $^3A^*$ can generate RP1 $^3[A^{\bullet-}-\ D^{\bullet+}]$ in the triplet state (step ET^T), which can thus interconvert with $^1[A^{\bullet-}-\ D^{\bullet+}]$. RP1 can dissociate to create RP2 (steps $Diss^S$ and $Diss^T$ for $^1[A^{\bullet-}-\ D^{\bullet+}]$ and $^3[A^{\bullet-}-\ D^{\bullet+}]$, respectively), and essentially return to the ground state ^{1}A (step $Decay$).

If the system of study is of *intramolecular* nature, the intraprotein ET reaction usually takes places faster than the ISC [12], thus the second reaction scheme from the above is favored and a singlet-born radical pair is formed. It can then either undergo a *back-electron transfer* (BET) to recombine to the initial ground state[7], ^{1}A, or coherently interconvert into the triplet radical pair state.

However, if a molecule needs an external electron donor, the electron acceptor and donor species need to encounter first through diffusion. This falls under the *intermolecular* reaction scheme, where the ET is delayed and thus ISC happens faster [12], thereby forming the triplet photoexcited state, $^3A^*$. Through the ET sequence, a triplet-born radical pair can be formed, which can undergo coherent singlet-triplet mixing and interconvert into the singlet radical pair state.

[7]Under spin conservation rules, only the singlet state of the RP1 can recombine back to the ground state through BET, as direct recombination of the triplet state is forbidden.

In both circumstances, a magnetosensitive radical pair, named as RP1, is produced. With the various spin relaxation processes taking place at the same time (see **Section 2.1.4**), the two magnetically sensitive components of the RP1 eventually diffuse to form the photoproducts, termed as RP2, which can exist as free radicals or different protonation states of A and D. The two radical species eventually diffuse apart and decay back to the ground state.

2.2.2 Magnetic Sensitivity of Radical Pairs

The application of external magnetic fields reduces the efficiency of singlet-triplet interconversion, as the Zeeman interaction energetically separates the $|T_{\pm}\rangle$ states from $|S\rangle$ and $|T_0\rangle$ states in the high field region (see **Section 2.1.3**). This eliminates any other possible interconversion pathway than those between the $|S\rangle$ and $|T_0\rangle$ spin states, hence attenuating the overall singlet-triplet mixing mechanism. The produced concentrations of photoproducts, RP2, are directly enhanced through the application of magnetic fields [1, 15]. Such manifestation of changes, where the reaction product distributions and rate kinetics of the overall yield of the reaction are altered, are referred to as *magnetic field effects* (*MFEs*) [1, 13].

To provide a quantifiable response of how MFEs impact the RPM, MFEs are often calculated as percentage changes of the reaction products with and without applied magnetic fields, denoted as $\%$MFE. However, MFEs can be also indirectly recorded by measuring the ground state fluorescence intensity upon continuous illumination of the sample. This way, the magnetosensitive information of the re-excited ground state population can be accessed through fluorescence, which can only be collected upon relaxation of the singlet excited state (*cf.* **Figure 2.6**). It is, therefore, useful to express the $\%$MFE is terms of the excited state fluorescence intensity, I_f:

$$\%MFE = \frac{I_f(B) - I_f(B=0)}{I_f(B=0)} \cdot 100, \tag{2.34}$$

where the subscripts B and $B = 0$ indicate if the presence and absence of an external magnetic field, respectively.

Measuring MFEs over a range of magnetic field strengths results approximately in a Lorentzian curve, termed as *magnetically altered reaction yield* (*MARY*), illustrated in **Figure 2.7**.

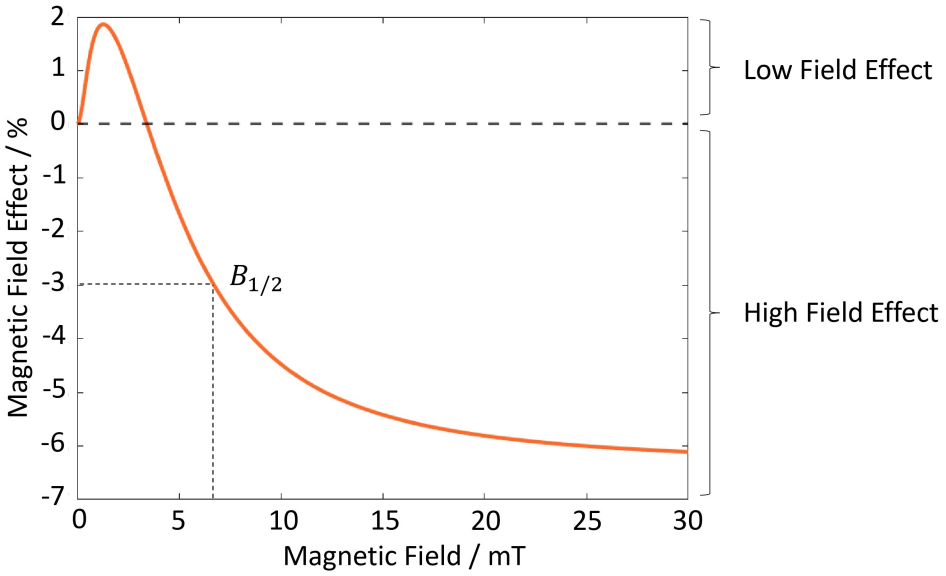


Figure 2.7 A qualitative diagram of a MARY curve, showing the low and high field effects. The width of the curve is characterised by the $B_{1/2}$ parameter.

It is a useful means of comparing the magnetic behaviours of different systems and/or different screening techniques, even those that are not capable of detecting changes in fluorescence intensities[8]. In the low field region, where the Zeeman and hyperfine interactions are comparable in strength, additional spin interconversion pathways are permitted. Such an increase in the singlet-triplet mixing efficiency is a result of the lifted degeneracies between the zero-field spin states, which leads to a positive MFE in singlet-born RPs [113, 140], and is known as the *low field effect (LFE)*. However, in the high field region, the Zeeman interaction hinders the interconversion of the triplet states and only $|S\rangle$ and $|T_0\rangle$ states can mix (see **Figure 2.3**), which results in a negative MFE. In addition, MARY curves display a characteristic parameter $B_{1/2}$, which defines the magnetic field value at which the MFE is equal to half its saturated limit. It is expressed from the Weller[9] equation [139]:

[8] In this case, **Equation 2.34** can be rewritten in terms of photoproduct concentrations with and without applied magnetic fields, which will allow to compare the spin chemistry through MARY plots.

[9] A recent paper by Wong *et al.* directly disagrees with this formula and states that it is only valid for small and short-lived ($\sim$ 5 ns) RPs in solution. Its credibility is, therefore, somewhat unreliable in the context of magnetoreception [139].

$$B_{1/2}^{W} = 2\sqrt{3}\left(\frac{\sigma_1^2 + \sigma_2^2}{\sigma_1 + \sigma_2}\right), \tag{2.35}$$

where the effective hyperfine coupling, σ_i, is defined for different radicals by:

$$\sigma_i = \sqrt{\frac{1}{3}\sum_k a_{ik}^2 I_{ik}\left(I_{ik}+1\right)}, \tag{2.36}$$

with a_{ik} is the isotropic hyperfine coupling of an electron i and the k^{th} nucleus, I_{ik} represents the spin quantum number of the k^{th} nucleus coupled to electron i.

In general, $B_{1/2}$ gives insights into spin relaxation processes, as it was found that the simulated values of $B_{1/2}$ in solutions do not entirely reflect the observed experimental values [139]. Therefore, by evaluating the hyperfine coupling contributions using **Equations 2.35** and **2.36**, information on spin dynamics of a specific system of study can be extracted.

2.3 Summary and Outlook

The theoretical background discussed in **Chapter 2** lays the groundwork for understanding the spin chemistry for fluorescence-based measurements on magnetically-sensitive RPs. Crys exhibit MFEs upon the application of external magnetic fields, which can be analysed through the subsequent fluorescence emission by their ground state consituants of the RPM.

The new technique presented in this thesis incorporates fluorescence microscopy coupled with microfluidic technology, which requires a certain comprehension of fluid mechanics involved in microflows. **Chapter 3** delves into the theoretical explanations of the physics behind microdroplet formation, followed by a detailed description of the experimental methods that integrate the concepts of microfluidics and quantum chemistry from **Chapters 2** and **3**.

Chapter 3

Methodologies of Droplet-Based Microfluidics

The RPM mechanism in Cry flavoprotein operates over a large range of time scales, typically showing initial changes in Cry biochemistry just picoseconds after the initial exposure to light, and expanding to minutes or hours upon accumulating long-lived RP species. As a result, these photoproducts exhibit significant variation in their absorption properties. Furthermore, MFEs generated in Cry proteins are usually small, which demands specialised spectroscopic techniques with significant sensitivity for accurate detection of MFEs. For these reasons, a variety of spectroscopic techniques must be applied in order to study the entire avian RPM photocycle.

MFEs in proteins are typically studied using fluorescence microscopy, electron paramagnetic resonance, optical absorption, and optical cavity-enhanced spectroscopic methods. However, these experiments require substantial amounts of protein samples since measurements are conducted in bulk. This poses multiple challenges to the experimental collection of data, as continuous illumination of a relatively unstable sample increases photodegradation processes inside Cry proteins, thereby damaging the sample over time. For this reason, recovery of the sample is necessary to restore it back to its ground state. Moreover, the difficulty and costs associated with the expression of Cry proteins add another level of complexity to the experiment, as only small quantities (usually less than a few milliliters) of the sample phase are usually available after around a month of their development.

These experimental constraints have prompted the development of a novel technique of microdroplet fluorescence, which makes use of microfluidic droplet generation to produce a monodispersed flow of thousands of minuscule protein samples contained

within microdroplets. By coupling such experimental configuration with confocal microscopy, it is possible to image single microdroplets of sizes down to 10 μm in diameter. This allows microfluidic screening of each microdroplet that acts as a separate microreactor of protein samples and allows the development of statistical analysis over many acquisitions of the magnetic field-induced changes on the photochemistry of Crys. Continuous illumination of moving microdroplets initiates the RPM mechanism inside the confined protein sample, and if the flow is subjected to varying magnetic fields, MFEs can be extracted through the analysis of the resulting fluorescence signal.

Such systems provide many advantages over traditional spectroscopic methods of MFE analysis. First and foremost, microfluidic droplet formation minimises sample consumption of proteins, which directly improves efficiency and cost-effectiveness by requiring significantly smaller amounts of limited and expensive reagents. The small scale and high surface area-to-volume ratio of each microdroplet enhances the photoreactive screening of samples, with an average of around 150 ms of illumination time per microdroplet. This directly tackles the photodegradation problem of Cry proteins, as no immediate degradation can take place within such a short time frame. Furthermore, microfluidics has remarkable versatility, offering large compatibility with other techniques. It allows real-time imaging of microdroplet formation, which facilitates rapid calibration and optimisation of experiments. Based on their precise control over droplet properties, microfluidic experiments can be tailored to the specific needs of different measurements by adjusting various experimental parameters. These include changing microdroplet flow rates, as well as microchannel diameter and geometry in which fluids flow, all of which contribute to the highly uniform droplet formation with narrow size distributions. Such homogeneity of sample size is critical for reproducibility of experiments, particularly when it comes to envisioning prospective screening of thousands of individual avian cells.

The following chapter presents a short introduction to microfluidics, the necessary concepts of fluid mechanics that outline how microdroplets are formed in microfluidic chips, and experimental methods of data acquisition and analysis.

3.1 Introduction to Microfluidic Technology

The field of *lab-on-a-chip* systems is a relatively new area of science that has experienced exceptionally rapid progress since its development in the 1980s [141]. The underlying principle of microfluidics is to process and manipulate liquids in microchannels, typically within the range of $10-100$ μm. This deviates from classical fluid mechanics describing macroscopic systems — a reduction in a linear scale of a liquid diameter by a factor of 10^{-3} corresponds to its volume reduction by a factor of 10^{-9}. Therefore, rather than working with 1 L or 1 mL of sample volume, *lab-on-a-chip* systems can efficiently manage analyses with volumes as small as 1 nL or 1 pL. The practical application of this is the dramatic minimisation of sample required, which is invaluable when working with sparse samples, such as Cry proteins. If we consider a standard microdroplet confined within a channel of 80 μm in diameter, the volume of each droplet is roughly equal to 268 pL. As a result, a total of 50 μL of Cry sample provides over 185,000 possible individual measurements, when normally around 200 μL of sample (four times as much!) is required for a single measurement in bulk.

Consequently, since the volumes of liquids of study are extremely small, the fluid physics in systems that transport liquids in the form of single microdroplets within enclosed channels are no longer governed by the fundamental force of gravity, and instead give rise to the predominant force of surface tension [142]. This factor significantly simplifies the equations describing the fluid mechanics of droplets, which make microfluidics a compelling method of analysis for researchers to investigate the properties and dynamics of fluid flows at high resolution.

The technological development of *lab-on-a-chip* systems has already transformed research areas of medical diagnostics, pharmacology, forensics, and synthetic chemistry [141]. All of these fields leverage the screening of tiny volumes of fluids passing through microchannels, with its most successful commercial applications being high-quality photo delivery via inkjet printing, high-performance micropumps for regular and precise drug delivery of insulin for diabetes care, as well as rapid and cost-effective high-throughput DNA sequencing [141, 143, 144].

The ultimate goal of microfluidics is to develop entire laboratories on a single chip, as its name of *lab-on-a-chip* suggests. The basic idea of these miniaturised platforms is to integrate various assay operations, ranging from analytical detection to sample pre-treatment and preparation [145]. This is already somewhat a reality as the new cutting-edge application of *organ-on-a-chip* has emerged, seeking to recreate the physiological and mechanical microenvironment of human organs in a three-dimensional configuration. This miniaturised technology mimics the extracellular environment and tissue architecture of a human body, which provides tremendous potential to revolutionise the field of drug development, disease modeling, and personalised medicine by providing a more accurate and physiologically relevant alternative to traditional cell culture and animal models.

A crucial challenge for these applications of microfluidics consists of precisely controlling and manipulating fluid flow rates to deliver droplets of predictable volumes. To enable the effective use of fluidic microsystems, a thorough understanding of the physical behaviour of fluids at the micro-regime is necessary. Therefore, is it important to describe the most relevant theory of fluid mechanics in order to understand microdroplet formation, which is at the experimental core of the technique used in this research project.

3.2 Laws of Fluid Motions

Fluid mechanics is a branch of physics that studies the behaviour of fluids — either liquids or gases — in motion and at rest. In particular, fluid physics defines how fluids deform under the action of external forces (such as pressure or temperature change) and how they interact with solid boundaries.

A fluid is defined as a substance with no preferred shape, allowing its different portions to be freely arranged under continuous influence of external forces without modifying its overall properties. From a molecular point of view, fluids demonstrate discrete quantisation through separation from the other phases by an interface up to a few nm thick [146]. However, microfluidic flows are generally treated as a *continuous*

medium in most *lab-on-a-chip* applications, since fluid behaviour in the micrometer dimensions is governed by macroscopic fluid mechanics principles rather than molecular dynamics that takes place on the micro- or nanoscale.

3.2.1 The Continuity Hypothesis

The macroscopic characteristics of fluids can be treated as a perfectly continuous structure, rather than, in reality, a combination of individual molecules. This implies that any small volume element within the fluid is assumed to be sufficiently large to consist of a considerable amount of molecules [147]. Such a framework can be established by describing different fluid properties (*e.g.* velocity, pressure, density, etc.) in terms of fields using two distinct ways:

1. using the *Eulerian* approach, where the evolution of fluid field properties over time can be observed at fixed positions in space;
2. using the *Lagrangian* approach, where the evolution of individual fluid particles can be tracked as they move across the trajectory of the fluid.

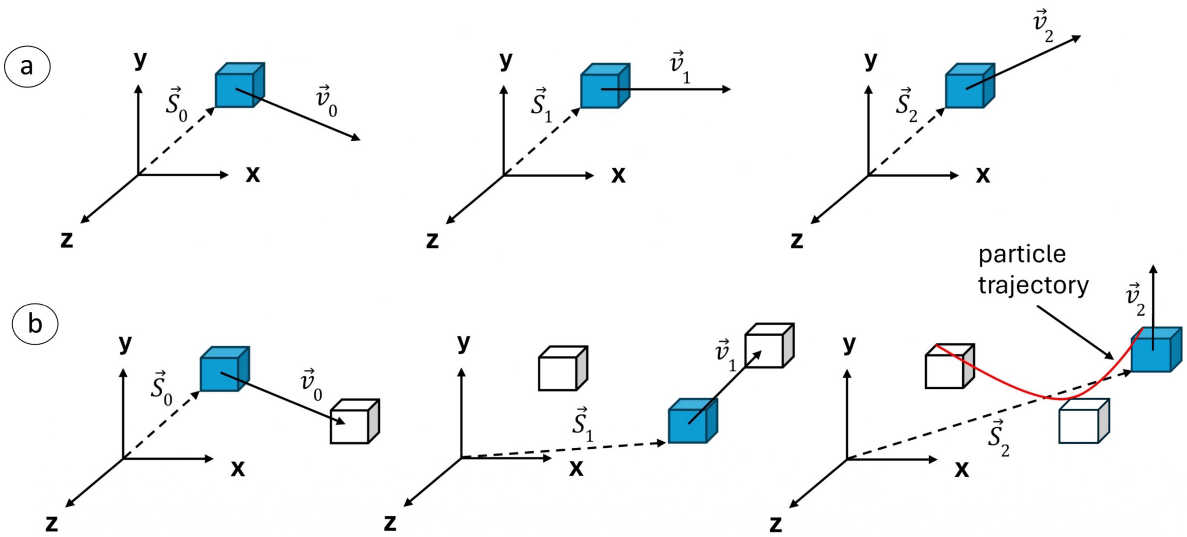


Figure 3.1 Visual representations of (a) the *Eulerian* description, where the frame of reference is fixed in space, and (b) the *Lagrangian* description, where the frame of reference moves in space along the trajectory of the fluid flow.

Both of these approaches provide solid frameworks to analyse fluid fields, however, the *Eulerian* description makes it more simple to study microfluidic flows that comprise vast numbers of particles. Considering that there are over thousands of molecules

in a single cubic micrometer of space inside a microdroplet, the application of the *Lagrangian* method to each individual particle would present a significant challenge even for the most powerful computational facilities available today [148].

For this reason, the continuity hypothesis will be described with the help of the Eulerian description, using which the fluid field can be described as follows [142]:

$$F(\boldsymbol{r}, t) = \langle F_{mol}(\boldsymbol{r}', t) \rangle_{\boldsymbol{r}' \in \Delta V(\boldsymbol{r})} , \tag{3.1}$$

where $F(\boldsymbol{r}, t)$ is defined as the flow field that evolves in time, t, over any fixed position in space, $\boldsymbol{r}$, and $\langle F_{mol}(\boldsymbol{r}', t) \rangle$ corresponds to the averages of all molecular values of molecules contained in a single fluid particle of arbitrary volume, $\Delta V(\boldsymbol{r})$.

In classical mechanics, the principle of conservation of matter declares that mass remains constant over time; it cannot suddenly appear or vanish. When delving into the dynamics of fluids, this concept translates into the notion that the flow of matter through a defined region of space, Σ, must correspond to the quantity of mass that enters and exits Σ.

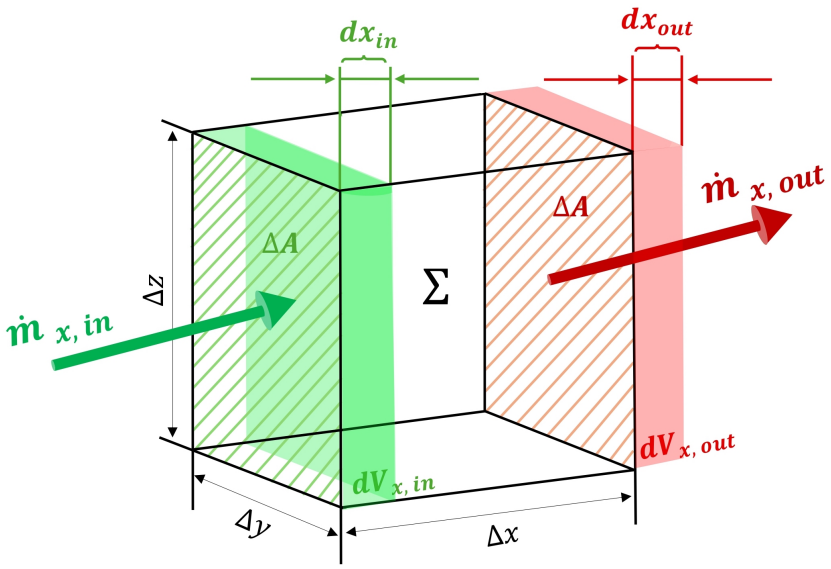


Figure 3.2 Infinitesimal control volume of an arbitrary region of space, Σ, for the derivation of the mass current density, $\boldsymbol{J}$.

The total mass of fluid, $M(\Sigma, t)$, confined within Σ can be expressed as a volume integral of the contained density of the fluid, $\rho(\boldsymbol{r}, t)$, over the whole surface surrounding the volume in question [142]:

$$M(\Sigma, t) = \int_{\Sigma} \rho(\boldsymbol{r}, t)\, d\boldsymbol{r}, \tag{3.2}$$

where $d\boldsymbol{r}$ is the Cartesian coordinate integral in the x, y and z direction.

Since Σ is taken as a fixed region in space, $M(\Sigma, t)$ may only vary over time. If we consider the net flow to be directed outwards, the overall change of mass flowing through Σ can be expressed either as a volume integral that decreases over time:

$$\frac{\partial}{\partial t} M\left(\Sigma, t\right) = -\frac{\partial}{\partial t} \int_{\Sigma} \rho(\boldsymbol{r}, t)\, d\boldsymbol{r}, \tag{3.3}$$

or equally, as a surface integral over $\partial\Sigma$:

$$\frac{\partial}{\partial t} M\left(\Sigma, t\right) = \int_{\partial\Sigma} \rho(\boldsymbol{r}, t)\boldsymbol{u}(\boldsymbol{r}, t) \cdot \boldsymbol{n}\, dA \tag{3.4}$$

where $\boldsymbol{u}(\boldsymbol{r}, t)$ describes the *Eulerian* velocity field, dA is the infinitesimal surface area bounding $\partial\Sigma$, and $\boldsymbol{n}$ is the unit vector directed along the normal. By definition, this flow of mass can be expressed as the mass current density $\boldsymbol{J}(\boldsymbol{r}, t)$:

$$\boldsymbol{J}(\boldsymbol{r}, t) = \rho(\boldsymbol{r}, t)\boldsymbol{u}(\boldsymbol{r}, t) \tag{3.5}$$

which is positive if the fluid flows out of the volume, and negative if the flow is directed in the direction opposite to the normal.

According to the principle of conservation of mass, the rate of change of mass flowing into the region Σ must equal the net mass flux flowing out of the volume. Thus, **Equations 3.3** and **3.4** must be equal:

$$\int_{\partial\Sigma} \boldsymbol{J}(\boldsymbol{r}, t) \cdot \boldsymbol{n}\, dA = -\frac{\partial}{\partial t} \int_{\Sigma} \rho(\boldsymbol{r}, t)\, d\boldsymbol{r}. \tag{3.6}$$

The surface integral on the left side of **Equation 3.6** can be converted to a volume integral using Gauss' theorem [142]:

$$\int_{\partial\Sigma} \boldsymbol{J}(\boldsymbol{r}, t) \cdot \boldsymbol{n}\, dA = \int_{\Sigma} \nabla \cdot \Big(\boldsymbol{J}(\boldsymbol{r}, t)\Big)\, d\boldsymbol{r}, \tag{3.7}$$

Using **Equations 3.6** and **3.7**, the terms inside the integral can be combined as follows:

$$\int_{\Sigma} \left(\frac{\partial}{\partial t}\rho(\boldsymbol{r}, t) + \nabla \cdot \boldsymbol{J}(\boldsymbol{r}, t)\right) d\boldsymbol{r} = 0. \tag{3.8}$$

Since **Equation 3.8** must hold for any arbitrary volume Σ, the integrand must be zero:

$$\frac{\partial}{\partial t}\rho(\boldsymbol{r},t) + \nabla \cdot \boldsymbol{J}(\boldsymbol{r},t) = 0. \tag{3.9}$$

Equation 3.9 is known as the *continuity equation* which shows that any change in density of the fluid, $\rho(\boldsymbol{r},t)$, over time is directly related to the divergence of the mass current density, $\boldsymbol{J}(\boldsymbol{r},t)$. Simply put, in fluid mechanics, this change in mass is linked to the movement of compressible fluids, which physically describes the conservation of mass.

However, it is reasonable to assume that fluids in microfluidic systems are *incompressible*, meaning that their density remains constant $\left(\frac{\partial}{\partial t}\rho(\boldsymbol{r},t) = 0\right)$ throughout their motion, even under changes in pressure or temperature [142]. Taking this into account, **Equation 3.9** can be reduced to the following:

$$\nabla \cdot \boldsymbol{u}(\boldsymbol{r},t) = 0. \tag{3.10}$$

The incompressibility approximation in the continuity equation implies that there is no net fluid flow into or out of the arbitrary fixed volume Σ. This means that any amount of fluid entering any small volume is equal to the amount of fluid leaving that volume.

3.2.2 The Navier-Stokes Equation

The Navier-Stokes equation represents a fundamental principle in fluid mechanics that mathematically describes the behaviour of any fluid flow — from the slow viscous flow of honey to the rapid and turbulent airflow around an airplane wing. It is generally used to predict the weather and ocean currents, model the airflow around vehicles to aid their design development, and can be applied to study multiphased microfluidic flows, such as blood flow in the human body's arteries to optimise drug delivery devices.

In fluid mechanics, the Navier-Stokes equation can be derived from Newton's second law of motion for a solid object:

$$m\frac{d\boldsymbol{v}}{dt} = \sum_i \boldsymbol{f_i}, \tag{3.11}$$

where $\boldsymbol{f}$ represents forces per unit volume, known as *force densities*.

In the context of a fluid, we apply this principle to an infinitesimal fluid element, such as Σ, in which the mass of fluid is defined using **Equation 3.2** and the velocity is described as the *Eulerian* velocity field, $\boldsymbol{u}(\boldsymbol{r}, t)$. This translates **Equation 3.11** to the following:

$$\rho(\boldsymbol{r}, t)\frac{d}{dt}\boldsymbol{u}(\boldsymbol{r}, t) = \sum_i \boldsymbol{f_i}. \tag{3.12}$$

The derivative of $\boldsymbol{u}(\boldsymbol{r}, t)$ over time yields the following result:

$$\begin{aligned}\frac{d}{dt}\boldsymbol{u}(\boldsymbol{r}, t) &= \frac{\partial \boldsymbol{u}}{\partial t} + \left(\frac{\partial \boldsymbol{u}}{\partial x}\right)\left(\frac{dx}{dt}\right) + \left(\frac{\partial \boldsymbol{u}}{\partial y}\right)\left(\frac{dy}{dt}\right) + \left(\frac{\partial \boldsymbol{u}}{\partial z}\right)\left(\frac{dz}{dt}\right) \\ &= \frac{\partial \boldsymbol{u}}{\partial t} + \frac{d\boldsymbol{r}}{dt} \cdot \nabla \boldsymbol{u}.\end{aligned} \tag{3.13}$$

By definition, velocity is the rate of change of position with respect to time. Hence, for the velocity field, $\boldsymbol{u}(\boldsymbol{r}, t)$, this definition translates to a change of path taken by some object through the fluid, $\boldsymbol{r}$, over time: $u = \frac{d\boldsymbol{r}}{dt}$. Therefore, we can rewrite **Equation 3.13** as follows:

$$\frac{d}{dt}\boldsymbol{u}(\boldsymbol{r}, t) = \frac{\partial \boldsymbol{u}}{\partial t} + (\boldsymbol{u} \cdot \nabla)\boldsymbol{u}. \tag{3.14}$$

This definition can be used to modify **Equation 3.12** in the following way:

$$\rho(\boldsymbol{r}, t)\left(\frac{\partial \boldsymbol{u}}{\partial t} + (\boldsymbol{u} \cdot \nabla)\boldsymbol{u}\right) = \sum_i \boldsymbol{f_i}. \tag{3.15}$$

For a fluid, $\boldsymbol{f}$ represents body force densities, which act across the entire fluid volume and usually take on the following form:

$$\sum_i \boldsymbol{f}_i = \boldsymbol{f}_{pres} + \boldsymbol{f}_{visc} + \boldsymbol{f}_g + \boldsymbol{f}. \tag{3.16}$$

The total external force $\boldsymbol{f}_{pres}$ acting on Σ due to the pressure, p, is given by the following surface integral:

$$\boldsymbol{f}_{pres} = -\int_{\partial\Sigma} p \cdot \boldsymbol{n}\, dA = -\int_{\Sigma} \nabla p\, d\boldsymbol{r}, \tag{3.17}$$

where the minus sign is necessary to ensure that p acts in the opposite direction to the outward normal vector of the surface, $\boldsymbol{n}$. The second equality in **Equation 3.17** is found by applying Gauss' theorem. The integrand of the volume integral can,

therefore, be identified as the force density due to the pressure:

$$\boldsymbol{f}_{pres} = -\nabla p. \tag{3.18}$$

Particles moving through viscous fluids experience linear drag that physically manifests as friction. This causes liquids to move at different speeds and gives rise to the viscous force [142]:

$$\boldsymbol{f}_{visc} = \eta \nabla^2 \boldsymbol{u}, \tag{3.19}$$

where η is the dynamic shear viscosity of a fluid.

The gravitational force can be expressed directly using Newton's second law of motion for a fluid (*cf.* **Equation 3.12**), where the derivative of the velocity field, $\boldsymbol{u}(\boldsymbol{r}, t)$, over time gives fluid particle acceleration due to the gravitational pull:

$$\boldsymbol{f}_g = \rho g, \tag{3.20}$$

where g is the standard gravitational acceleration constant.

The final Navier-Stokes equation can thus be developed if we substitute **Equations 3.18**, **3.19** and **3.20** into **Equation 3.15**:

$$\rho(\boldsymbol{r}, t) \left(\frac{\partial \boldsymbol{u}}{\partial t} + (\boldsymbol{u} \cdot \nabla)\boldsymbol{u} \right) = -\nabla p + \eta \nabla^2 \boldsymbol{u} + \rho g + \boldsymbol{f}, \tag{3.21}$$

where $\boldsymbol{f}$ represents any other influencing forces per unit volume. In the case of microfluidic flows, gravity can be neglected (as described in **Section 3.1**), which simplifies **Equation 3.21** to the following form:

$$\rho(\boldsymbol{r}, t) \left(\frac{\partial \boldsymbol{u}}{\partial t} + (\boldsymbol{u} \cdot \nabla)\boldsymbol{u} \right) = -\nabla p + \eta \nabla^2 \boldsymbol{u} + \boldsymbol{f}. \tag{3.22}$$

The mathematical equation presented above is the fundamental equation of fluid motion for the majority of microfluidic systems [142]. The left-side of **Equation 3.22** represents inertial acceleration of fluid particles, which consists of *time-dependent acceleration*, $\rho(\boldsymbol{r}, t)\frac{\partial \boldsymbol{u}}{\partial t}$, which describes how the velocity at a specific location of the fluid changes as time progresses, and *convective acceleration*, $\rho(\boldsymbol{r}, t)(\boldsymbol{u} \cdot \nabla)\boldsymbol{u}$, which takes into account that fluid particles experience different velocities upon moving through spatially varying flow fields [149].

3.3 Physics of Microdroplet Formation

The origin of microdroplet formation in narrow channels stems from fluid instabilities [150]. In bulk solution of a liquid, molecules of the same fluid experience cohesive attraction as a result of chemical bonds formed between individual molecules and interact with neighboring molecules on all sides. The intermolecular forces acting between them (e.g. hydrogen bonding, van der Waals forces, electrostatic attraction between ions, etc.) create a balanced, net zero force acting on each molecule, leading them to interact uniformly with their surrounding molecular environment.

If two immiscible fluids are introduced into one another, they will separate into two distinct phases and form a liquid-liquid interface, which is a geometrical surface of a few nm thick [146] delimiting two fluid domains. At the contact of the interface, molecules are not surrounded by other liquid particles in all directions; instead, they are exposed to another fluid phase. This leads to fewer interactions taking place, which creates an imbalance in intermolecular forces acting on surface molecules, and generates an inward pull from the surface toward the bulk solution (see **Figure 3.3**). This phenomenon is known as *surface tension*, which seeks to minimise the surface

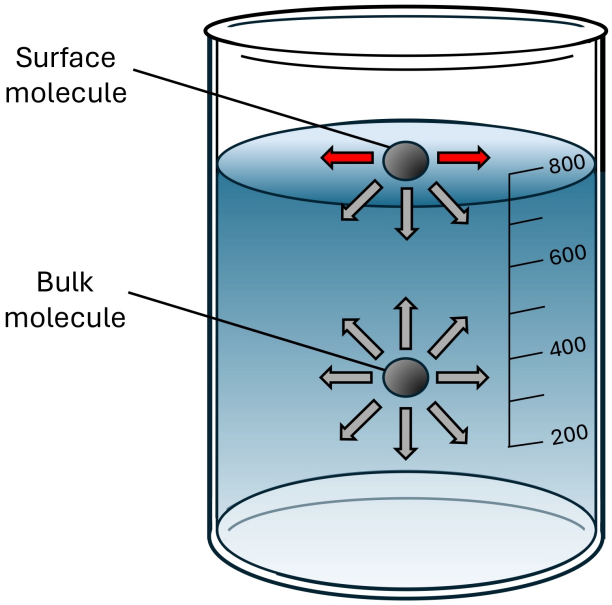


Figure 3.3 Vectorial visualisation of forces acting on molecules inside a liquid. A bulk molecule located away from the surface is pulled equally in all directions by neighboring liquid molecules. However, at the surface, molecules are not surrounded by other molecules on all sides. This creates an inward pull, causing the liquid surface to contract to the smallest area possible.

area of the fluid according to the second law of thermodynamics (see **Appendix B**).

In the presence of two different molecular environments — such as two different immiscible fluids — adhesive forces between the surfaces of fluid bodies permit the bonding of one material to another. They contribute to interfacial tension, and if adhesive forces are weaker than intermolecular forces, droplets generally take on a symmetric spherical shape. This is because each point on the surface of a sphere is at an equal distance from the centre of the sphere, which geometrically produces the smallest surface area for a given volume (see **Appendix B.3**).

3.3.1 Interface Formation of Two-Phase Microflows

Generally, the dynamics of each immiscible fluid in a two-phase flow is characterised by the Navier-Stokes equation (see **Equation 3.22**). However, appropriate modeling of fluid flows in microchannels requires imposing boundary conditions that address the formation of interfaces.

Any fluid moving along a solid surface will experience *shear stress* that arises due to deformation between the adjacent layers of fluid flows [150]:

$$\boldsymbol{\tau}(\boldsymbol{u}) = \eta \left(\nabla \boldsymbol{u}(\boldsymbol{r}) + [\nabla \boldsymbol{u}(\boldsymbol{r})]^T \right). \tag{3.23}$$

Near solid boundaries — such as a microfluidic chip channel wall — fluid particles adhere to the surface upon contact and resist motion, causing their velocity fields at the liquid-chip interface to be zero [142, 150]:

$$\boldsymbol{u}(\boldsymbol{r}) = 0. \tag{3.24}$$

This is known as the *no-slip boundary condition*, for which $\boldsymbol{r} \in \partial\Sigma$, and is defined for an arbitrary microchannel volume, $\partial\Sigma$.

Due to the *no-slip* condition, the immediate layer of fluid in direct contact with the wall is stationary. The next layer just above it moves slightly faster, as does the next one, and so on. Moving away from the *no-slip* boundary towards the centre of the microchannel, the shear stress becomes gradually weaker and causes the development of

a parabolic velocity field gradient within the fluid (see **Figure 3.4**). This constitutes a liquid-liquid interfacial boundary, which stems from the continuity of normal velocity fields at the interface between two immiscible fluids [150]:

$$\boldsymbol{u}_d(\boldsymbol{r}, t) \cdot \boldsymbol{n} = \boldsymbol{u}_c(\boldsymbol{r}, t) \cdot \boldsymbol{n}, \tag{3.25}$$

where $\boldsymbol{n}$ is the unit normal vector toward the liquid-liquid interface and the subscripts c and d define the carrier (non-fluorescent) and disperse (photoreactive) phases, respectively.

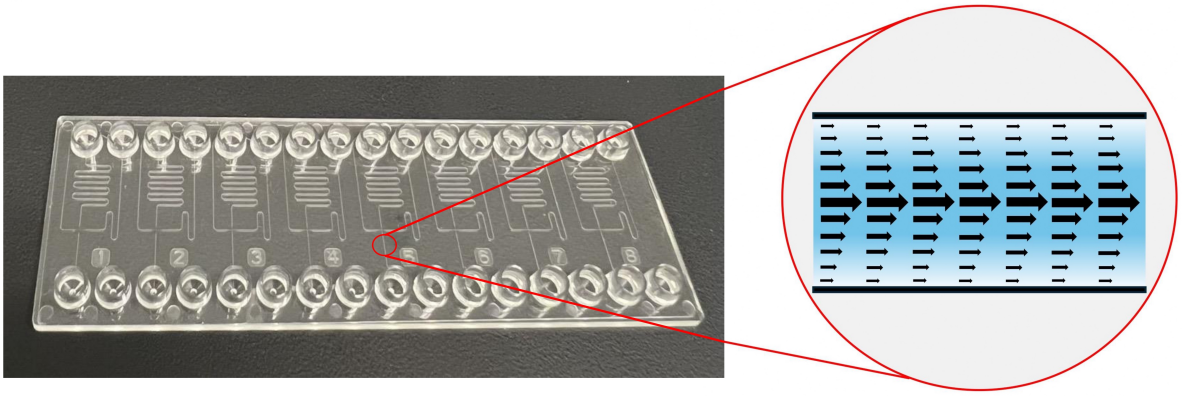


Figure 3.4 Photo of a flow-focusing microfluidic chip used for microfluidic experiments presented in this thesis (left) and an illustrative picture of a what a parabolic velocity field profile across a cross-section of a single microfluidic channel would look like (right).

Just as velocity fields are continuous at the liquid-liquid interface (see **Equation 3.25**), the continuity of forces at the contact is ensured as well [150]:

$$\boldsymbol{\tau}_d(\boldsymbol{u}) \cdot \boldsymbol{t} = \boldsymbol{\tau}_c(\boldsymbol{u}) \cdot \boldsymbol{t}, \tag{3.26}$$

where $\boldsymbol{t}$ is the unit tangent vector to the interface between the two fluids. From here, the *exact interface stress condition* can be expressed as the stress balance equation:

$$\boldsymbol{T}_d \cdot \boldsymbol{n} - \boldsymbol{T}_c \cdot \boldsymbol{n} = \gamma\, \boldsymbol{n}\, (\nabla \cdot \boldsymbol{n}) - \nabla\gamma, \tag{3.27}$$

where $\boldsymbol{T} = -p\boldsymbol{I} + \boldsymbol{\tau}(\boldsymbol{u})$ is the stress tensor and γ is the interfacial tension. The divergence of the unit normal, $\nabla \cdot \boldsymbol{n}$, describes the geometry of the local curvature of the interface, while $\nabla\gamma$ is the tangential stress associated with gradients of the interfacial tension. If **Equation 3.27** is projected along the unit normal $\boldsymbol{n}$, the liquid-liquid

interface condition can be written separately as the *normal stress balance*:

$$\boldsymbol{n} \cdot (\boldsymbol{T}_d - \boldsymbol{T}_c) \cdot \boldsymbol{n} = \gamma \left(\nabla \cdot \boldsymbol{n} \right); \tag{3.28}$$

or the *tangential stress balance* if its projected along the unit tangent vector $\boldsymbol{t}$:

$$\boldsymbol{n} \cdot (\boldsymbol{T}_d - \boldsymbol{T}_c) \cdot \boldsymbol{t} = \nabla \gamma \cdot \boldsymbol{t}. \tag{3.29}$$

These conditions are critical in determining the pressure differences across curved interfaces — such as that of a microdroplet — and hence the overall shape and stability of the fluid surrounded by the liquid-liquid interface.

3.3.2 Dimensionless Numbers

In microflows, fluid motion with distinct characteristics can arise, typically governed by competing physical effects. Using the laws of fluid mechanics, these are usually quantified by *dimensionless numbers*, which, in essence, define a ratio of two relative forces. The main governing forces for droplet formation are the viscous, inertial, capillary and gravitational forces. However, in the case of microfluidic flows, gravity always has a significantly smaller effect than any other force due to the volume of the fluid (see **Section 3.1**), and, therefore, is typically neglected.

The *Reynolds number*, Re, predicts laminar to turbulent fluid flow patterns by measuring the ratio of inertial and viscous forces, and is defined as [150]:

$$Re_s = \frac{\rho_s u_s L}{\eta_s}, \tag{3.30}$$

where L is the diameter of the microchannel in which fluids flow, and the subscript s can be used to describe either the carrier or dispersed phases. At low Reynolds number values ($Re < 2000$), fluid flow is typically characterised as *laminar*, in which fluid particles move in orderly motion with minimal mixing between them (as depicted in **Figure 3.4**). Instabilities in flow patterns begin to develop at the intermediate flow regime characterised by the values of $2000 < Re < 4000$, whereas at high Reynolds numbers (typically $Re > 4000$), the fluid flow becomes *turbulent*, where fluid particles move in a chaotic manner with significant mixing.

The continuity equation for incompressible fluids states that fluid density, $\rho_s(\boldsymbol{r}, t)$, remains constant throughout the entire fluid flow (see **Equation 3.10**). In addition, the dynamic shear viscosity of a fluid, η_s, is determined by the fluid's molecular composition and is, therefore, an intrinsic property of the fluid. Taking this into account, for microfluidic flows, $Re \sim u_s L$, which is considerably reduced in microsystems [151]. The small channel size constrictions of microfluidic flows yield Re values between 10^{-6} and 10, thus always resulting in a laminar flow [150]. The typical Re numbers governing the microflows presented this thesis are $\sim$ 0.2 and $\sim$ 0.02 for the carrier and dispersed phases, respectively.

Using the incompressibility approximation (see **Equation 3.10**) and by negligible inertial forces compared to viscous forces (as indicated by the low Re numbers above), **Equation 3.22** can be simplified to the following form:

$$\mu \nabla^2 \mathbf{u} = \nabla p. \tag{3.31}$$

The *Capillary number*, Ca, is particularly important in the study of two-phase flows. It defines the shape of the interface between the two fluids and is expressed as the ratio between viscous and capillary forces [150]:

$$Ca_s = \frac{\eta_s u_s}{\gamma}. \tag{3.32}$$

At low capillary number values ($Ca < 10^{-2}$), the stress due to interfacial tension of the system is stronger than the viscous force, which leads to the formation of well-defined and stable interfaces. This causes immiscible microdroplets to retain non-spherical, elongated shapes [152] and allows for reproducible microdroplet formation, as surface tension forces provide minimal variations in droplet size. If high values of capillary number are achieved ($Ca > 1$), viscous forces overtake the interfacial tension, and significant deformations of the interface can take place upon microdroplet generation [152]. This can result in frequent droplet breakup and challenges in controlling droplet sizes, to even a continuous flow of both phases rather than a segmented microdroplet stream. In the case of microfluidic flows, microdroplet generation results in Ca values between 10^{-3} and 10 [150, 152]. The microflows described in this thesis

are characterized by Ca numbers ranging from ~ 1.3 and ~ 0.004 for the carrier and dispersed phases, respectively.

3.3.3 Droplet Breakup Modes in Microfluidic Chips

In microflows, specific breakup modes determine how droplets are formed, and depend on the surface tension of the interface between the two liquids, as well as additional energy input by external elements[1]. Because microdroplet formation occurs at the junction of the microfluidic device, the specific geometry of the microchannel dictates the nature of droplet breakup modes. For droplet-based microfluidic techniques, *co-flow*, *cross-flow* (also known as *T-junction*) and *flow-focusing* (or *double T-junction*) geometries are mostly used [150, 152], all of which are shown in **Figure 3.5**.

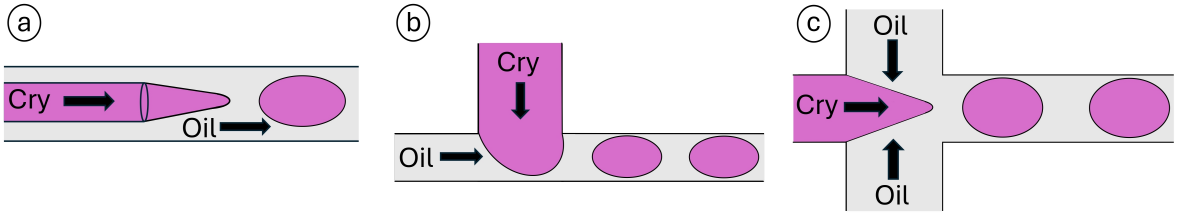


Figure 3.5 Schematics of a (a) co-flow, (b) cross-flow and (c) flow-focusing microfluidic chip junctions, showing Cry encapsulation in microdroplets.

In all of these microfluidic chips, the dispersed and carrier phases are driven independently up to a junction, where the two phases encounter and form a stable stream of monodispersed droplets. In *co-flowing* microsystems, the dispersed and carrier phases flow in parallel streams individually, until the dispersed phase flow reaches the end of its channel. At this point, it is injected into the carrier phase flow and breaks into microdroplets upon forming an interface. In *cross-flowing* microsystems, dispersed and carrier phases flow orthogonally, and form microdroplets upon encountering at a T-shaped junction. Lastly, in *flow-focusing* microsystems, the dispersed phase is squeezed by two counter-flowing streams of the continuous phase. This results in microdroplets being pinched off into the uniform stream of the carrier phase that evacuates microdroplets toward the end of the microchannel.

[1]Supplementary supply of energy, such as pressure regulators and centrifugal controls, modifies the force balance on the interface, thus adding another level of controllability in modulating droplet formation [150].

Each of these different junction geometries result in microdroplet formation, the process of which can be generally divided into three main parts [153]:

1. the formation of an immiscible interface of the dispersed and carrier phases at the microchannel junction (**Figure 3.6 a**);

2. deformation of the interface to an unstable state (**Figure 3.6 b** and **c**);

3. formation of a new microsystem through the breaking of the interface into microdroplets, each of which is surrounded by its own interface (**Figure 3.6 d**).

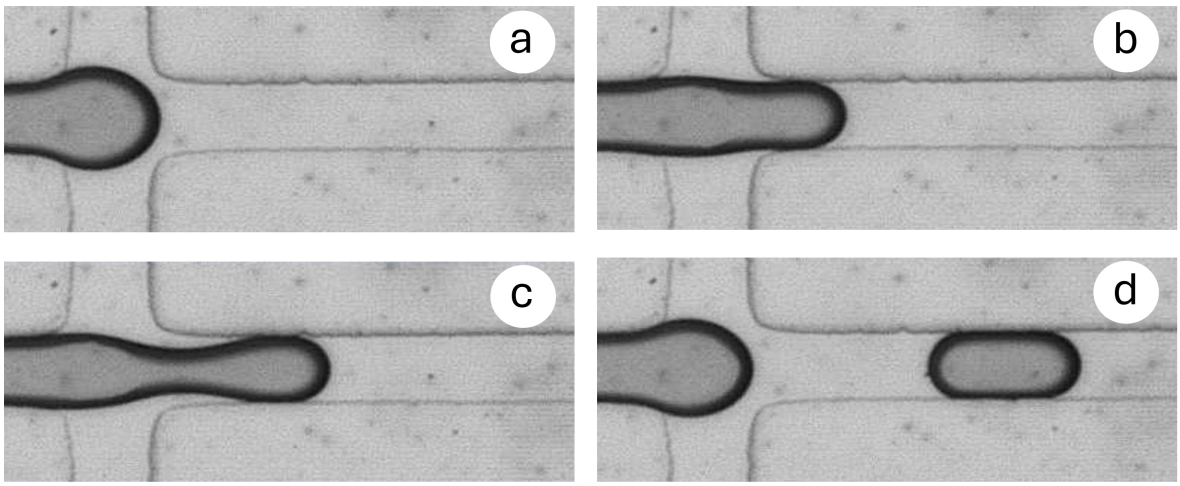


Figure 3.6 Snapshots of microdroplet formation in a flow-focusing microfluidic chip. (a) The dispersed phase (dark gray colour) comes into contact with the carrier phase (transparent colour) and forms an interface. (b) The dispersed phase starts to exit the junction and (c) gets squeezed by two counter-flowing streams of the carrier phase. (d) The dispersed phase detaches from the continuous flow as a separate microdroplet is formed.

In the case of flow-focusing microsystems, the initial formation of an immiscible interface happens when the dispersed phase is squeezed by two counter-flowing streams of the continuous phase. Because of external hydrodynamic forcing[2], the squeezed thread of the dispersed phase starts to thin down [154] until the thread size becomes minimal compared to the width of the microchannel. As the equilibrium of interfacial forces is reached, a plug-like shape of the microdroplet is adopted, and the

[2]Usually, pressure regulators are used to apply a pressure difference between the inlet and outlet of the microchannel to drive the fluid flow. Based on specific experiments, electric and magnetic fields or the use of pumps might be applied to induce fluid movements [150].

squeezed neck further constricts until the interface breaks. At this point, complete encapsulation of the dispersed phase into individual droplets takes place, and a separate microdroplet is formed.

3.4 Droplet Transport Phenomena

Once microdroplets are formed, they stay in motion and are carried along the microfluidic channel by the continuous stream of the carrier phase. If the size of the microchannel is drastically wider than the diameter of the microdroplet, they will flow at the local velocity of the carrier phase [152]. Differences in velocities shall be seen, as microdroplets near the centre of the microchannel flow at higher speeds compared to those near the sides (see **Figure 3.4**). However, if the diameter of the microdroplet matches the width of the microchannel, the flow of such microdroplets significantly depends on the capillary effects and interface deformability [152]. In this section[3], the influence on microdroplet velocity induced by film lubrication and irregular flow fields caused by immiscible interfaces are discussed.

3.4.1 Film Lubrication and Microdroplet Velocity

The local flow field in microfluidic chips is influenced by the physical properties of the fluids (interfacial tension and viscosity), the distribution of flow rates, and the contact with the microchannel walls. As the microdroplet flows throughout the channel, a thin layer of the carrier phase forms in between the droplet and the channel walls [155]. From a microdroplet's perspective that moves from left to right, the walls of the microchannel move in the opposite direction with velocity $-V_d$ and drag the carrier phase from right to left, which creates a *coating film* in between the interface of the microdroplet and the walls [152] (see **Figure 3.7a**). The interplay between the viscous and shear forces defines the thickness of the lubrication film, e, which can be compared to the capillary number, Ca, as it is expressed as the ratio between the two forces (see **Equation 3.32**) [156]:

$$\frac{e}{H} \propto Ca^{\frac{2}{3}}, \tag{3.33}$$

[3]For the sake of simplicity, complete wetting of the microchannel walls by the carrier phase is assumed in this section, and only a circular geometry of the microchannel is taken into account.

where H is the diameter of the microchannel of study. This equation is valid for $Ca < 0.01$ [157], and is, therefore, relevant to microfluidic flows.

The microdroplet velocity fields are directly impacted by the lubrication films, as the microdroplet, at any given point, must move in greater speed than the carrier phase [156]:

$$\frac{\boldsymbol{u}_d(\boldsymbol{r},t) - \boldsymbol{u}_c(\boldsymbol{r},t)}{\boldsymbol{u}_d(\boldsymbol{r},t)} \propto -Ca^{\frac{1}{3}}, \tag{3.34}$$

where subscripts d and c denote droplet and carrier phase velocity fields, respectively. In the case of $10^{-6} < Ca < 1$, the difference in velocity fields remains below 6% [158].

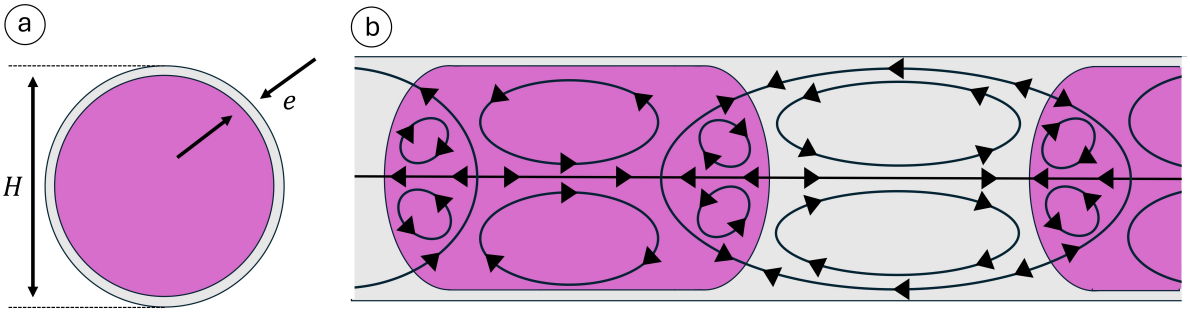


Figure 3.7 (a) Cross-section view of a microdroplet in a circular microchannel of diameter H and lubrication film of thickness e. (b) Topology of internal mixing currents caused by the presence of immiscible interfaces between the dispersed and carrier phases. Adapted from Hodges *et al.* [159].

3.4.2 Microflow fields and mixing currents

The presence of immiscible interfaces between the carrier and dispersed phases induces mixing flow fields inside each microdroplet. As explained in **Section 3.3.1**, the mean field velocity inside a microchannel is maximised along the central line. However, in the presence of a microdroplet large enough to occupy approximately the total width of the microchannel, the non-mixing nature of the two immiscible phases modifies this flow field in two ways. Firstly, due to surface tension, viscous and drag forces, the velocity field of a moving microdroplet, $\boldsymbol{u}_d(\boldsymbol{r},t)$, is usually smaller than the maximum velocity field of the carrier phase flow, $\boldsymbol{u}_c(\boldsymbol{r},t)$ [152]. As a result, fluid particles moving with a velocity higher than that of a microdroplet will eventually come into contact with the microdroplet and change their flow direction upon reaching the interface. This induces internal advection currents inside each microdroplet

(see **Figure 3.7b**), which depend significantly on the capillary number and the geometric characteristic of the microchannel [160]. Secondly, the creation of thin films in between the walls of the microchannel and the microdroplet at which the field velocity is considered to be zero (see **Equation 3.24**) induces internal flow patterns in the opposite direction to that of the microdroplet flow [161]. Both of these effects destabilise flowing patterns inside the microdroplet, causing complex mixing currents that, in some cases, may enhance the photoreactivity of each microsystem, which is further explored in **Section 4.3**.

3.5 Working Principles of Microdroplet Fluorescence Experiment

As outlined in the preface of **Chapter 3**, the key principle of the microdroplet fluorescence experimental technique is encapsulating the bulk phase of the photoreactive sample into a plethora of microdroplets — each of which acts as a separate microreactor and, therefore, as an individual experiment. This requires the usage of a flow-focusing microfluidic chip[4], where the flow rate of both phases can be accurately controlled to generate a regular and stable stream of $2 - 5$ Hz throughput monodispersed droplets. If the microfluidic chip is placed inside a system of magnetic coils and the flow of microdroplets is diverted through a laser beam, the sample confined within each microdroplet is excited, emitting fluorescence. Finally, MFEs can be analysed by measuring the collected fluorescence emission intensity using a PMT or a spectrograph, which permits the characterisation of the emission spectrum and is used to identify the system of study.

The PMT measures the total emission resulting from the fluorescence of each microdroplet. A typical PMT response resulting from a single microdroplet passing through the laser beam is provided in **Figure 3.8b**, which can be divided into three main parts based on their flow and illumination times:

- $0 - 50$ ms: microdroplet and the beam spot of surface areas begin to overlap and an initial illumination takes place. However, only one rear edge is illuminated

[4]The exact microfluidic chip used is shown in **Figure 3.4**, along with the photos of its flow-focusing junction and microdroplet formation in **Figure 3.6**.

and, as the droplet moves further down the microchannel, the fluorescence signal grows in continuously;

- 50 – 150 ms: the beam spot is fully covered inside the microdroplet (as shown in **Figure 3.8a**) and the emitted fluorescence is maximised;
- 150 – 200 ms: microdroplet starts exiting the laser beam spot surface area and the signal starts to continuously decrease.

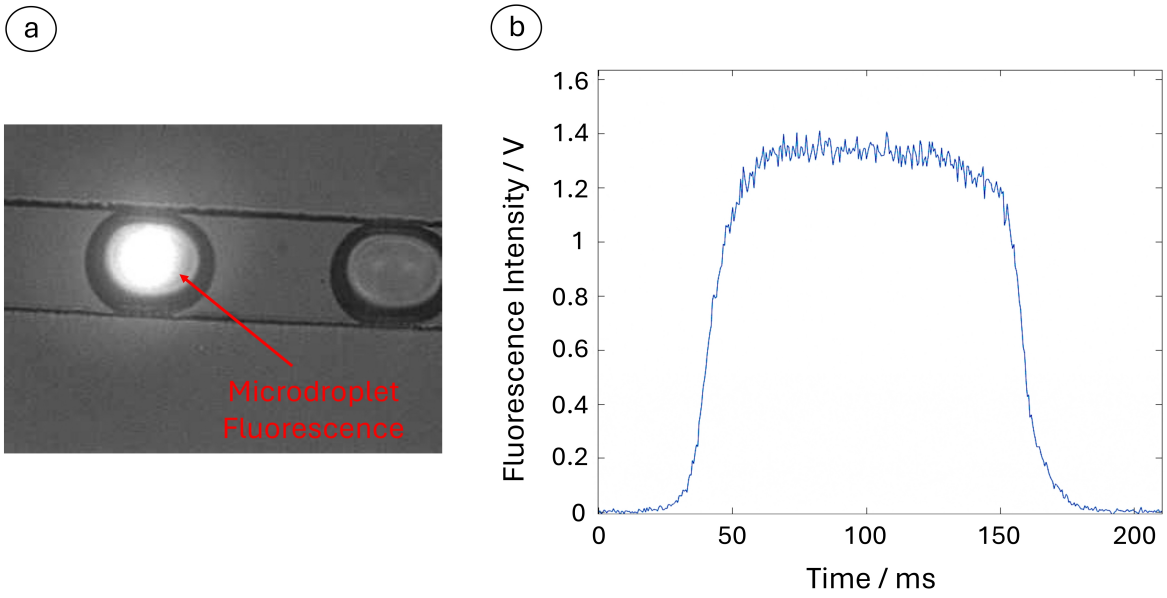


Figure 3.8 (a) Capture of fluorescence emission initiated as a photoreactive sample (FAD in citric buffer), encapsulated inside a microdroplet, flows through a laser beam of 2830 μm^2 size inside a microfluidic microchannel of 80 μm. (b) Variation in fluorescence signal measured with a PMT for a single microdroplet of FMN with ascrobic acid ($AscH_2$).

3.5.1 Experimental Apparatus and Data Acquisition Process

Microdroplets are formed upon the application of a pressure difference using a piezoelectric pressure controller (Elveflow OB1) across a microchannel of a microfluidic chip (Microfluidic ChipShop, Fluidic 440). The chip itself is placed on a 3D printed circular base plate[5] with an engraved chip holder installed on a holder arm (Thorlabs, MPRC, shown in **Figure 3.9**) which mounts on a 2-dimensional translation stage, allowing the precise focus of a custom-made inverted confocal microscope onto the microfluidic chip. The excitation beam of 2830 μm^2 size from a continuous-wave 450 nm diode laser (Oxxius LBX-450-70) is directed toward the microchannel using a

[5]All 3D prints were made by the University of Oxford Physical and Theoretical Chemistry Electronic and Mechanical Workshops.

long-pass 500 nm dichroic mirror that partially reflects and partially transmits light depending on its wavelength. It then travels through an oil immersion objective lens (Leica HC PL APO 40×/1,30 OIL CS2) that concentrates the beam onto channels of 80-15 μm diameter. The photoreactive system, encapsulated inside microdroplets that passes through the laser beam, is excited and emits fluorescence as a result. This time, the passing fluorescence signal through the dichroic mirror is not reflected but rather transmitted and refocused through a pinhole, which removes any reflected excited light from outside the focal plane, onto an optical fiber. The signal is directed to a spectrograph (Avantes AvaSpec-ULS2048x64TEC) or a PMT (Hamamatsu R928) for signal amplification. The PMT is linked to an oscilloscope (LeCroy HDO8058) for visualising variations in fluorescence intensity. The schematic outline of the experimental setup is presented in **Figure 3.10**.

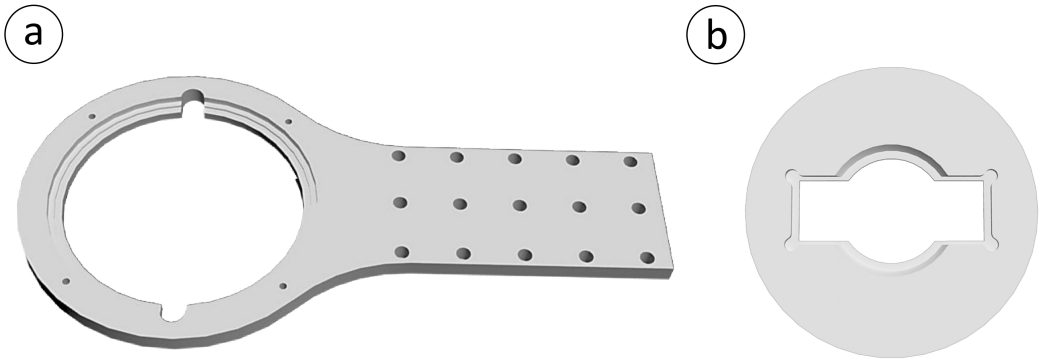


Figure 3.9 Digital CAD drawings of 3D models of the sample holder of (a) the holder arm and (b) the circular base plate with an engraved microfluidic chip holder. The holder arm is made of stainless steel which mounts on a manual rigid 2D translation stage. The circular holder is inserted into the 11 cm wide opening of the holder arm, allowing the objective (positioned below the holder arm) to be focused onto the microfluidic chip which is securely placed in the carved rectangular section of the base plate. The blueprints were generated using *Autodesk* software in collaboration with Dr. Patrick Murton.

The flow-focusing microfluidic chips (shown in **Figure 3.4**) are made of hydrophobic cyclic olefin copolymer (COC), which produces aqueous microdroplets submerged in the silicone oil carrier phase. The sample is introduced into the microfluidic chip by applying air pressure to the external sample containers that are connected through tubing to the pressure regulator and the inlets of the chip. The pressure forces the sample toward the inlet of the chip, essentially establishing a regular flow of both phases through the control of specific pressure levels applied to each phase until a de-

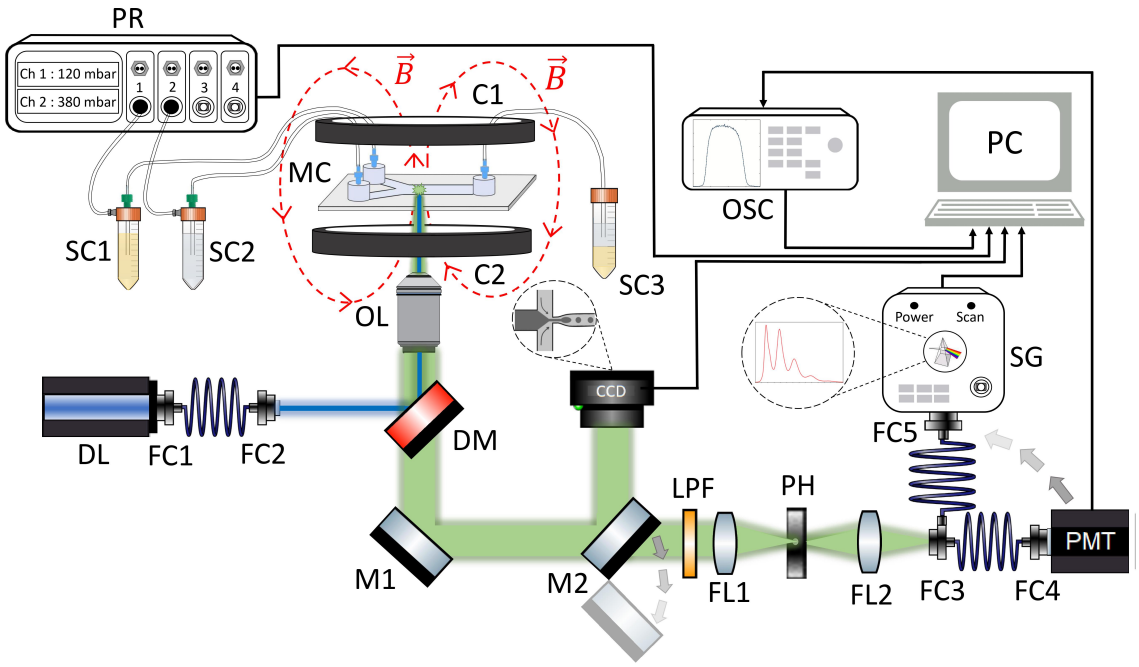


Figure 3.10 Schematic outline of the custom built experimental setup. Different components in alphabetic order: C1 and C2 are magnetic coils; CCD is the charge-coupled device camera; DL is the diode laser; DM is the dichroic mirror; FC1-5 are fiber collimators; FL1 and FL2 are focussing lens; MC is the flow-focusing microfluidic chip[a]; M1 and M2 are mirrors, with M2 having the possibility to be taken out to allow the beam to propagate into the PMT which is the photomultiplier tube; PH is the pinhole; PR is the pressure regulator; OL is the objective lens; OSC is the oscilloscope; PC is the personal computer; SC1-3 are sample containers; SG is the spectrograph.

[a]The flow-focusing microfluidic chip (among other experimental components) in **Figure 3.10** is not to scale; it appears larger than it actually is for more accurate representation of the main components of the chip.

sired microdroplet generation frequency is achieved.

After achieving a stable microdroplet flow through pressure applications to both the dispersed and carrier phases, MFEs can be investigated. This requires the application of magnetic fields using a set of Helmholtz coils[6] of 15 cm diameter that are placed around the microfluidic chip, equally spread 7.5 cm apart from one another. Its power supply provides a constant current to a set level of 7 A, which can generate homogeneous magnetic fields of around $\pm$ 31.5 mT. This can cause the coils to overheat, so regular circulation of a water-driven cooling system allows prolonged use of these magnetic coils.

[6]These custom-made coils were fabricated by the University of Oxford Physical and Theoretical Chemistry Electronic and Mechanical Workshops.

Fluorescence MFE experiments are first prepared by establishing a uniform and stable production of microdroplets at the flow-focusing junction. This is done by using the CCD camera, to which the emission signal can be redirected by adding a supplementary mirror (named as M2 in **Figure 3.10**). This allows to monitor microdroplet production in real-time and adjust the pressure applied to each phase accordingly, as well as focus the objective lens correctly to the microchannel in order to maximise the fluorescence emission signal. Once a preferred microdroplet production rate is achieved, the laser beam is then focused in the middle of the microdroplet flow, where a photochemical reaction is thus initiated (as shown in **Figure 3.8a**). This marks the end of the focusing procedure, and once the additional mirror diverting light to the CCD camera is taken out of the experimental setup, the fluorescence emission is delivered into the fiber coupling connected either to the spectrograph or the PMT. The spectrograph allows the recording of an emission spectrum of the species encapsulated within the microsystem and spectroscopic characterisation of the system, while the PMT measures the variations in fluorescence emission throughout the whole flow of each microdroplet (an example of the acquired PMT signal is shown in **Figure 3.8b**).

The acquisition of data is automated and handled by using a *LabView* software package[7] which allows the input of specific experimental parameters tailored to each MFE experiment, such as applied laser power, magnetic field strength, acquisition time of each measurement, number of acquired averages, etc. Each measurement consists of acquiring two time traces — one with an applied magnetic field and one without it — for each laser power and magnetic field strength. This protocol is then repeated for a chosen number of averages over a set period of time.

3.5.2 Data Analysis

The analysis of raw data acquired from the oscilloscope is performed using a written *MatLab* program[7] which separates each signal acquired from multiple microdroplets from a time trace into traces with and without an applied magnetic field. Each signal

[7]The custom written *LabView* and *MatLab* codes were developed by Dr. Patrick Murton.

is then centred and, if any anomalies happen[8], some peaks are removed. Then, all microdroplets from a specific applied magnetic field-strength are averaged into a single characteristic droplet signal.

Looking at the typical PMT signal of fluorescence (see **Figure 3.8b**), it is possible to model the characteristic microdroplet fluorescence shape as a difference in positive and negative sigmoid functions (as shown in **Figure 3.11**):

$$F_t(V) = A\left(\frac{1}{1+e^{-k_1(t-b_1)}} - \frac{1}{1+e^{-k_2(t-b_2)}}\right), \tag{3.35}$$

where A is the amplitude of the signal, k_1 and k_2 define the increase or decrease of the microdroplet signal, and b_1 and b_2 determine the width of the microdroplet. Therefore, to analyse a full time trace of N microdroplets, **Equation 3.35** can be rewritten as a series of differences in sigmoid functions:

$$F_t(V) = \sum_{i}^{N} A_i\left(\frac{1}{1+e^{-k_{i1}(t-b_{i1})}} - \frac{1}{1+e^{-k_{i2}(t-b_{i2})}}\right), \tag{3.36}$$

where $i, N \in \mathbb{N}$.

Since **Equation 3.36** has far too many individual variables to be fit as a function to thousands of individual microdroplets, it is easier and faster to fit **Equation 3.35** to each microdroplet and extract individual peaks. This is executed by determining the beginnings and ends of each microdroplet signal, which mathematically translates to calculations of the second derivative of raw data that describe how the slope of the approximated sigmoid function changes over time. Numerically, this can be determined by convoluting the normalised raw data with the analytical second derivative of a Gaussian:

[8]This might take place if only half of the microdroplet was recorded at the end of the trace or if it is significantly smaller than the other ones, suggesting that there might have been an issue with the formation of the microdroplet or a problem with the flow. In this case, the signal from such a microdroplet is not taken into the calculation of the averages required for %MFEs.

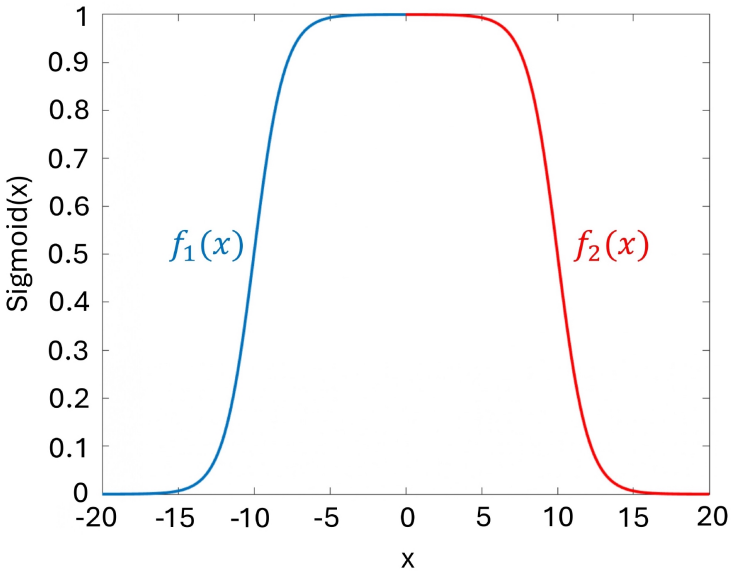


Figure 3.11 Example of positive and negative sigmoid functions, centred at $x = 0$. The characteristic fluorescence shape resulting from photoilluminating a microdroplet can be written as $F(x)$, as written above.

$$\frac{d^2F_t(V,t)}{dt^2} \approx \int_{-\infty}^{\infty} F_t(V,\tau)G''(t-\tau)d\tau = \mathcal{F}^{-1}\left(\mathcal{F}\left[F_t(V,t)\right] \cdot \mathcal{F}\left[G''(t)\right]\right), \tag{3.37}$$

where $F_t(V,t)$ is the raw fluorescence trace from each individual microdroplet, $\mathcal{F}$ and $\mathcal{F}^{-1}$ are the forward and inverse Fourier transform, respectively, and G'' is the second derivative of a Gaussian function, defined by:

$$G''(t) = \frac{1}{\sqrt{2\pi}\sigma^5}\left(\left(t - \frac{t_{aq}}{2}\right) - \sigma^2\right) exp\left(-\frac{\left(t - \frac{t_{aq}}{2}\right)^2}{2\sigma^2}\right), \tag{3.38}$$

where σ is the standard deviation parameter that defines the width of the Gaussian curve and, hence, the microdroplet size, and t_{aq} is the acquisition time.

These calculations lead to numeric solutions of positive maxima that determine the increase in microdroplet fluorescence and the decrease in signal. By calculating the gradient of the raw data at these points, each positive maximum is characterised either as the start or end of the microdroplet signal. The points are then paired accordingly and used to break down the raw data into individual microdroplet signals.

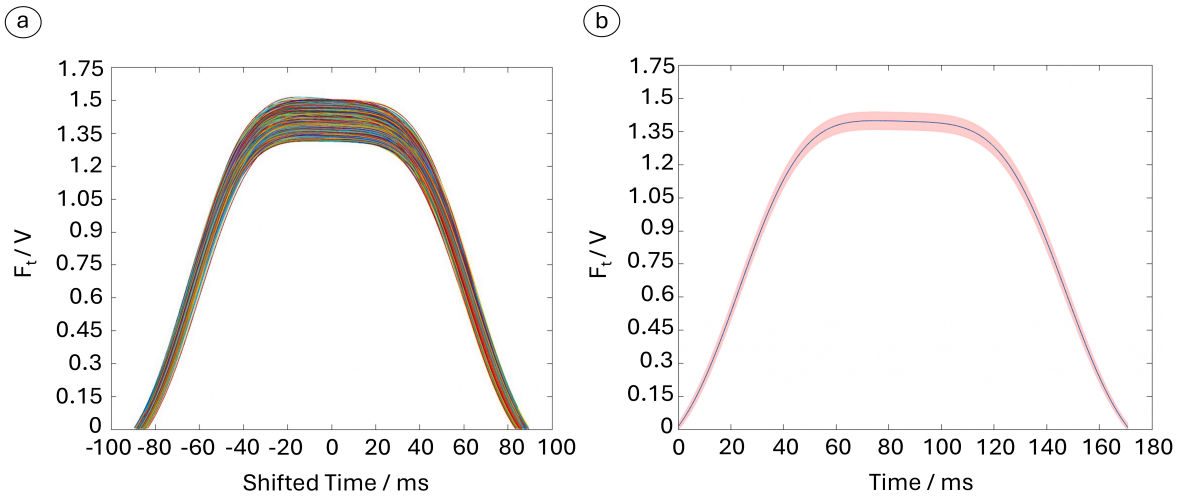


Figure 3.12 (a) All individual microdroplet signals from 1,000 averages for a single magnetic field strength superimposed on top of each other based on their flow time (centred at its half-time point relative to the entire microdroplet flow duration through the laser beam). (b) Averaged microdroplet signal from a series of acquired signals for a single magnetic field strength with error bars indicating standard deviation.

Once all signals have been extracted, their variations in fluorescence intensity are averaged for each magnetic field. Finally, further to **Equation 2.34**, the averaged microdroplet fluorescence traces are evaluated to calculate the %MFEs in the following way:

$$\%MFE = \frac{F_t(V)_B - F_t(V)_{B=0}}{F_t(V)_{B=0}} \cdot 100. \tag{3.39}$$

3.6 Summary and Outlook

The call for new experimental methods which significantly reduce the amount of sample required for optical measurements — particularly when it comes to working with sparse samples, such as Cry flavoproteins — have prompted the development of the new microdroplet fluorescence experimental technique. **Chapter 3** presented the necessary foundations of fluid mechanics to understand the mechanism of photoreactive sample encapsulation within microdroplets, together with the outline of the experimental setup needed for such measurements. In addition, practical development of the data analysis procedure explains how MFEs, resulting from each illuminated microdroplet, can be investigated.

In **Chapter 3**, **Equation 3.39** explains how %MFEs are calculated, which is at the center of **Chapter 4**, where the experimental results are presented. **Chapter 4** incorporates the key principles of fluid mechanics of relevance to microflows, the experimental application of the microdroplet fluorescence experiment, both of which were highlighted in **Chapter 3**, and the concepts of spin chemistry from **Chapter 2** on three model systems of relevance to Cry4a flavoproteins presented in **Chapter 1**.

Chapter 4

Magnetic Field Effects in Flavin Model Systems

When developing a new experimental technique, it is indispensable to start working with simplified and well-characterised systems. Successful results provide consistency and reproducibility across experiments, which is essential for validating the new technique. In terms of the microdroplet fluorescence experiment, it is important to first test out model systems containing photoactive components of Crys to minimise the variables and complexities encountered in intricate Cry proteins. This allows to shift the focus on refining the flow of microdroplets and their consequent analysis without the complications from any factors that spectroscopic screening of Cry proteins might entail, such as sample instability or aggregation. Finally, model systems are paramount for extensive testing and optimising of the novel technique without the incurring costs associated with difficult, expensive and time-consuming Cry purification and expression processes.

By way of proof of principle, the experimental results presented in this chapter are based on the spectroscopic characterisation of three Cry flavoprotein model systems:

1. FAD in citric buffer (pH 2.3) to unravel the relation between continuous fluorescence MFEs and laser induced sample degradation[1];

2. FMN with ascorbic acid (pH 3 and pH 7) to demonstrate the sensitivity of the experimental technique and manifestation of low field effects[1] (LFEs);

3. RF with Trp (pH 7) to monitor the influence that the microdroplet size reduction has on MFEs[1,2].

[1]Experiments on FAD, FMN, and some experiments on RF model systems were carried out in collaboration with Dr. Patrick Murton.

[2]Most experiments on RF−Trp model system were conducted together with Dr. Lewis Antill.

4.1 Flavin Adenine Dinucleotide in Citric Acid

Recalling from **Section 1.4.1**, FAD functions as the light-sensitive component in Cry flavoproteins, and is believed to be a key factor in migratory birds' ability to detect magnetic fields. The spin chemistry and MFEs related to the RPM of FAD in aqueous solutions are well understood and extensively documented in the scientific literature [162–165]. This makes it an excellent model system for validating novel experimental approaches aimed at observing MFEs resulting from RPs.

4.1.1 Photochemistry of F−AH_2^+ Radical Pairs

Following blue light photoexcitation of the ground state flavins F_{OX}, the excited singlet state $^1F^*$ undergoes ISC to form an excited triplet state $^3F^*$ before ET from the adenine (AH) moiety to the isoalloxazine ring (see **Figures 1.5** and **1.6**) takes place [165, 166]. Because the isoalloxazine ring and AH originate from the same compound, this is an *intramolecular* reaction mechanism[3] (shown in **Figure 4.1b**), and, due to spin conservation, the excited triplet state $^3F^*$ yields triplet-born SCRPs [165]. It can then interconvert with the singlet RP $^1[FH^{\bullet-} - AH^{\bullet+}]$ and eventually return to the ground state F_{OX} *via* BET or transition back to the excited triplet RP state $^3[FH^{\bullet-} - AH^{\bullet+}]$.

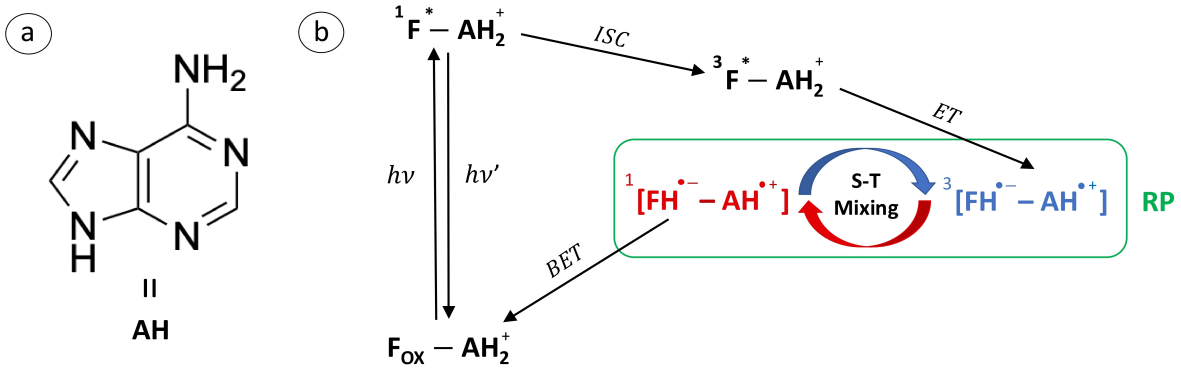


Figure 4.1 (a) Chemical structure of adenine (AH). It contains a six-membered pyrimidine ring along with an amino group attached to the C6 position of the ring, and a five-membered imidazole ring. (b) Proposed RPM photocycle for intramolecular MFEs in FAD under acidic conditions [162, 165]. F refers to the isoalloxazine moiety of FAD and AH_2^+ represents a deprotonated form of adenine. $h\nu$ depicts illumination at 450 nm and $h\nu'$ the emitted fluorescence as the excited $^1F^*$ returns back to the ground state F_{OX}.

[3] It is important to note that citric acid does not take an active role in this mechanism but is simply there to provide acidic conditions. At low pH (<3.6), the adenine group of FAD is protonated (F−AH_2^+), whereas a neutral molecule (F−AH) is produced at higher pH levels [162] due to isoalloxazine-adenine ring-stacking conformation [167], resulting in fast ET in the photoexcited state.

Magnetic fields stronger than FAD hyperfine couplings reduce the interconversion between the triplet and singlet states due to the energetic isolation of $|T_{\pm}\rangle$ states caused by the Zeeman interaction (see **Figure 2.3b**). This impedes singlet RP recombination within the RP and, assuming continuous illumination conditions, lowers the ground state F_{OX} concentration, resulting in negative MFEs observed as a reduction in ground state fluorescence intensity [168].

4.1.2 Description of the Experimental Conditions

Experimental data were collected from microdroplets produced in flow-focusing microfluidic chips with 80 μm channels. The aqueous solution of 30 μM FAD in pH 2.3 citric buffer (4 mM Na_2HPO_4, 98 mM citric acid in deionised water) was encapsulated in microdroplets with a high viscosity, immiscible silicone oil carrier phase. Each microdroplet was roughly 400 pL in volume and was tested with an illumination time of 120 ms using pressure levels of 150 mbar and 130 mbar for the carrier and dispersed phases, respectively. Excitation of the photoactive system was carried out at 450 nm continuous illumination, followed by measurements of MFEs across multiple laser powers and magnetic field strengths.

4.1.3 F$-$AH$_2^+$ Fluorescence Emission

The successful detection of the fluorescence signal from a series of microdroplets is indicated by the emission spectra in **Figure 4.2a**. The broad emission band peaks at 530 nm, corresponding to the $S_1 \rightarrow S_0$ transition that is consistent with the known FAD emission spectrum [162]. The small spike at $\sim$ 450 nm is a reflection from the excitation beam, and the spike at $\sim$ 730 nm is a back-reflection from the objective lens. Regardless, this confirms that the microdroplet fluorescence experimental method is capable of characterising the sample contained in each microdroplet using the spectrograph as the photodetector. Furthermore, the observed fluorescence increase during 500 ms to 1 s exposure times reflects the integrated signal from $2-3$ and $4-6$ microdroplets, respectively. This shows that fluorescence is a direct result of microdroplets passing through a laser, as the detected emission intensity proportionally correlates to the exposure time.

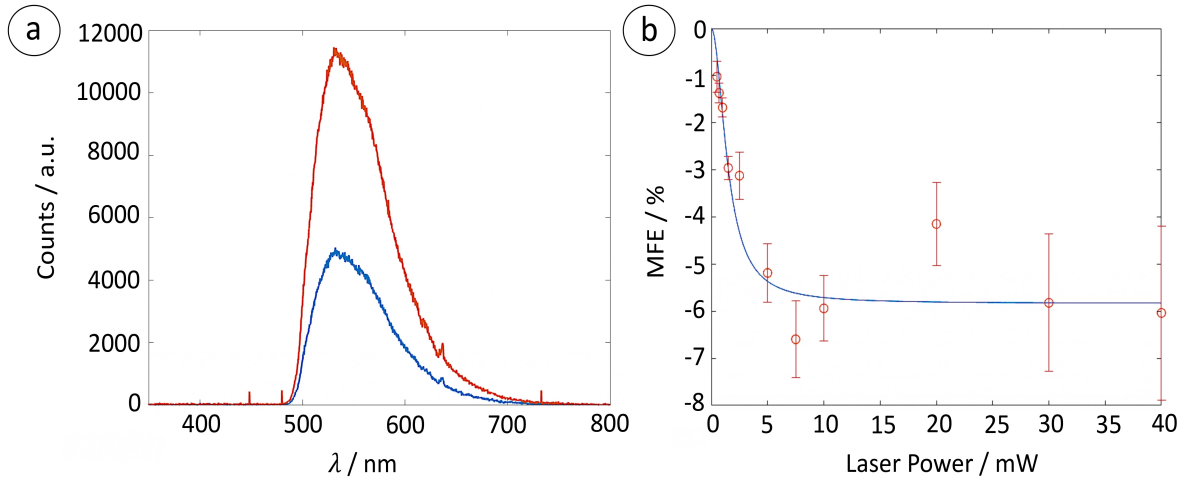


Figure 4.2 (a) Emission spectrum from microdroplets consisting of FAD excited at 450 nm. The blue line represents an average of 2-3 microdroplets, whereas the orange line depicts fluorescence emission from 4-6 microdroplets. The integration times are 500 ms and 1 s, respectively. (b) MFE power dependent experimental data from microdroplets consisting of FAD with a 30 mT applied magnetic field. The fit line in blue is a Lorentzian.

4.1.4 Power Dependence Measurements

Power dependence measurements are crucial in determining the required minimum laser power to achieve maximum excitation without causing significant photobleaching of the protein sample. By varying the laser power, it is possible to determine how the emitted fluorescence intensity and spectral characteristics of the system change, providing optimal conditions for measurements. **Figure 4.2b** shows the MFE as a function of excitation power, with the magnitude of MFEs increasing as laser power rises. This correlates with a greater excitation of the ground state F_{OX}, producing larger quantities of the photoinduced state $^1F^*$ and emitting more fluorescence which results in a stronger signal. Greater populations of $^1F^*$ lead to larger amounts of $^3F^*$ being produced *via* ISC, ultimately generating more triplet-born SCRPs. The increase of this magnetically sensitive species leads to the observed increase in MFE. The maximum MFE of -6% at 30 mT in this system starts to saturate at 5 mW, indicating no further increase in MFE at higher laser power levels.

4.1.5 MARY Results and Discussion

Consequently, the power level of 5 mW was chosen for recording the microdroplet fluorescence with and without an applied magnetic field. **Figure 4.3a** displays the averaged PMT response to FAD microdroplets under acidic conditions and shows a

clear decrease in fluorescence intensity under an applied magnetic field, exhibiting a total -7.2% MFE.

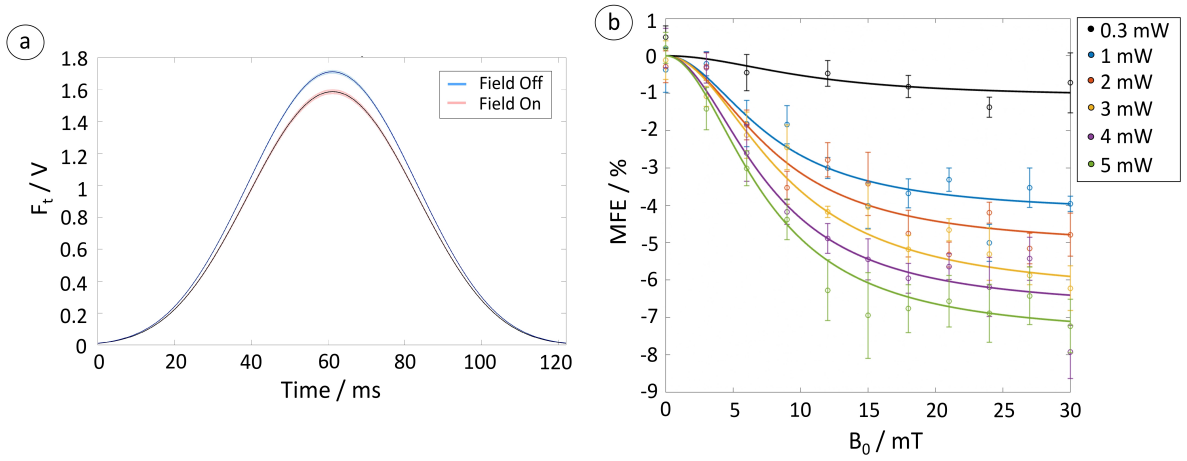


Figure 4.3 (a) Averaged microdroplet PMT signals from 10 averages with a 30 mT magnetic field (pink) and without any applied field (blue). The error bars were used as standard deviation. (b) MARY plots at different powers acquired from microdroplets of FAD. The different lines for each dataset represent Lorentzian fits.

Evaluating MFEs over a range of 0 mT to 30 mT magnetic field strengths at different excitation powers on FAD revealed a Lorentzian distribution of %MFEs that matches the characteristic MARY shape, shown in **Figure 4.3b**. The saturation level matches the values in the power dependence plot presented in **Figure 4.2b**: %MFE rises until 5 mW and achieves a plateau. These experimental MARY results are summarised in **Table 4.1**. It is worth mentioning that the $B_{1/2}$ values for each of these experiments do not indicate any noticeable trend. This is not surprising — increasing the applied power modifies only the relative population of excited molecules in the RPM photoscheme without affecting any of the spin dynamics, such as the hyperfine couplings or spin relaxation. However, theoretical calculations using the Weller formula (see **Equa-**

Power / mW	$\%MFE_{Sat}$	$B_{1/2}$ / mT
0.3	-1.0 ± 0.4	5.8 ± 1.2
1	-4.0 ± 0.5	7.9 ± 1.0
2	-4.8 ± 0.5	8.4 ± 0.8
3	-5.6 ± 0.5	8.5 ± 0.5
4	-6.4 ± 0.5	7.3 ± 0.6
5	-7.2 ± 0.7	6.5 ± 0.5

Table 4.1 Summary of the MARY experimental results using increasing excitation powers on the $F-AH_2^+$ model system.

tion 2.35) predict an estimated $B_{1/2}$ value of 2.6 mT for a flavin-adenine RP [162], although the average $B_{1/2}$ value[4] extracted from the measurements made above is 7.5 $\pm$ 0.3 mT. This can be explained by the equilibrium between the protonated FAD triplet state and the triplet-born radical pair ($^3F^*{-}AH_2^+ \rightleftharpoons {}^3[F^{\bullet-} - AH_2^{\bullet+}]$, see **Figure 4.1b**) induced by the application of magnetic fields which prolongs the lifetime of the RP [162, 165]. This increases electron spin relaxation, leading to a larger $B_{1/2}$ value, consistent with the values reported by Antill *et al.* [162].

4.2 Flavin Mononucleotide and Ascorbic Acid

To characterise how systems of intermolecular reactivity behave in microchannels, FMN and ascorbic acid ($AscH_2$) were chosen as the appropriate model system. Unlike FAD, FMN does not have an adenine moiety in its molecular structure (see **Figure 1.5**) which acts as an electron donor and participates in the ET. For that reason, an external electron donor is required. Studies by Kattnig *et al.* [12] and Evans *et al.* [113] reveal that $AscH_2$ exhibits magnetic sensitivity in the low field region by means of small hyperfine interactions in the ascorbyl radical, which results in additional routes for singlet-triplet interconversion than with zero-field being permitted when the applied magnetic fields are weaker than the system's hyperfine couplings (*e.g.* 12 mT). This is known as the LFE (see **Section 2.2.2**), which happens due to the lifting of degeneracies within some of the zero field eigenstates [136, 169] and manifests in positive values in the low field region [140, 170]. However, LFE is a very small effect, thus requiring extremely sensitive spectroscopic techniques to be observed in intermolecular systems. For these reasons, $AscH_2$ was chosen as the appropriate electron donor to evaluate the intermolecular RP formation with FMN in microchannels, and to test the sensitivity of the microdroplet fluorescence technique.

$AscH_2$ — widely referred to as vitamin C — is a water-soluble organic nutrient abundantly found in large amounts in fruits and vegetables [171]. In human bodies, $AscH_2$ helps to repair tissue damange, produce collagen and blood vessels, as well as heal

[4]This value was obtained by combining all experimental data into one data set. The weighted mean of all averaged $B_{1/2}$ values is 7.5 mT, with the errors leading to a smaller value of 0.3 mT in comparison with the results presented in **Table 4.1**, as the error varies with $\frac{1}{\sqrt{n}}$.

wounds and strengthen the immune system [172]. Key to its function in the intermolecular RPM, $AscH_2$ can act both as a reductant and antioxidant [171, 172] which, by donating electrons, reduces photoexcited flavins to form RPs. **Figure 4.4a** shows the chemical structure of $AscH_2$.

4.2.1 Photochemistry of FMN−$AscH_2$

Following absorption of a 450 nm photon, the excited singlet state $^1FMN^*$ undergoes rapid ISC to the excited triplet state $^3FMN^*$. Upon receiving an electron from $AscH_2$, a triplet-born SCRP $^3[FMNH^{\bullet-}\ AscH^{\bullet+}]$ is formed[5], which can interconvert to its singlet state and recombine back to the ground state FMN. As such, fluorescence emitted by the FMN−$AscH_2$ system displays negative HFEs and positive LFEs in the high and low field regimes, respectively [113] (typical MARY model profile shown in **Figure 2.7**). This intermolecular RPM photocycle is depicted in **Figure 4.4b**.

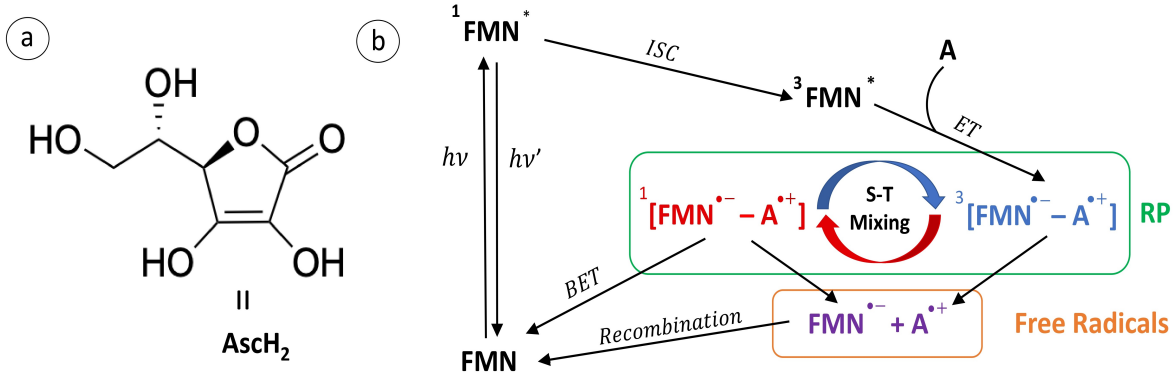


Figure 4.4 (a) Chemical structure of ascorbic acid ($AscH_2$). It contains four hydroxyl groups and one lactone ring, which is a cyclic ester. (b) Proposed RPM photocycle for intermolecular MFEs in FMN [113]. Species A refers to $AscH_2$. The protonation states of each species is not shown.

4.2.2 pH Dependence of FMN−$AscH_2$

At both pH 3 and pH 7, $Asc^{\bullet-}$ and $FMNH^{\bullet}$ are the thermodynamically favoured protonation states formed by ET [113]. However, at pH 7, $^3FMN^*$ is not protonated and forms a radical anion $FMN^{\bullet-}$. Therefore, the magnetic properties of the SCRP are determined by $FMN^{\bullet-}$ and $Asc^{\bullet-}$ at pH 7 [113].

[5] In sufficiently high concentrations of $AscH_2$, a singlet-born SCRP can be formed [173]. This process depends on the ET efficiency from $AscH_2$ and the relative concentrations of $AscH_2$ and FMN in the aqueous solution [113].

$FMN^{\bullet -}$ and $Asc^{\bullet -}$ are both negatively charged states, meaning that they are influenced by the repulsive Coulomb force, which is not the case for $Asc^{\bullet -}$ and $FMNH^{\bullet}$. At pH 3, there should be no Coulomb interaction between $Asc^{\bullet -}$ and $FMNH^{\bullet}$, so both species undergo free diffusion. However, it was reported that $Asc^{\bullet -}$ and $FMNH^{\bullet}$ form a complex at low pH, binding the two radicals together [113]. The dependence of the formed RP protonation states at pH 3 and pH 7 impacts MFEs, which is reflected in the observed MARY profile presented in **Section 4.2.5**.

4.2.3 Description of the Experimental Conditions

To investigate this system, an aqueous solution was prepared, consisting of 10 μM FMN, 2 mM $AscH_2$, formulated in a buffer adjusted with deionised water to pH 3 or 7 while maintaining an ionic strength of 0.1 M. The solution was tested on microdroplets of approximately 380 pL in volume together with silicone oil of high viscosity in a flow-focusing microfluidic chip under continuous illumination at 450 nm and 4 mW of applied laser power. The stable flow of microdroplets was formed by applying pressures of 140 mbar and 180 mbar to carrier and dispersed phases, respectively, resulting in an average illumination time of 141 ms.

4.2.4 FMN$-$$AscH_2$ Fluorescence Emission

Recording the emitted fluorescence from microdroplets containing FMN with $AscH_2$ results in minute differences between the fluorescence intensities with and without an applied magnetic field. The averaged PMT signal of microdroplets with FMN$-$$AscH_2$ is presented in **Figure 4.5**.

Initial results of FMN emission spectrum in microdroplets showed a spike in fluorescence from the COC polymer in the microfluidic chip at 513 nm (see **Figure 4.6a**). Curiously, this was not an issue for the F$-$$AH_2^{\ddagger}$ model system, as FAD exhibits higher fluorescence intensity than FMN (*cf.* **Figure 4.2a**) and overwhelms the fluorescence signal from COC. To address this issue, an implementation of a 550 nm long-pass filter was necessary to remove the emission resulting from the polymer. **Figure 4.6b** shows the fluorescence emission only resulting directly from the FMN$-$$AscH_2$ model system

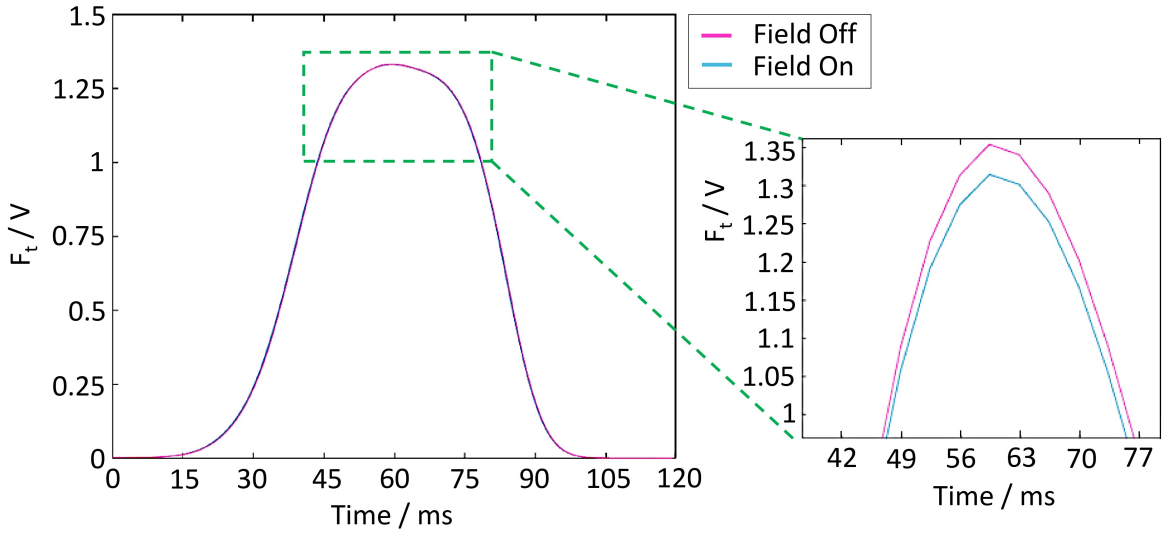


Figure 4.5 Averaged microdroplet PMT signals from 6,000 averages with a 30 mT magnetic field (blue line) and without any applied field (pink line). The error bars were used as standard deviation. The zoomed inset shows a clear difference in fluorescence emission when a magnetic field is applied.

after filtering, displaying an FMN emission spectrum above the filter cut-off. Thus, the shown emission peaks at 560 nm rather than at 530 nm (*cf.* **Figures 4.2** and **1.8**).

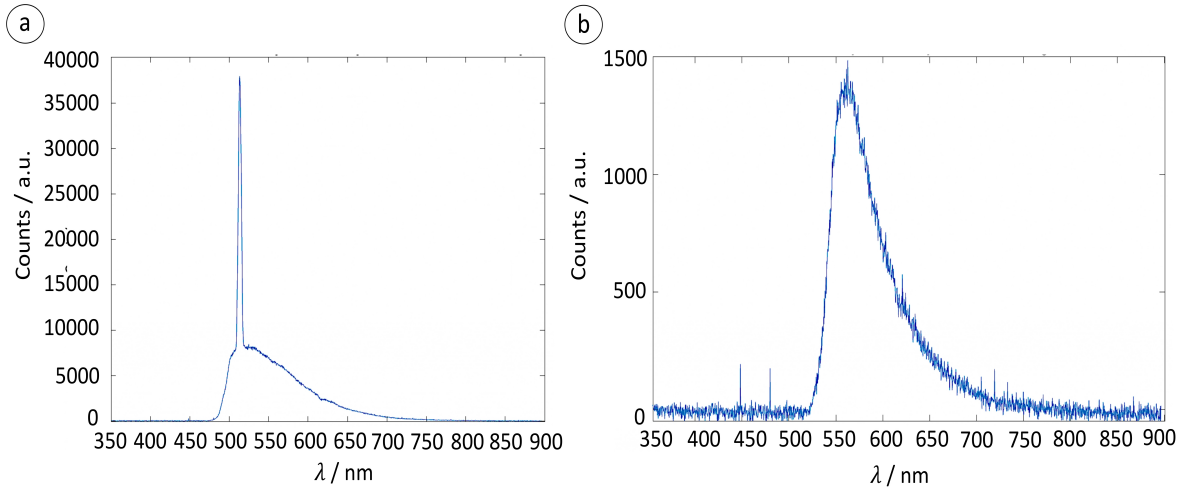


Figure 4.6 (a) Fluorescence spectra of FMN and $AscH_2$ with the emission of the microfluidic chip (spike at 513 nm). (b) FMN and $AscH_2$ fluorescence peaking at 560 nm with the microfluidic chip signal removed by a 550 nm long-pass filter. The integration time for both figures were 5 s, which resulted in more elevated counts than in **Figure 4.2a**.

4.2.5 MARY Results and Discussion

Figure 4.7 shows the recorded MARY at 4 mW which successfully captures both HFEs and LFEs. For pH 3 and 7, the LFE displays the amplitudes of $\sim$ 27.6% and $\sim$ 7.9%, respectively, of the magnitude of the HFEs, which is consistent with the previously

reported results [113]. The following sum of two Lorentzians was used to fit both MARY curves of different signs in high and low field regions, presented in **Figure 4.7**:

$$\mathcal{L} = \Lambda_1 \left(\frac{\zeta_1}{B^2 + \zeta_1} - 1 \right) - \Lambda_2 \left(\frac{\zeta_2}{B^2 + \zeta_2} - 1 \right), \tag{4.1}$$

where Λ_1 and Λ_2 measure the saturation of the HFE ($\%\text{MFE}_{\text{Sat}}$), ζ_1 defines the width of the MARY curve, and ζ_2 determines the depth of the LFE ($\%\text{MFE}_{\text{LFE}}$). The experimental results are summarised in **Table 4.2**, where B_{LFE} and B_{zero} are magnetic field values at the LFE peak maxima and when $\%$MFE is equal to zero, respectively.

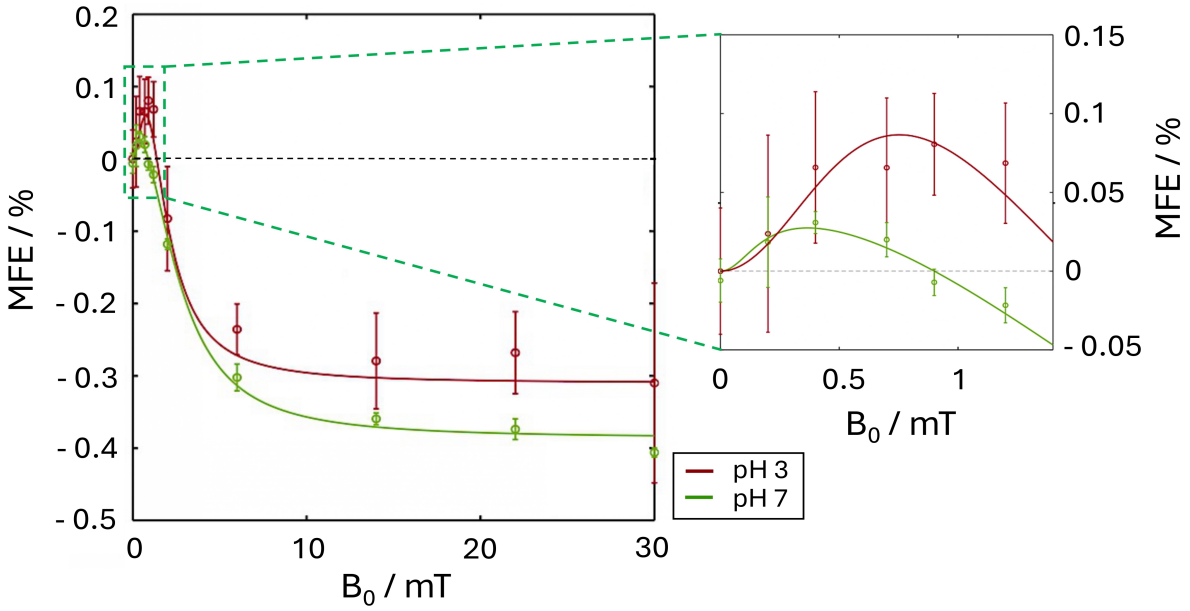


Figure 4.7 MARY plots on microdroplets containing FMN and AscH_2 at pH 3 and pH 7. The error bars were used as standard deviation. The zoomed insert shows successful capture of the LFE.

Experiment	$B_{1/2}$ / mT	$\%\text{MFE}_{\text{Sat}}$	$\%\text{MFE}_{\text{LFE}}$	B_{LFE} / mT	B_{zero} / mT
pH 3	2.71 ± 0.10	-0.29 ± 0.14	0.08 ± 0.03	0.90 ± 0.03	1.40 ± 0.05
pH 7	2.98 ± 0.04	-0.38 ± 0.01	0.03 ± 0.01	0.40 ± 0.01	0.90 ± 0.02

Table 4.2 Summary of FMN–AscH_2 model system MARY results.

The greater error for pH 3 measurements is a result of a lower number of averages collected throughout the experiment — data for pH 3 were acquired with 300 averages for each field point, whereas 2,000 averages were collected for pH 7. In addition, each average was acquired over a 2 s time period for the aqueous solution of pH 7,

which captured FMN fluorescence of 3 to 4 microdroplets per acquisition and, therefore, produced a total of 6,000 to 8,000 averages, respectively, for each field point (or between 66,000 and 88,000 microdroplets analysed in total). Nonetheless, the total sample volume consumed throughout this experiment was only *ca* 45 μL, which highlights the advantage of microfluidic technology when working with limited amounts of sample.

4.2.6 Test of Microdroplet Generation Reproducibility

The large amount of averages acquired during the MARY experiment for the FMN$-$AscH$_2$ model system provided reasonable levels of sampling to assess the reproducibility[6] of the microdroplet fluorescence experimental technique. If each illuminated microdroplet is considered to be a separate sample, then identical volumes of FMN$-$AscH$_2$ need to be encapsulated in each microdroplet in order to quantitatively compare the spectroscopic results from each microdroplet.

The flow-focusing microfluidic chips contain microchannels with rectangular cross-sections of fixed dimensions[7] of their height and width. Therefore, the only other dimension that influences the volume of each sample is the microdroplet length. Because the flow speed of microdroplets inside the microchannels is assumed to be constant (see **Appendix C.1**), it is possible to evaluate the volume of each microdroplet by looking at the total illumination time of the photoreactive sample upon flowing through the laser beam.

Figure 4.8 presents a histogram illustrating the different illumination times of all microdroplets acquired throughout the experiment with the duration of illumination for each microdroplet binned in ms timescale. Based on the symmetric bell-shape of the histogram, a normal distribution was assumed with a standard deviation of 3.83 ms. This accounts to 2.78 $\%$ in volume variability and, given the average recorded

[6]The analysis code and subsequent tests of reproducibility on the FMN$-$AscH$_2$ model system were developed in collaboration with a DPhil student Daniel Cubbin in the Mackenzie group.

[7]The width and height of the microfluidic chip may vary at the junction depending on the chip model. However, this is irrelevant since microdroplets flow in a straight channel with no variations in height of width once they are formed after passing the junction.

flow rate of 1.72 μL/min[8], the standard deviation in flow times reflects a very small fluctuation with almost no impact on the total volume during the short interval of 3.83 ms. Considering the approximate volume of 380 pL of microdroplets tested for FMN−$AscH_2$, this results in variations of $\sim$ 10.5 pL in volume in total between microdroplets, suggesting a high degree of reproducibility in the encapsulation of photoactive sample volumes within microdroplets.

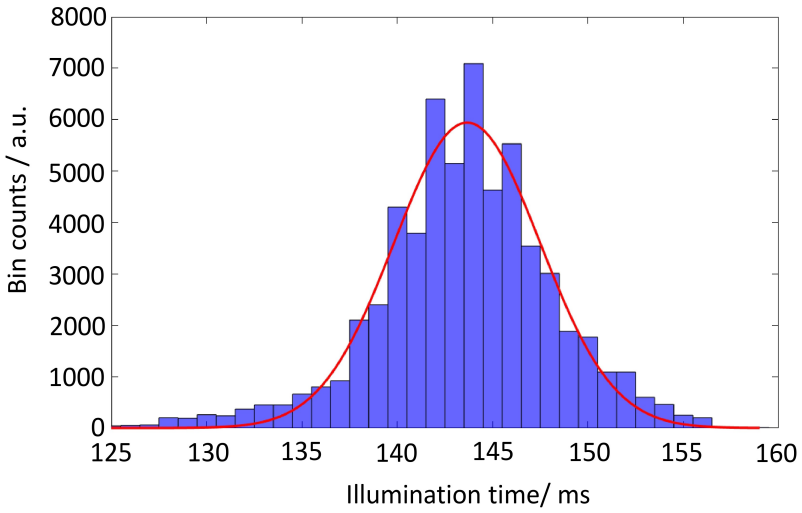


Figure 4.8 Histogram distribution of the different illumination times across all microdroplets acquired during a MARY experiment on FMN−$AscH_2$. The fitted Gaussian function is shown in red.

4.3 Riboflavin and Tryptophan

In comparison with bulk measurements, microdroplets entail analyses with significantly smaller volume of photoreactive samples, which may lead to increased sensitivity in detecting minute differences in kinetic rates of fast reactions. In terms of microfluidics, this is due to the flow of microdroplets in confined channels — the constant contact with microchannel walls (see the *no-slip* condition in **Section 3.3.1**) creates internal flows in the opposite direction to the microdroplet flow (explained in **Section 3.4.1**). Such experimental conditions induce the effect of internal circulation of molecules inside the microdroplet (see **Section 3.4.2**), which increases the rate of encounters between radicals [174] — a particularly important factor for short-lived intermediates involved in intermolecular RPMs.

[8]The average flow rate was measured using a microfluidic flow rate sensor (Elveflow, MFS 5) for the first 22 hours of the experiment.

Based on studies done by Yu *et al.* which show a dependence of internal mixing rates on the size and shape of the microdroplet [175], it is necessary to evaluate whether the microdroplet volume has any effect on MFEs. For this, an intermolecular RF−Trp flavin model system was chosen, as theoretical predictions [1, 15, 132, 139, 176] and spectroscopic measurements [6, 12, 173, 177–179] show that Trp — an essential amino acid that acts as a precursor to the neurotransmitter serotonin, the hormone melatonin, and vitamin B_3 [180] — is considered to make up the magnetically sensitive RP in Cry proteins. In addition, Trp participates in ET processes throughout the Trp tetrad in Crys (see **Figure 1.10**), therefore, making it one of the central components in the magnetic avian compass that birds use for navigation.

4.3.1 Photochemistry of RF−TrpH

Figure 4.9a shows the chemical structure of Trp, along with the intermolecular RPM scheme presented in **Figure 4.9b** that closely reassembles the FMN−$AscH_2$ model system (*cf.* **Figure 4.4b**). After the ground state RF absorbs a photon and forms the singlet excited state, $^1RF^*$, the SCRP is generated in the triplet state, $^3[RF^{\bullet-}\ TrpH^{\bullet+}]$. Upon the application of magnetic fields, the successive interconversion into the singlet state, $^1[RF^{\bullet-}\ TrpH^{\bullet+}]$, leads to negative MFEs in the ground state RF which can be analysed through fluorescence.

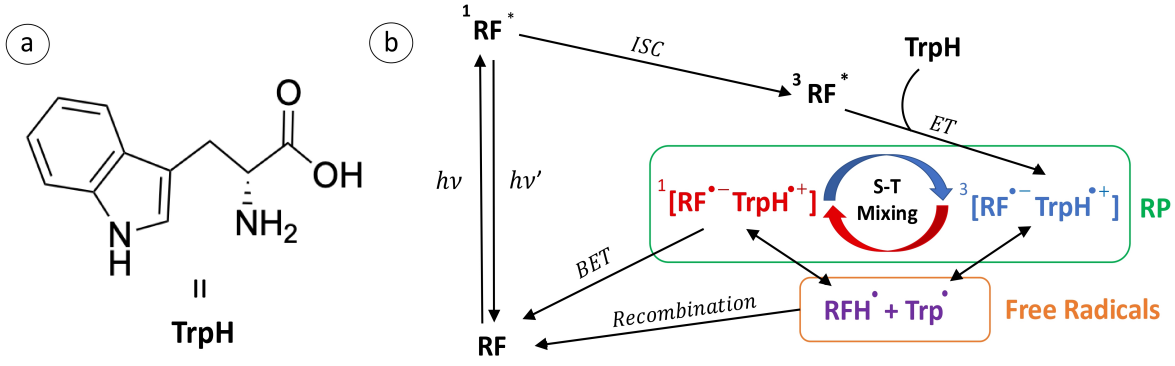


Figure 4.9 (a) Chemical structure of tryptophan (TrpH). It contains an α−carboxylic and α−amino groups, and a side chain indole. (b) Proposed RPM photocycle for intermolecular MFEs in RF and TrpH.

4.3.2 Description of the Experimental Conditions

To investigate how the microdroplet size affects the MFEs in bi-molecular RP systems, an aqueous solution of 10 μM RF and 500 μM Trp was prepared in deionised water.

The solution was tested on microdroplets with a high viscosity silicone oil in a flow-focusing microfluidic chip with different microchannel sizes ranging from 80 μm to 50 μm in diameter. The flow of microdroplets was continuously illuminated using a 450 nm laser. Microdroplets were produced at a 2−4 Hz frequency with average illumination times ranging from $\sim$ 170 ms to $\sim$ 140 ms. Experimental conditions for each separate measurement are presented in **Table 4.3**.

Size / μm	Volume / pL	Aqueous phase / mbar	Carrier phase / mbar	Time / ms
80 μm	390	180	300	172
70 μm	350	210	280	157
60 μm	315	160	330	145
50 μm	280	200	290	138

Table 4.3 Summary of experimental conditions for the RF−TrpH model system. Size refers to the microchannel diameter; volume defines the average microdroplet volume throughout the experiment; aqueous and carrier phases specify the pressures applied to each specific phase; and time describes the average illumination time for each microdroplet.

4.3.3 RF−TrpH Fluorescence Emission

Fluorescence emission was first recorded using a spectrograph which revealed a spike at 513 nm from the COC polymer in the microfluidic chip (shown in **Appendix C.2**), identical to the problem explained for the FMN−$AscH_2$ system (see **Section 4.2.4**). The application of a 550 nm long-pass filter removed the emission resulting from the polymer and reilluminating the same solution in microdroplets revealed a peak at 560 nm above the filter cut-off. Thus, the following measurements were performed with the 550 nm long-pass filter.

4.3.4 MARY Results and Discussion

Figure 4.10a shows a series of MARY measurements recorded at 2 mW laser power on different microchannels to examine how the MFE develops with microdroplet size. Interestingly, microchannel diameter reduction from 80 μm to 50 μm does not show any obvious increase in MFE magnitude or a trend in $B_{1/2}$ values. The mean variation of all 4 measurements conducted in different microchannels is 4.0 $\pm$ 0.2 mT and -0.93 ± 0.04 $\%$ for the $B_{1/2}$ and $\%\text{MFE}_{\text{Sat}}$ values, respectively (see **Footnote 4**). Moreover, the values of each of the 4 measurements fall within the error margins

of other measurements, suggesting there is no substantial difference in the observed experiments. These experimental results are summarised in **Table 4.4**.

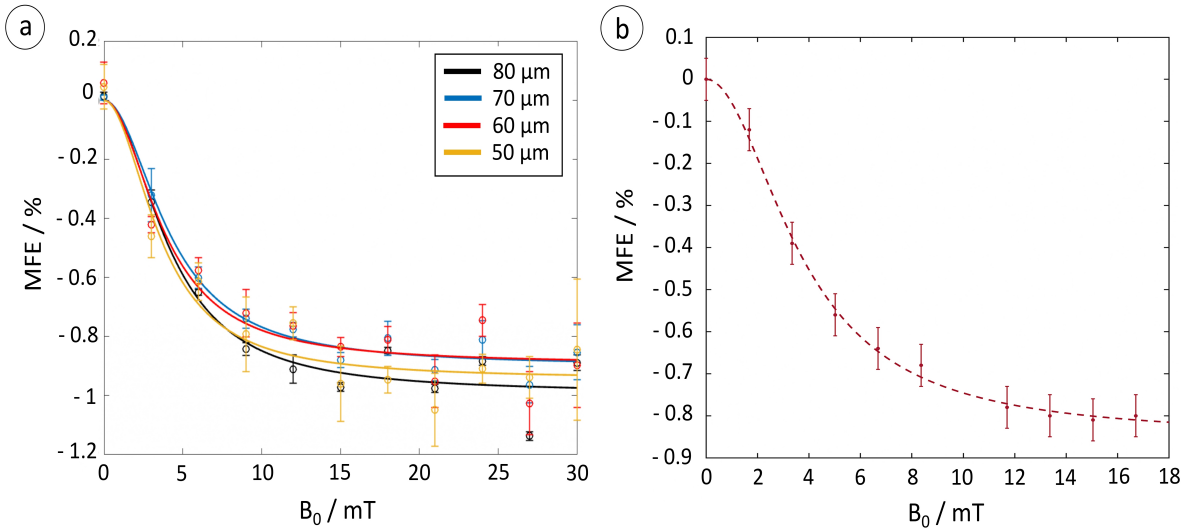


Figure 4.10 (a) MARY plots recorded at 2 mW power in microchannels of different diameter for 1,800 averages. (b) MARY plot measured on the confocal microscope in a bulk solution. Due to experimental limitations, the MARY could only be measured up to 18 mT on a bulk solution. The results demonstrate a good correlation between MARYs recorded in confined microchannels and in bulk. The error bars is both plots were used as standard deviation.

Experiment	$B_{1/2}$ / mT	$\%MFE_{Sat}$
Bulk	3.8 ± 0.6	-0.81 ± 0.06
80 μm	4.1 ± 0.4	-0.94 ± 0.08
70 μm	4.2 ± 0.3	-0.88 ± 0.09
60 μm	3.8 ± 0.5	-0.88 ± 0.08
50 μm	3.6 ± 0.4	-0.93 ± 0.12

Table 4.4 Summary of RF−TrpH model system microdroplet diffusion confinement experiment MARY results, along with the results of a measurement for a bulk solution.

When microdroplet size is reduced, the surface area to volume ratio increases, which theoretically should enhance reaction rates because of improved mixing dynamics inside the microdroplet caused by the constant movement of the flowing the samples inside the microfluidic chip. Nonetheless, the results acquired in 80−50 μm channels are comparable to the ones conducted on a bulk solution, which suggests that the RF−TrpH model system does not show any significant difference in spin dynamics

when the volume size is reduced to the microscale. This can be confirmed experimentally[9] by comparing the magnitudes of MFEs and $B_{1/2}$ with an experiment recorded on a confocal microscope where the solution was illuminated in bulk, the results of which are shown in **Figure 4.10b**. In bulk, the RF−TrpH model system exhibits 3.8 ± 0.6 mT and −0.81 ± 0.06 % for the $B_{1/2}$ and $\%\text{MFE}_{\text{Sat}}$ values, respectively (see **Table 4.4**). Despite the different physical environments, the experimental data indicate that the kinetic reaction rates and yields are comparable across both techniques. This suggests that the effect of reducing the sample volume to a few hundreds of pL does not introduce any substantial effect on the spin dynamics in the RF−TrpH model system. Nevertheless, these experimental results highlight the main advantage of microfluidic technology, which is to significantly reduce the sample volume required for experiments. The experiment in bulk required of ∼ 1 mL of sample, whereas all four experiments in microchannels of different sizes resulted in a total of 53.4 μL of sample volume used.

4.4 Summary and Outlook

The experimental results presented in **Chapter 4** constitute the successful development of the microdroplet fluorescence technique, showcasing great sensitivity in detecting minute differences in fluorescence intensities for both the intra- and intermolecular model systems of the RPM. Experimental findings on the F−AH_2^+ model system revealed that increasing the applied laser power to the photoreactive sample increases the fluorescence emitted by the singlet excited state $^1F^*$ and enhances the MFE by producing larger populations of SCRPs. The FMN−$AscH_2$ model system showed that the LFE and HFE depend on the pH of the system, and demonstrated the high sensitivity to detect MFEs down to 0.007 %. In addition, the reproducibility of microdroplet formation was tested on microdroplets containing FMN as the photoreactive sample. An average variation of 2.78 % in the encapsulated sample volume of each microdroplet was revealed, suggesting a high degree of reproducibility of the

[9]Experiments on the RF−TrpH model system in bulk solutions were recorded by a DPhil student Jamie Gravell in the Timmel group in collaboration with MChem student Will Parry from the Mackenzie group.

experiment. Finally, the RF−TrpH model system allowed to investigate the effect that the microdroplet size has on MFEs, which did not reveal any significant difference to the experiments produced in the bulk solution. This suggests that analyses conducted in microchannels can yield comparable results to bulk solutions, but with reduced volumes of the precious Cry sample, thus accentuating the advantages of microfluidics over conventional methods. The work in this chapter contributed to posters presented at two international conferences: "Lab-on-a-Chip and Microfluidics Asia 2023" and "18th Symposium on Magnetic Field and Spin Effects in Chemistry and Related Phenomena (Spin Chemistry Meeting 2024)"[10] (attached in **Appendix D** and **Appendix E**, respectively).

The experiments explained in **Chapter 4** allowed the development of the microdroplet fluorescence technique, particularly the fine tuning of the microdroplet formation and the different experimental parameters, such as laser power, difference in carrier and disperse phases' pressure, *etc*. All of this is of paramount importance for **Chapter 5** which examines the first-ever recorded fluorescence signal in microdroplets of *Gg*Cry4a avian protein.

[10]This poster was honored with the *Young Investigator Poster Award*, presented by the *Computational and Structural Biotechnology Journal*.

Chapter 5

Avian Cryptochrome Magnetosensitivity on Droplet-Based Microfluidics

In **Chapter 1**, the feasibility of avian magnetoreception was established, with behavioural and biological studies showing that Cry is likely to be the plausible magnetoreceptive molecule of the biological compass. **Chapter 2** discussed how magnetic fields affect RPs and their interconversion between the singlet and triplet spin states using the theory of the RPM. In addition, the postulated RPM photocycle was presented, explaining how photoinduced SCRPs generate MFEs in Crys. Based on the theoretical background of the microdroplet fluorescence experimental method described in **Chapter 3**, three flavin model systems were tested, each containing FAD, FMN or RF as the chromophore. Experimental results on microdroplets in **Chapter 4** indeed show that RPs respond to externally applied magnetic fields and display MFEs. However, due to the difficulty of expressing and purifying avian Cry proteins (Cry4a), as well as their instability and limited availability, there is a need for new methods that detect MFEs without damaging the sample and requiring excessive amounts of volumes. To address this challenge, the following **Chapter 5** presents the first reported fluorescence emission signals on domestic chicken mutant Cry (*Gg*Cry4a W369F) in microdroplets, along with the necessary development of the experimental setup needed to accommodate experiments on Cry4a proteins.

5.1 Point Mutations in Cryptochrome 4a

Naturally occurring Cry proteins inside the birds' retinae are termed *wild type*, and are expressed using the bird's natural amino acid sequence. Previous spectroscopic studies on wild type Cry proteins successfully reported MFEs, including plant thale cress

(*Arabidopsis thaliana, At*Cry1) [12, 181], fruit fly (*Drosophila melanogaster, Dm*Cry) [177, 182], European robin (*Erithacus rubecula, Er*Cry4a) [6, 177], domestic chicken (*Gallus gallus, Gg*Cry4a) [178] and pigeon (*Columba livia, Cl*Cry4a) [173].

However, to assess the role of each specific residue within the sequence and determine their impact on RP magnetic sensitivity, it is possible to prepare site-specific mutant Cry proteins by replacing native amino acid residues with a different amino acid. Various studies have already explored the magnetic sensitivity of Cry4a mutants [6, 173, 178, 183, 184]; particularly important are the recent studies by Xu *et al.* [6] and Gravell *et al.* [184] which show that the mutation, where the terminal Trp_D (W369, refer to **Figure 1.10**) was replaced with a redox-inactive phenylalanine (F), exhibits significantly larger MFEs. The reasons for the increased MFE remain under investigation, but a possible explanation could include the formation of photoinduced FAD$-Trp_C$ RPs that are longer lived. This allows longer mixing times of the singlet and triplet spin states, which is argued to primarily occur on the Trp_C residue [179, 184]. Therefore, it is advantageous to test a W369F mutant form of Cry proteins on microdroplet fluorescence technique, as studies by Gravell *et al.* show ~ 1.2 % MFE in *Gg*Cry4a W369F [184]. **Figure 5.1** shows the mutated structure of *Gg*Cry4a W369F.

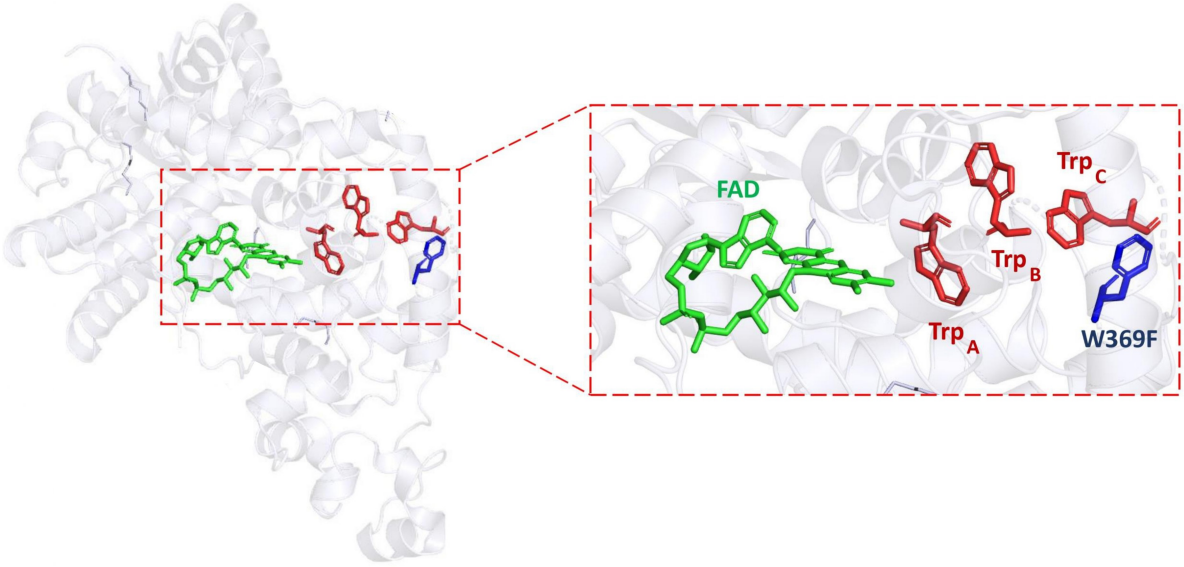


Figure 5.1 Homology model of the mutated chicken cryptochrome 4a protein (*Gg*Cry4a) W369F (drawn from PDP ID entry 6PTZ and mutated with the *PyMOL* software [121]). The zoomed inset depicts the *Gg*Cry4a W369F protein FAD cofactor (green), the three Trp residues (red), and a phenylalanine (blue).

5.2 Development of the Microdroplet Fluorescence Experimental Setup

In preparation to evaluate the magnetic sensitivity of Cry proteins in microdroplets, certain alterations to the experimental setup were required. The following section outlines the latest developments in the experimental apparatus.

5.2.1 Minimisation of the Tubing Length

Due to the limited availability of *Gg*Cry4a samples (generally, less than a few mL), it is necessary to reduce the length of the tubing connecting the sample container to the microfluidic chip through which the sample enters the microchannel (see the experimental setup outline in **Figure 3.10**). Longer tubing can result in a considerable portion of the Cry protein being confined within the tubing itself before it reaches the microfluidic chip. This poses the risk of introducing air bubbles into the tubing once all of the Cry protein is exhausted from the sample container, which is inevitable when dealing with limited amounts of Cry protein sample. As air has a much lower viscosity compared than silicone oil, it moves faster through the microchannel under the same pressure, which disrupts the generation of microdroplets and the reproducibility of encapsulation of Cry proteins. In addition, Cry samples should always be kept below 5 °C to avoid protein denaturation, which may not be possible due to prolonged confinement in microfluidic tubing at room temperature. This can lead to the denaturation of the photoreactive protein before it is illuminated, leading to spurious results, *e.g.*, MFEs recorded from free FAD or incorrectly bound FAD.

To minimise the risks explained above, a new base plate with three eppendorf vial holders was printed (see **Figure 5.2a**). Thus, minimising the distance between the sample holder and the microfluidic chip (*cf.* **Figure 3.9** for comparison with old components). This allows for a faster injection of Cry samples into the microfluidic chip, enhancing the reproducibility of microdroplet generation and the effective use of Cry protein samples.

5.2.2 Improving the Stability of Sample Stage Holder

The new base plate containing the microfluidic chip is placed inside the opening of the holder arm, which slides into the rigid microscope body and is tightly secured with a dovetail rail. Unlike the fixed end of the holder arm, the free end is unconstrained and susceptible to small movements due to vibrations that may arise while acquiring experimental data. This can result in the loss of focus to the microchannel and a decrease in the acquired fluorescence signal, which reduces the likelihood of detecting MFEs.

In order to keep the base plate more stable, a plastic circular clamp was printed (shown in **Figure 5.2b**) that positions on top of the main base plate. By tightening it with four screws that fit into the holder arm (see **Figure 3.9a**), the extent of the intermediate base plate movements are reduced, which provides more stability to the sample holder. The final sample holder CAD drawing with the new components added is presented in **Figure 5.2c**.

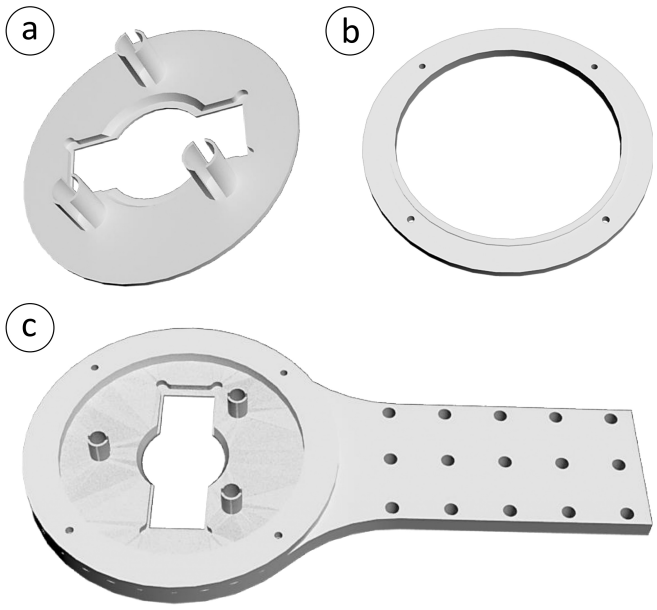


Figure 5.2 Digital CAD drawing of 3D models of the sample holder adopted for MFE analysis of Cry proteins. Figures were generated using *Autodesk* software in collaboration with Dr. Peter Watson. (a) A new circular base plate, featuring three eppendorf vial holders for the dispersed and carrier phases next to the microfluidic chip, as well as a holder for the waste vial. (b) A circular clamp positioned atop the main base plate where the microfluidic chip is inserted. It is fastened with screws into the holder arm to enhance the stability of the intermediate plate. (c) The holder arm with the news parts implemented.

5.3 Mutant Chicken Cryptochromes in Microdroplets

5.3.1 Photochemistry of *Gg*Cry4a W369F

The photoscheme of the FAD−TrpH RPM in *Gg*Cry4a W369F protein is shown in **Figure 5.3**. Identically to the RPMs presented in **Chapter 4**, the excited singlet state of $^1FAD^*$ is formed when FAD_{OX} absorbs a photon from blue light photoexcitation. Because all components of the RPM are confined within the protein, this is followed by rapid (<1 ps [185]), intramolecular ET from the isoalloxazine ring along a triad of Trp residues[1] [186], which out-competes ISC to the triplet state of $^3FAD^*$. This results in the formation of a singlet-born SCRP between an anionic semiquinone and tryptophanyl cation radical $^1[FAD^{\bullet-}\ TrpH^{\bullet+}]$, which can undergo hyperfine coupling driven interconversion to the triplet state $^3[FAD^{\bullet-}\ TrpH^{\bullet+}]$. Based on the rules of spin conservation, only the singlet RP can directly recombine back to the ground state FAD_{OX} *via* BET. In addition, both the singlet and triplet RPs can form long-lived neutral radical state $FADH^{\bullet}$ through deprotonation of $TrpH^{\bullet+}$ and protonation of $FAD^{\bullet-}$, which ultimately return back to the ground state.

5.3.2 Sample Preparation Protocol

To evaluate the magnetic sensitivity of Crys in microdroplets, samples of *Gg*Cry4a W369F protein were expressed and purified by collaborators in Professor Henrik Mouritsen's group at the University of Oldenburg, Germany, as described by Xu *et al.* [6]. Prior to shipping the samples to the University of Oxford, where they are stored in a $-80°C$ cryogenic freezer, the samples are suspended in 20 mM Tris buffer (pH 8, 260 mM NaCl, 20 % glycerol v/v) and BME[2] to reduce degradation during shippment. Before Cry proteins are injected into the microfluidic chip, the samples of *Gg*Cry4a W369F were centrifuged to washed out the reducing agent (BME) from

[1] Normally, *Gg*Cry4a consists of a tetrad of Trps, but the Cry of study — *Gg*Cry4a W369F — has only three Trp residues, as the fourth W_D has been mutated by an F amino acid (see **Figures 1.10** and **5.1**).

[2] BME — or $\beta-$mercaptoethanol — is used in proteins to prevent aggregation and improve their stability. Generally, BME is added during the purification process of the protein.

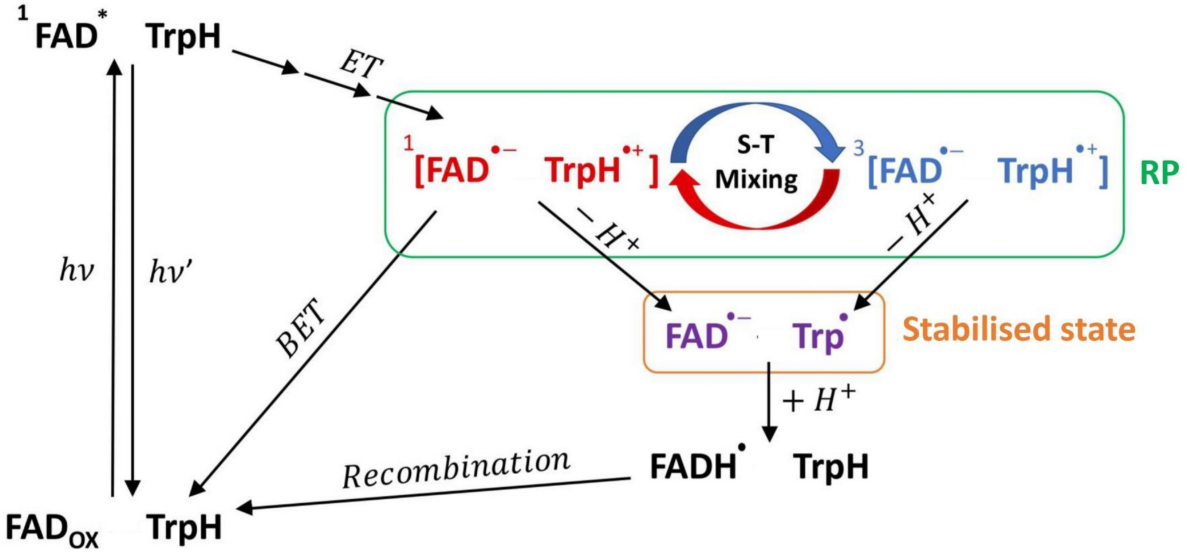


Figure 5.3 The RPM photocycle of FAD−TrpH in the *Gg*Cry4a W369F mutant protein [15, 139]. The singlet-born RP ^{1}[FAD$^{\bullet-}$ TrpH$^{\bullet+}$] is formed *via* an intramolecular ET from the excited singlet state ^{1}FAD* TrpH. It can recombine back to the ground state FAD$_{OX}$− TrpH or interconvert to the triplet state ^{3}[FAD$^{\bullet-}$ TrpH$^{\bullet+}$]. The SCRP can form a longer-lived neutral radical state FADH$^\bullet$ TrpH through deprotonation and protonation processes of both radical species.

the samples with a 20 mM Tris buffer solution and centrifugal filters. Finally, the concentration of the sample was measured using a UV-Vis spectrometer and subsequently diluted to an approximate protein concentration of $\sim 50\,\mu$M (*ca.* 0.6 OD at 450 nm).

5.3.3 Description of the Experimental Conditions

To keep the sample at a low temperature, an eppendorf vial containing the solution of *Gg*Cry4a W369F protein along with a sample container of silicone oil were submerged in an ice bath throughout the experiment. The solution was tested in microchannels of 80 μm in a flow-focusing microfluidic chip. The application of 90 mbar and 210 mbar pressures to the dispersed and carrier phases, respectively, resulted in the encapsulation of *Gg*Cry4a W369F in microdroplets of approximately 360 pL volumes at a 2 Hz frequency. Under continuous illumination of the microflow at 450 nm, the photoreactive sample in each microdroplet was excited for an average of 105 ms at 70 mW laser power.

5.3.4 *Gg*Cry4a W369F Microdroplet Fluorescence

The first recorded[3] case of fluorescence signals from avian Cry proteins in microdroplets is shown in **Figure 5.4**. At 70 mW laser power, *Gg*Cry4a W369F exhibits fluorescence of $\sim$ 1.38 V in microdroplets with significant background noise. The need for such a high applied laser power (in comparison to 2 mW and 4 mW for the RF$-$Trp and FMN$-$AscH_2 model systems, respectively) is due to the weak quantum fluorescence yield of Crys ($Q_F = 3 \times 10^{-3}$, as reported by Song *et al.* [187]). As a result of the close proximity between the isoalloxazine moiety and the Trp residues ($\sim$5 Å), the ET occurs in $<$1 ps [185], and, therefore, the excited singlet state of ^{1}FAD* is quenched rapidly, significantly reducing the fluorescence quantum yield. However, the fluorescence signal can be improved by increasing the applied laser power and by raising the gain of the PMT detector, although the latter increases the signal, as well as the noise. This is reflected in **Figure 5.4** as the signal is considerably noisy.

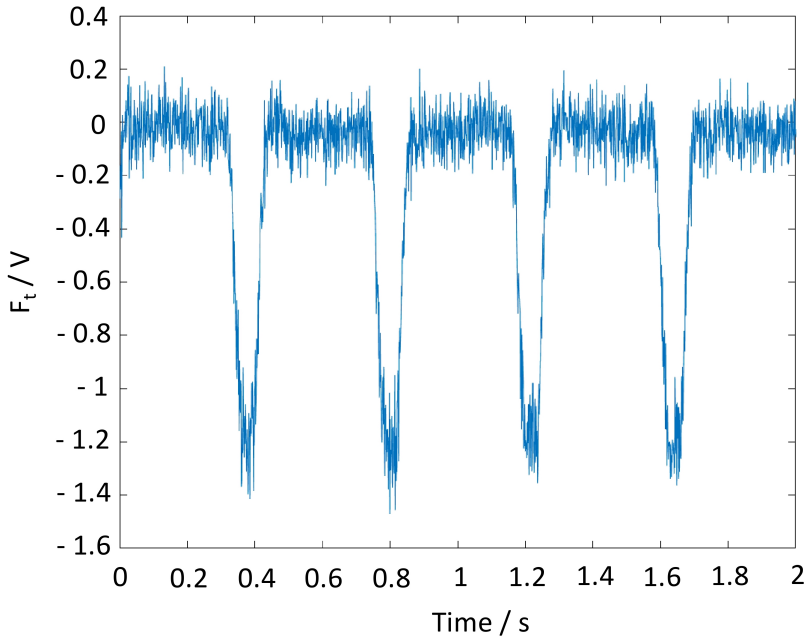


Figure 5.4 PMT signal of fluorescence from microdroplets of *Gg*Cry4a W369F excited at 450 nm in 80 μm microchannels of a flow-focusing microfluidic chip.

[3]Experiments on microdroplets of *Gg*Cry4a W369F were conducted in collaboration with a DPhil student Daniel Cubbin in the Mackenzie group and Dr. Lewis Antill.

5.3.5 Attempts at Measuring Magnetic Field Effects on *Gg*Cry4a W369F

In an attempt to detect MFEs on *Gg*Cry4a encapsulated in microdroplets, an on-off experiment was conducted, during which fluorescence signals with and without a 30 mT magnetic field were acquired. A total of 16,000 microdroplets were measured, resulting in a used sample volume of $\sim 5.76\ \mu$L. **Figure 5.5** shows the averaged PMT response to *Gg*Cry4a W369F microdroplets, indicating no observable MFE. This is mainly due to the poor signal-to-noise ratio (see **Figure 5.4**), which can be improved by acquiring more averages and optimising the experimental conditions to reduce the noise in the experiment.

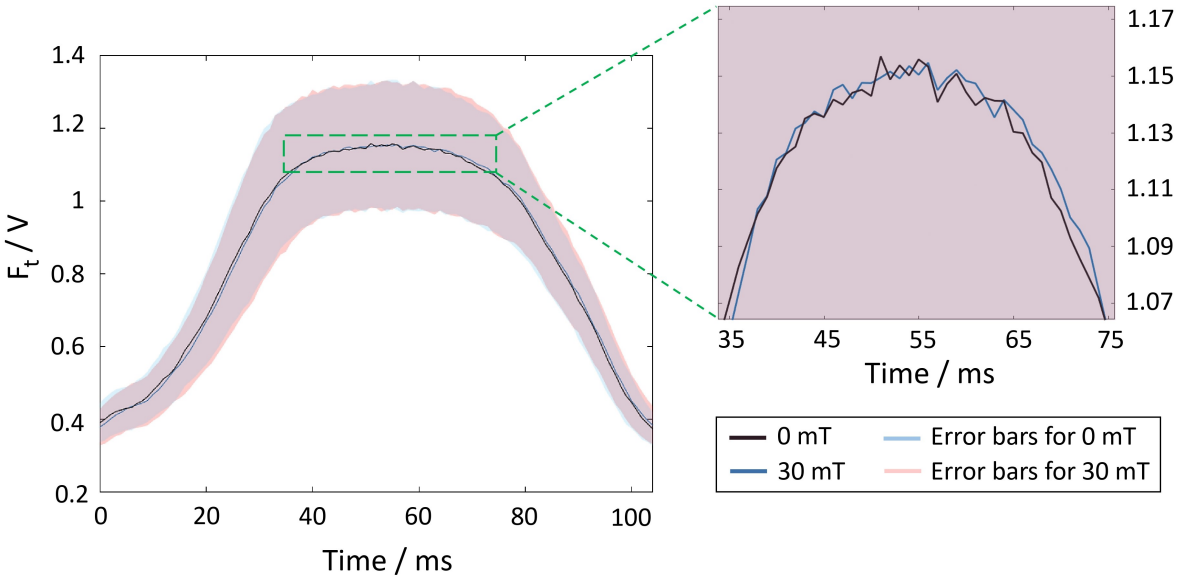


Figure 5.5 Averaged PMT signals for 1,000 averages with and without a 30 mT magnetic field (black and blue, respectively) on microdroplets containing *Gg*Cry4a W369F. The error bars were used as standard deviation. The large errors bars are due to experimental noise and variation of droplet to droplet signals.

5.4 Conclusions and Future Work

The novel method of microdroplet fluorescence is an emerging and highly promising technique to detect MFEs in avian Cry proteins. Its most significant advantage over other conventional methods is reducing the amount of sample consumption, which is of utmost importance to MFE experiments that deal with scarce and limited amounts of avian Cry proteins. For the first time, samples of the mutated *Gg*Cry4a W369F protein were encapsulated in microdroplets with successful detection of their emitted

fluorescence. This shows great promise for MFE detection, as picoliter microdroplet samples allow the sample to be illuminated for less than 200 ms, which mitigates photodegradation and could lead to larger %MFEs.

The work on three model systems ($F-AH_2^+$, $FMN-AscH_2$ and RF−Trp) in **Chapter 4** constitute the successful development of the microdroplet fluorescence technique to detect MFEs in microdroplets. However, the results in **Chapter 5** on microdroplets of *Gg*Cry4a W369F revealed that additional improvements in the experimental technique are required. A more sensitive and stable detector, such as a single photon avalanche diode (SPAD), could improve the stability and signal-to-noise ratio inherent to the system of study, which is currently one of the limiting factors in detecting MFEs in avian Crys. Additionally, the general stability of the experimental setup can be upgraded. Particularly by adding a rigid brace to the free end of the holder arm where the microfluidic chip is inserted, which is currently the most unstable part of the setup. Furthermore, as avian Crys denature at room temperature, a robust sample cooling system is necessary. As it was established that samples need to be in close proximity to the microfluidic chip and the length of tubing needs to be reduced, the cooling of eppendorf vials in their designated sample holders on the circular base plate (*cf.* **Figure 5.2**) needs to be implemented, along with a system to cool the microfluidic chip where samples are measured. Such developments of the microdroplet fluorescence technique would improve the consistency and sensitivity of experimental data acquisition, and provide more automation to the experiment.

The principle motivation of the application of droplet-based microfluidic technology to study MFEs is the capability of measuring complete retinal cells that contain the avian Cry protein. Such models are a more accurate representation of avian Crys in the retinal tissue of migratory birds and would alleviate the time-consuming expression and purification of proteins. With improved sensitivity and stability of the microdroplet fluorescence experimental technique, such cells could potentially be studied, leading to new diverse and fascinating microdroplet-based experiments.

Bibliography

[1] Rodgers, C. T. et al. *Proceedings of the National Academy of Sciences* **2009**, *106*, 353–360.

[2] Komolkin, A. V. et al. *Journal of The Royal Society Interface* **2017**, *14*, 20161002.

[3] Kramer, G. *Naturwissenschaften* **1950**, *37*, 377–378.

[4] Kramer, G. *Ibis* **1952**, *94*, 265–285.

[5] Emlen, S. T. et al. *The Auk* **1966**, *83*, 361–367.

[6] Xu, J. et al. *Nature* **2021**, *594*, 535–540.

[7] Wiltschko, W. et al. *Naturwissenschaften* **2002**, *89*, 445–452.

[8] Schulten, K. et al. *Zeitschrift für Physikalische Chemie* **1978**, *111*, 1–5.

[9] Ritz, T. et al. *Biophysical Journal* **2000**, *78*, 707–718.

[10] Solov'yov, I. et al. *Biophysical Journal* **2010**, *99*, 40–9.

[11] Wiltschko, R. et al. *Biosensors* **2014**, *4*, 221–242.

[12] Kattnig, D. R. et al. *Nature Chemistry* **2016**, *8*, 384–391.

[13] Steiner, U. E. et al. *Chemical Reviews* **1989**, *89*, 51–147.

[14] Ritz, T. et al. *Biophysical Journal* **2009**, *96*, 3451–3457.

[15] Hore, P. J. et al. *Annual Review of Biophysics* **2016**, *45*, 299–344.

[16] Ritz, T. et al. *Journal of the Royal Society Interface* **2010**, *7*, S135–S146.

[17] Klaassen, R. H. et al. *Biology Letters* **2011**, *7*, 833–835.

[18] Gill Jr, R. E. et al. *Proceedings of the Royal Society B: Biological Sciences* **2009**, *276*, 447–457.

[19] Åkesson, S. et al. *PloS one* **2012**, *7*, e41195.

[20] Åkesson, S. et al. *Philosophical Transactions of the Royal Society B: Biological Sciences* **2016**, *371*, 20150393.

[21] Holland, R. A. *Journal of Zoology* **2014**, *293*, 1–15.

[22] Lack, D. *Oikos* **1968**, 1–9.

[23] Guilford, T. et al. *Journal of Experimental Biology* **2011**, *214*, 3705–3712.

[24] Bridge, E. S. et al. *BioScience* **2011**, *61*, 689–698.

[25] Gagliardo, A. *Journal of Experimental Biology* **2013**, *216*, 2165–2171.

[26] Endres, C. et al. *Frontiers in Behavioral Neuroscience* **2016**, *10*, 19.

[27] Lohmann, K. et al. *Ethology, Ecology & Evolution* **1999**, *11*.

[28] Putman, N. et al. *Current Biology* **2011**, *21*, 463–466.

[29] Gould, J. L. *Nature* **1982**, *296*, 205–211.

[30] Wallraff, H. G. *Biogeosciences* **2013**, *10*, 6929–6943.

[31] Butler, R. F. *Paleomagnetism: Magnetic Domains to Geologic Terranes*, 1st ed.; Blackwell Scientific Publishing, 1992.

[32] Weiss, N. *Astronomy & Geophysics* **2002**, *43*, 3–9.
[33] Jordan, T. H. *Proceedings of the National Academy of Sciences* **1979**, *76*, 4192–4200.
[34] Buffett, B. A. *Science* **2000**, *288*, 2007–2012.
[35] *The Earth's Magnetism: An Introduction for Geologists*; Springer Berlin Heidelberg: Berlin, Heidelberg, 2006; pp 1–66.
[36] Buffett, B. A. *Nature* **2010**, *468*, 952–954.
[37] Campbell, W. H. *Introduction to Geomagnetic Fields*, 2nd ed.; Cambridge University Press, 2003.
[38] Meyers, H. et al. *Journal of Geomagnetism and Geoelectricity* **1990**, *42*, 1079–1085.
[39] Barros e Sá, N. et al. *American Journal of Physics* **2022**, *90*, 436–444.
[40] Walt, M. *Introduction to Geomagnetically Trapped Radiation*; Cambridge Atmospheric and Space Science Series; Cambridge University Press, 1994.
[41] Ladynin, A. et al. *Russian Geology and Geophysics* **2009**, *50*, 195–205.
[42] Navabi, M. et al. *Applied Mathematical Modelling* **2017**, *46*, 365–381.
[43] Vogt, J. et al. *Advances in Space Research* **2001**, *28*, 863–868.
[44] Korte, M. et al. *Earth, Planets and Space* **2008**, *60*, 937–948.
[45] Regi, M. et al. *Journal of Geophysical Research: Space Physics* **2021**, *126*, e2020JA028513.
[46] Torsvik, T. H. et al. *Earth-Science Reviews* **2012**, *114*, 325–368.
[47] Courtillot, V. et al. *Science* **1987**, *237*, 1140–1147.
[48] Charvátová, I. et al. *Studia Geophysica et Geodaetica* **2011**, *55*, 159–174.
[49] Lohmann, K. J. et al. *Science* **1987**, *235*, 331–334.
[50] Lohmann, K. J. et al. *Journal of Experimental Biology* **1991**, *161*, 1–24.
[51] Wyeth, R. C. et al. *The Biological Bulletin* **2021**, *240*, 105 – 117.
[52] Gegear, R. J. et al. *Nature* **2008**, *454*, 1014–1018.
[53] Esquivel, D. M. S. et al. *Naturwissenschaften* **2007**, *94*, 139–142.
[54] Pereira-Bomfim, M. et al. *Sociobiology* **2015**, *62*.
[55] Wajnberg, E. et al. *Journal of The Royal Society Interface* **2010**, *7*, S207–S225.
[56] Lucano, M. et al. *BioMetals* **2006**, *19*, 295–300.
[57] Quinn, T. P. *Journal of Comparative Physiology* **1980**, *137*, 243–248.
[58] Taylor, P. *Journal of Fish Biology* **1986**, *28*, 607–623.
[59] Phillips, J. B. *Journal of Comparative Physiology* **1977**, *121*, 273–288.
[60] Phillips, J. B. *Journal of Comparative Physiology A* **1986**, *158*, 103–109.
[61] Phillips, J. B. *Science* **1986**, *233*, 765–767.
[62] Sinsch, U. *Journal of Comparative Physiology A* **1987**, *161*, 715–727.
[63] Sinsch, U. *Ethology, Ecology & Evolution* **1992**, *4*, 15–32.
[64] Lohmann, K. J. *Journal of Experimental Biology* **1991**, *155*, 37–49.
[65] Lohmann, K. J. et al. *Journal of Comparative Physiology A* **2022**, 1–27.
[66] Mathis, A. et al. *Ethology* **1988**, *78*, 265–274.
[67] Merrill, M. W. et al. *Marine Biology* **2011**, *158*, 101–112.
[68] Walcott, C. *Journal of Experimental Biology* **1996**, *199*, 21–27.
[69] Keeton, W. T. *Proceedings of the National Academy of Sciences* **1971**, *68*, 102–106.

[70] Gould, J. L. *Annual Review of Physiology* **1984**, *46*, 585–598.
[71] Mora, C. V. et al. *Nature* **2004**, *432*, 508–511.
[72] Wu, L.-Q. et al. *Current Biology* **2011**, *21*, 418–423.
[73] Falkenberg, G. et al. *PLoS One* **2010**, *5*, e9231.
[74] Wiltschko, W. et al. *Journal of Experimental Biology* **2007**, *210*, 2300–2310.
[75] Freire, R. et al. *Journal of Animal Science* **2011**, *89*, 1201–1206.
[76] Mather, J. G. et al. *Nature* **1981**, *291*, 152–155.
[77] Malkemper, E. P. et al. *Scientific reports* **2015**, *5*, 9917.
[78] Marhold, S. et al. *Naturwissenschaften* **1997**, *84*, 421–423.
[79] Nemec, P. et al. *Science* **2001**, *294*, 366–368.
[80] Holland, R. A. et al. *Nature* **2006**, *444*, 702–702.
[81] Holland, R. A. et al. *Proceedings of the National Academy of Sciences* **2010**, *107*, 6941–6945.
[82] von Middendorf, A. T. *Die Isepiptesen Russlands: Grundlagen zur Erforschung der Zugzeiten und Zugrichtungen der Vögel Russlands*; Buchdruckerei der K. Akademie der Wissenschaften, 1855.
[83] Emlen, S. T. et al. *The Auk* **1966**, *83*, 361–367.
[84] Kerpal, C. et al. *Nature Communications* **2019**, *10*, 1–7.
[85] Biro, D. et al. *Proceedings of the National Academy of Sciences* **2007**, *104*, 7471–7476.
[86] Foster, J. J. et al. *Proceedings of the Royal Society B: Biological Sciences* **2018**, *285*, 20172322.
[87] Sauer, E. G. F. *Scientific American* **1958**, *199*, 42–47.
[88] Wiltschko, R. et al. *Oxford Research Encyclopedia of Neuroscience*; 2023.
[89] Wiltschko, W. et al. *Naturwissenschaften* **2001**, *88*, 387–390.
[90] Richardson, W. J. *Oikos* **1978**, *30*, 224–272.
[91] Wiltschko, R. et al. *Journal of the Royal Society Interface* **2010**, *7*, S163–S177.
[92] Wiltschko, W. et al. *Nature* **1993**, *364*, 525–527.
[93] Horst, G. T. v. d. et al. *Nature* **1999**, *398*, 627–630.
[94] Chaves, I. et al. *Annual Review of Plant Biology* **2011**, *62*, 335–364.
[95] Mondal, P. et al. *Journal of Photochemistry and Photobiology A: Chemistry* **2020**, *387*, 112164.
[96] Medina, M. et al. *Journal of the Chemical Society, Perkin Transactions 2* **1996**, 633–638.
[97] Massey, V. *Biochemical Society Transactions* **2000**, *28*, 283–296.
[98] de Or Arrivetti, L. et al. *Journal of Agricultural and Food Chemistry* **2013**, *61*, 7615–7620.
[99] Zoltowski, B. D. et al. *Biochemistry* **2011**, *50*, 4–16.
[100] Hemmerich, P. et al. *FEBS letters* **1970**, *8*, 69–83.
[101] Conrad, K. S. et al. *Nature Chemical Biology* **2014**, *10*, 801–809.
[102] Alexov, E. *European Journal of Biochemistry* **2004**, *271*, 173–185.
[103] Penzkofer, A. *Journal of Photochemistry and Photobiology A: Chemistry* **2016**, *314*, 114–124.
[104] Weber, S. et al. *Flavins and Flavoproteins: Methods and Protocols*; Springer, 2014.

[105] Salzmann, S. et al. *Journal of Photochemistry and Photobiology A: Chemistry* **2008**, *198*, 221–231.
[106] Sikorska, E. et al. *Journal of Fluorescence* **2004**, *14*, 57–64.
[107] Ren, S. et al. *Plant and Cell Physiology* **2012**, *53*, 1638–1647.
[108] Knowles, A. et al. *Photochemistry and Photobiology* **1972**, *15*, 199–207.
[109] Li, G. et al. *The Journal of Physical Chemistry A* **2008**, *112*, 4573–4583.
[110] Moore, W. M. et al. *Photochemistry and Photobiology* **1977**, *25*, 505–512.
[111] Reichert, D. et al. *Frontiers in Oncology* **2023**, *13*, 1105648.
[112] Wingen, M. et al. *Photochemical & Photobiological Sciences* **2014**, *13*, 875–883.
[113] Evans, E. W. et al. *The Journal of Chemical Physics* **2016**, *145*.
[114] Tsentalovich, Y. P. et al. *Spectrochimica Acta Part A: Molecular and Biomolecular Spectroscopy* **2002**, *58*, 2043–2050.
[115] Kennis, J. T. et al. *Biochemistry* **2003**, *42*, 3385–3392.
[116] Evans, E. W. et al. *Physical Chemistry Chemical Physics* **2015**, *17*, 18456–18463.
[117] Sichula, V. et al. *The Journal of Physical Chemistry A* **2010**, *114*, 12138–12147.
[118] Ahmad, I. et al. *Flavins Photochemistry and Photobiology*; The Royal Society of Chemistry, 2006.
[119] Ernst, S. et al. *Nature Communications* **2020**, *11*, 2600.
[120] Zhuang, B. et al. *The Journal of Physical Chemistry B* **2022**, *126*, 3199–3207.
[121] Yuan, S. et al. *Wiley Interdisciplinary Reviews: Computational Molecular Science* **2017**, *7*, e1298.
[122] Lukacs, A. et al. *Journal of the American Chemical Society* **2008**, *130*, 14394–14395.
[123] Nießner, C. et al. *PloS one* **2011**, *6*, e20091.
[124] Wiltschko, W. et al. *Nature* **2002**, *419*, 467–470.
[125] Saey, T. H. *Science News* **2015**, *187*, 22–26.
[126] Schulten, K. et al. *Biophysical Effects of Steady Magnetic Fields* **1986**, *11*, 99–106.
[127] Atkins, P. et al. *Physical Chemistry*; Oxford University Press: Oxford, 2018.
[128] Atkins, P. W. et al. *Molecular Quantum Mechanics*; Oxford University Press, 2011.
[129] Dirac, P. A. M. *Proceedings of the Royal Society London, Series A* **1928**, *117*, 610–624.
[130] Schwinger, J. *Physical Review* **1948**, *73*, 416–417.
[131] Odom, B. et al. *Physical Review Letters* **2006**, *97*, 030801.
[132] Rodgers, C. T. *Pure and Applied Chemistry* **2009**, *81*, 19–43.
[133] Pauli, W. *Naturwiss* **1924**, *12*, 741.
[134] Sekiguchi, S. et al. *Journal of the American Chemical Society* **1998**, *120*, 1325–1326.
[135] Kuprov, I. *Spin: From Basic Symmetries to Quantum Optimal Control*; Springer Nature, 2023.
[136] Lewis, A. M. et al. *The Journal of Chemical Physics* **2018**, *149*.
[137] Grissom, C. B. *Chemical Reviews* **1995**, *95*, 3–24.
[138] Schweiger, A. et al. *Principles of Pulse Electron Paramagnetic Resonance*; Oxford University Press, 2001.
[139] Wong, S. Y. et al. *Physical Chemistry Chemical Physics* **2023**, *25*, 975–982.
[140] Timmel, C. R. et al. *Molecular Physics* **1998**, *95*, 71–89.

[141] Niculescu, A.-G. et al. *International Journal of Molecular Sciences* **2021**, *22*, 2011.
[142] Bruus, H. *Theoretical Microfluidics*; Oxford university press, 2007; Vol. 18.
[143] Maillefer, D. et al. A High-Performance Silicon Micropump For Disposable Drug Delivery Systems. Technical Digest. MEMS 2001. 14th IEEE International Conference on Micro Electro Mechanical Systems (Cat. No. 01CH37090). 2001; pp 413–417.
[144] Tay, F. E. *Microfluidics and BioMEMS Applications*; Springer, 2002.
[145] Herold, K. E. et al. *Lab on a Chip Technology: Biomolecular Separation and Analysis*; Horizon Scientific Press, 2009; Vol. 2.
[146] Ali, M. et al. In *Smart Nanocontainers*; Nguyen-Tri, P. et al. , Eds.; Micro and Nano Technologies; Elsevier, 2020; pp 515–536.
[147] Landau, L. D. et al. *Fluid Mechanics: Landau And Lifshitz: Course of Theoretical Physics, Volume 6*; Elsevier, 2013; Vol. 6.
[148] Childs, P. R. In *Rotating Flow*; Childs, P. R., Ed.; Butterworth-Heinemann: Oxford, 2011; pp 17–52.
[149] Squires, T. M. et al. *Reviews of Modern Physics* **2005**, *77*, 977.
[150] Zhu, P. et al. *Lab on a Chip* **2017**, *17*, 34–75.
[151] Colin, S. *Microfluidics*; John Wiley & Sons, 2013.
[152] Baroud, C. N. et al. *Lab on a Chip* **2010**, *10*, 2032–2045.
[153] Seemann, R. et al. *Reports on Progress in Physics* **2011**, *75*, 016601.
[154] Garstecki, P. et al. *Physical Review Letters* **2005**, *94*, 164501.
[155] Taylor, G. *Journal of Fluid Mechanics* **1961**, *10*, 161–165.
[156] Schwartz, L. et al. *Journal of Fluid Mechanics* **1986**, *172*, 259–275.
[157] Hazel, A. L. et al. *Journal of Fluid Mechanics* **2002**, *470*, 91–114.
[158] Jousse, F. et al. *Lab on a Chip* **2005**, *5*, 646–656.
[159] Hodges, S. et al. *Journal of Fluid Mechanics* **2004**, *501*, 279–301.
[160] de Lozar, A. et al. *Physical Review Letters* **2007**, *99*, 234501.
[161] Günther, A. et al. *Langmuir* **2005**, *21*, 1547–1555.
[162] Antill, L. M. et al. *The Journal of Physical Chemistry Letters* **2018**, *9*, 2691–2696.
[163] Stob, S. et al. *Journal of the American Chemical Society* **1989**, *111*, 7036–7042.
[164] Van Schagen, C. G. et al. *Biochemistry* **1982**, *21*, 402–407.
[165] Murakami, M. et al. *The Journal of Physical Chemistry A* **2005**, *109*, 5793–5800.
[166] Murakami, M. et al. *Chemical Physics Letters* **2002**, *362*, 123–129.
[167] Merk, V. et al. *Applied Spectroscopy* **2021**, *75*, 994–1002.
[168] Beardmore, J. P. et al. *Angewandte Chemie international edition* **2015**, *54*, 8494–8497.
[169] Kerpal, C. et al. *Nature Communications* **2019**, *10*, 3707.
[170] Brocklehurst, B. *Journal of the Chemical Society, Faraday Transactions 2: Molecular and Chemical Physics* **1976**, *72*, 1869–1884.
[171] Arrigoni, O. et al. *Biochimica et Biophysica Acta (BBA)-General Subjects* **2002**, *1569*, 1–9.
[172] Carr, A. C. et al. *Nutrients* **2017**, *9*, 1211.
[173] Murton, P. Characterisation of Magnetic Field Effects Through Sensitive Spectroscopic Measurement. Ph.D. thesis, University of Oxford, 2024.

[174] Wei, Z. et al. *Annual Review of Physical Chemistry* **2020**, *71*, 31–51.
[175] Yu, Q. et al. *Chaos, Solitons & Fractals* **2022**, *155*, 111774.
[176] Hiscock, H. G. et al. *Proceedings of the National Academy of Sciences* **2016**, *113*, 4634–4639.
[177] Dejean, V. Towards the Detection of Anisotropic Magnetic Field Effects in Flavin-Based Systems. Ph.D. thesis, University of Oxford, 2021.
[178] Štuhec, A. A Theoretical and Experimental Investigation of Magnetic Field Effects Using Confoncal Microscopy. Ph.D. thesis, University of Oxford, 2021.
[179] Konowalczyk, M. High-Sensitivity Measurements of Weak Magnetic Field Effects. Ph.D. thesis, University of Oxford, 2020.
[180] Slominski, A. et al. *FEBS Letters* **2002**, *511*, 102–106.
[181] Maeda, K. et al. *Proceedings of the National Academy of Sciences* **2012**, *109*, 4774–4779.
[182] Sheppard, D. M. et al. *Scientific Reports* **2017**, *7*, 42228.
[183] Golesworthy, M. J. et al. *The Journal of Chemical Physics* **2023**, *159*.
[184] Gravell, J. et al. *Spectroscopic characterisation of radical pair photochemistry in avian cryptochromes: Magnetic field effects in GgCry4a (in review)* **2024**,
[185] Timmer, D. et al. *Journal of the American Chemical Society* **2023**, *145*, 11566–11578.
[186] Nohr, D. et al. *Biophysical Journal* **2016**, *111*, 301–311.
[187] Song, S.-H. et al. *Journal of Photochemistry and Photobiology B: Biology* **2006**, *85*, 1–16.
[188] Sakurai, J. J. et al. *Modern Quantum Mechanics*; Cambridge University Press, 2020.
[189] Gokcen, N. A. et al. *Thermodynamics*; Springer Science & Business Media, 2013.
[190] Weijermars, R. et al. *Energies* **2019**, *12*, 1243.

BACK MATTER

List of Figures

1.1 Earth's geographic and magnetic poles and the movement of Earth's north magnetic pole across the Canadian Arctic 3

1.2 Earth's *North-East-Down* spatial coordinate reference system 4

1.3 Illustration of the paper funnels used for behavioural experiments on European robins and subsequent experimental results on their migration directions recorded in autumn 2000 and spring 2001 6

1.4 Spectra of light-emitting diodes used in behavioural experiments and their following experimental results on European robins 7

1.5 The chemical structures of flavin adenine dinucleotide (FAD), flavin mononucleotide (FMN) and riboflavin (RF) 8

1.6 Proton transfer tautomerism of alloxazine and isoalloxazine 9

1.7 Redox and protonation states of the 7,8-dimethylisoalloxazine ring 9

1.8 Experimental absorption and fluorescence spectra of an aqueous solution of oxidised FMN 10

1.9 A simplified diagram illustrating photochemical excitation and decay processes in oxidised flavins 12

1.10 Homology model of the chicken cryptochrome 4a protein (*Gg*Cry4a) 13

1.11 Illustration of the localisation of the Cry protein inside a bird's retinal tissue . . 14

2.1 Vector representation of the two possible orientations of an electron with spin-$\frac{1}{2}$ in a magnetic field 18

2.2 Vector model representation of the singlet and triplet spin states 21

2.3 The Zeeman effect on a system with one and two spin-$\frac{1}{2}$ electrons 24

2.4 Interaction of the aligned magnetic dipoles moments μ_e and μ_n originating from an electron and nuclear spins 27

2.5 Precession of the angular momentum vector along an arbitrary z-axis 30

2.6 Simplified radical pair mechanism photocycle with an electron acceptor and an electron donor 33

2.7 Qualitative diagram of a MARY curve, showing the low and high field effects . . 35

3.1 Visual representations of the Eulerian and Lagrangian descriptions 41

3.2 Infinitesimal control volume of an arbitrary region of space, Σ, for the derivation of the mass current density, $\boldsymbol{J}$ 42

3.3 Vectorial visualisation of forces acting on molecules inside a liquid and at its surface 47

3.4 A flow-focusing microfluidic chip together with an illustrative picture of a parabolic velocity field profile of a microflow 49

3.5 Schematics of a co-flow, cross-flow and flow-focusing microfluidic chips 52

3.6 Microdroplet formation in a flow-focusing microfluidic chip with the photoactive sample encapsulated within the laser beam path 53

3.7 Cross-section view of a microdroplet in a circular microchannel and the mixing currents in microdroplets of the carrier and dispersed phases 55

3.8 Fluorescence emission from a microdroplet by a laser beam and its PMT response to the emitted fluorescence signal 57

3.9 Digital CAD drawings of 3D models of the sample holder, featuring the holder arm and circular microfluidic chip holder 58

3.10 Schematic outline of the custom built microdroplet fluorescence experimental setup 59

3.11 Qualitative example of positive and negative sigmoid functions, centred at $x = 0$ 62

3.12 Fluorescence signal data extraction from all individual microdroplets and their average variation 63

4.1 Chemical structure of adenine (AH) and the $\mathrm{F{-}AH}_2^+$ radical pair mechanism photocycle 66

4.2 FAD emission spectrum from microdroplets and experimental results from laser power dependence measurements 68

4.3 Averaged microdroplet PMT signals with and without a 30 mT magnetic field on FAD and MARY results for different applied laser powers 69

4.4 Chemical structure of ascorbic acid ($AscH_2$) and the FMN−$AscH_2$ radical pair mechanism photocycle 71

4.5 Averaged microdroplet PMT signals with and without a 30 mT magnetic field on FMN−$AscH_2$ 73

4.6 Fluorescence spectra of FMN−$AscH_2$ with an without a 550 nm long-pass filter 73

4.7 MARY plots on microdroplets containing FMN and $AscH_2$ at pH 3 and pH 7 . . . 74

4.8 Histogram of illumination time consistency across microdroplets acquired during a MARY experiment on FMN−$AscH_2$ 76

4.9 Chemical structure of tryptophan (TrpH) and the RF−TrpH radical pair mechanism photocycle 77

4.10 MARY plots recorded at 2 mW power on RF−TrpH in microchannels of different diameter and in a bulk solution 79

5.1 Homology model of the mutated chicken cryptochrome 4a protein (*Gg*Cry4a) W369F 83

5.2 Digital CAD drawing of 3D models of the sample holder adopted for the MFE analysis of Cry proteins, including a new circular base plate, a rigid circular clamp and the holder arm with both parts implemented 85

5.3 The radical pair mechanism photocycle of FAD−TrpH in the *Gg*Cry4a W369F mutant protein. 87

5.4 PMT signal of fluorescence from microdroplets of *Gg*Cry4a W369F 88

5.5 Averaged PMT signals with and without a 30 mT applied magnetic field on microdroplets containing *Gg*Cry4a W369F 89

A.1 Quantum mechanical spin dynamics simulation to illustrate how magnetic fields affect RPs and the evolution of the RPM 109

C.1 Applied flow pressures for the FMN−$AscH_2$ model system 117

C.2 RF−TrpH fluorescence spectra with and without a 550 nm long-pass filter . . . 118

List of Tables

2.1 The uncoupled basis for a two spin-$\frac{1}{2}$ system 20

2.2 The coupled basis for a two spin-$\frac{1}{2}$ system 21

4.1 Summary of the MARY experimental results using increasing excitation powers on the $F-AH_2^+$ model system 69

4.2 Summary of FMN-AscH_2 model system MARY results 74

4.3 Summary of experimental conditions for the RF−TrpH model system 78

4.4 Summary of MARY results on the RF−TrpH model system microdroplet diffusion confinement a bulk solution experiments 79

C.1 Experimental results of the averaged applied flow rates for the FMN−AscH_2 model system 117

Appendices

Appendix A

Quantum Mechanical Spin Dynamics Simulation on Radical Pairs

It is important to highlight that the energy of interaction for an electron spin under the influence of the Earth's magnetic field (30−60 μT) is about six order of magnitude smaller than the thermal energy, k_BT, at 298 K [1, 2, 12, 15, 84, 113, 139]. It is, therefore, unlikely, from the viewpoint of thermodynamics, that such weak magnetic fields could have significantly alter chemical reaction yields. Nevertheless, experimental measurements [6, 12, 173, 177–179] show that the application of Earth-strength magnetic fields alters the spin dynamics of RP reactions.

The following appendix introduces the necessary foundations of density matrix formalism, required to present a theoretical simulation of spin dynamics, which illustrates the effect that magnetic fields have on RPs.

A.1 Introduction to Density Matrix Formalism

The density matrix formalism is used in quantum mechanics to describe the statistical state of a quantum system. Using the expansion of a quantum state in terms of an arbitrary basis, any quantum state can be defined as follows [188]:

$$|\psi\rangle = \sum_n c_n \, |\phi_n\rangle \, , \tag{A.1}$$

where $|\psi\rangle$ represents the quantum state of the system, $|\phi_n\rangle$ constitutes the basis states of orthonormal set of vectors $\{|\phi_n\}\rangle$ and c_n is the expansion coefficient, calculated as the projection of the state $|\psi\rangle$ with the basis state $|\phi_n\rangle$:

$$c_n = \langle \phi_n | \psi \rangle \, . \tag{A.2}$$

The density matrix describing such a system is written as the following [188]:

$$\hat{\rho} = |\psi\rangle \langle\psi| = \sum_{nm} c_m^* c_n |\phi\rangle \langle\phi| . \tag{A.3}$$

The time evolution of a density matrix in quantum mechanics can be taking the time-dependent Schrödinger equation [188]:

$$\frac{d}{dt} |\psi(t)\rangle = -\frac{i}{\hbar} \hat{H}(t) |\psi(t)\rangle . \tag{A.4}$$

To solve the Schrödinger equation, the time evolution operator , which allows to evaluate how any state evolves over time, needs to be introduced [188]:

$$\hat{U}(t) = \hat{\mathcal{T}} \exp\left(-\frac{i}{\hbar} \int_0^t \hat{H}(t')\, dt'\right), \tag{A.5}$$

where $\hat{\mathcal{T}}$ is the time ordering operator. $\hat{U}(t)$ thus constitutes the solution to the Schrödinger equation in the following way [188]:

$$|\psi(t)\rangle = \hat{U}(t) |\psi(0)\rangle . \tag{A.6}$$

Substituting **Equation A.6** into **Equation A.3** yields the following:

$$\begin{aligned} \hat{\rho}(t) &= \left(\hat{U}(t) |\psi(0)\rangle\right) \left(\langle\psi(0)| \hat{U}(t)^\dagger\right); \\ &= \hat{U}(t) |\psi(0)\rangle \langle\psi(0)| \hat{U}(t)^\dagger; \\ &= \hat{U}(t) \hat{\rho}(0) \hat{U}(t)^\dagger, \end{aligned} \tag{A.7}$$

which is the solution to the fundamental equation of spin dynamics, known as the *Liouville von-Neumann Equation* [188]:

$$\frac{d}{dt} \hat{\rho}(t) = -\frac{i}{\hbar} [\hat{H}(t), \hat{\rho}(t)]. \tag{A.8}$$

The expectation value of an arbitrary observable $\hat{O}$ in a quantum state $|\psi\rangle$ is given by the following [188]:

$$\langle \hat{O} \rangle = \langle\psi| \hat{O} |\psi\rangle . \tag{A.9}$$

Using the definition presented in **Equation A.1**, we can rewrite **Equation A.9** by the following:

$$\begin{aligned}\langle \hat{O} \rangle &= \left(\sum_m c_m^* \langle \phi_m | \right) \hat{O} \left(\sum_n c_n |\phi_n\rangle \right); \\ &= \sum_m \sum_n c_m^* \langle \phi_m | \hat{O} | \phi_n \rangle c_n.\end{aligned} \tag{A.10}$$

The term $\langle \phi_m | \hat{O} | \phi_n \rangle$ is the matrix element of $\hat{O}$ in the basis $\{|\phi_n\rangle\}$, which, by definition, is denoted as [188]:

$$\begin{cases} \langle \phi_m | \hat{O} | \phi_n \rangle = \hat{O}_{mn}; \\ Tr\left[|\phi_m\rangle \langle \phi_n | \hat{O} \right] = \hat{O}_{mn}. \end{cases} \tag{A.11}$$

Therefore, **Equation A.10** can be written as:

$$\langle \hat{O} \rangle = \sum_{mn} c_m^* \hat{O}_{mn} c_n. \tag{A.12}$$

Because **Equation A.12** displays a multiplication of scalars c_m^* and c_n which is a commutative operation, c_m^* and c_n can be rearranged in the following way:

$$\begin{aligned}\langle \hat{O} \rangle &= \sum_{mn} c_m^* c_n \hat{O}_{mn}; \\ &= \sum_{mn} c_n c_m^* \hat{O}_{mn}.\end{aligned} \tag{A.13}$$

Using **Equation A.11**, we can thus say the following:

$$\begin{aligned}\langle \hat{O} \rangle &= \sum_{mn} c_n c_m^* \, Tr\left[|\phi_m\rangle \langle \phi_n | \hat{O} \right]; \\ &= Tr\left[\sum_{mn} c_n c_m^* |\phi_m\rangle \langle \phi_n | \hat{O} \right].\end{aligned} \tag{A.14}$$

By substitution with **Equation A.3**, the following can be written:

$$\langle \hat{O} \rangle = Tr\left[\hat{\rho}(t) \hat{O} \right], \tag{A.15}$$

which defines the expectation value of the observable $\hat{O}$ at time t for a given density matrix $\hat{\rho}(t)$.

Equations A.1–**A.15** constitute the core foundation of the density matrix formalism.

A.2 Details of the Quantum Spin Dynamics Simulation

If we consider the RPM presented in **Figure 2.6**, the associated SCRP can undergo singlet-triplet interconversion upon the application of magnetic fields. This can be explained by evaluating the time-dependent probability of finding the system in the singlet state [140]:

$$p_S(t) = Tr\left[\hat{P}_S\hat{\rho}(t)\right], \tag{A.16}$$

with $\hat{P}_S$ defined as the singlet projection operator for the $|S\rangle$ state:

$$\hat{P}_S = |S\rangle\langle S|. \tag{A.17}$$

The fraction of triplet RPs at time t can be defined as follows [140]:

$$p_T(t) = 1 - p_S(t). \tag{A.18}$$

Following the description of the simulations presented by Timmel *et al.* [140], the considered RP consists of:

- a single magnetic nucleus with spin quantum number $s = \frac{1}{2}$;
- a 500 μT isotropic hyperfine coupling;
- a pure singlet state at time $t = 0$.

The triplet state RP density matrix, $\hat{\rho}_T$, and the yield of RP2 (see **Figure 2.6**) is expressed as follows:

$$\hat{\rho}_T = \frac{\hat{Q}_T}{Tr\left[\hat{Q}_T\right]}; \tag{A.19}$$

$$\left[RP\,2\right]_t = k\int_0^t p_T(t')dt', \tag{A.20}$$

where $\hat{Q}_T$ is the triplet projection operator:

$$\hat{Q}_T = \frac{3}{4}I + \hat{S}_A\hat{S}_B. \tag{A.21}$$

The simulation[1] was performed with no applied magnetic field (**Figure A.1a**) or a 50 μT (Earth-strength) magnetic field (**Figure A.1b**). The kinetics are first order with no interradical interactions or spin relaxation considered.

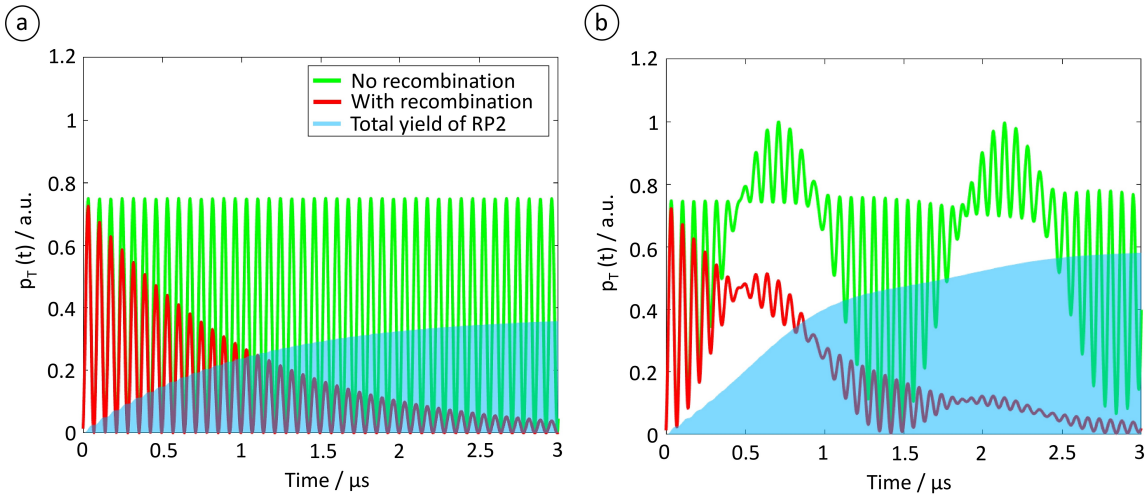


Figure A.1 Quantum mechanical spin dynamics simulation for when (a) no magnetic field is applied and (b) a 50 μT magnetic field is applied. In both figures, the green traces show the time dependence of the fraction of RPs existing in the triplet state, $p_T(t)$,with no chemical reactivity present (*i.e.*, $k_{BET} = k^S_{Diss} = k^T_{Diss} = 0$, as noted in **Figure 2.6**). The red and green traces represent, respectively, $p_T(t)$ and the yield of long-lived radicals, RP2, shown in blue, when chemical reactivity is considered (*i.e.*, $k_{BET} = k^S_{Diss} = k^T_{Diss} = 10^6$ s^{-1}).

Figure A.1a shows that, without a magnetic field and no recombination (green), the extent of singlet-triplet mixing remains constant over time and the fraction of RPs in the triplet state, $p_T(t)$, oscillates at the hyperfine coupling frequency (14 MHz). This produces a total yield of RP2 of 0.356. However, when a weak magnetic field is introduced (**Figure A.1b**), the singlet-triplet mixing has an additional fluctuation at the frequency of the external magnetic field (1.4 MHz). RP reactions result in an exponential decrease of $p_T(t)$ (red), enabling the total yield of long-lived radical to rise to 0.579 (green). Therefore, an Earth-strength magnetic field enhances singlet-triplet interconversion of RPs, hence increasing the accumulation of the RP2 state by 62.6%.

A.3 *MATLAB* Code

```
%% Density matrix simulation for the time evolution of a one proton radical pair
%
% Developed by Dr. Lewis Antill, Saitama 2021

% clear; clc; close all;
```

[1]The simulation code was developed by Dr. Lewis Antill in *MATLAB*.

```
%% Pauli Matrices

Sx=[0 1/2; 1/2 0]; Sy=[0 -1i/2; 1i/2 0]; Sz=[1/2 0; 0 -1/2]; unit=[1 0; 0 1];


%% Spin operators - 2 electrons and 1 nucleus (proton)

kkron=@(x,y,z) kron(kron(x,y),z);

SxA=(kkron(Sx,unit,unit)); SyA=(kkron(Sy,unit,unit)); SzA=(kkron(Sz,unit,unit));
SxB=(kkron(unit,Sx,unit)); SyB=(kkron(unit,Sy,unit)); SzB=(kkron(unit,Sz,unit));
IxA=(kkron(unit,unit,Sx)); IyA=(kkron(unit,unit,Sy)); IzA=(kkron(unit,unit,Sz));

%% Product operators

SASB=SxA*SxB+SyA*SyB+SzA*SzB;
SAIA=SxA*IxA+SyA*IyA+SzA*IzA;

%% Constants for the Hamiltonian

kb=1.38e-23; %Boltzman Constant
hfc=0.5; % hyperfine coupling constant
J=-0.0; % J-coupling constant
B0=0.05; %0.05; %Applied magnetic field - change between 0 and 0.05 to generate
different figures
gn=267.513e3; % Hydrogen nucleus magentogyric ratio in rad/s/mT
ge=1.760859644e8; % Electron magentogyric ratio in rad/s/mT
T=linspace(0,3e-6,1000); dt=T(2)-T(1); %Time vector
kr=1e6; %recombination rate (/s) - change between 0 and 1e6 to generate different
figures
temp=310; %K
hbar=1.05457182e-34 %Reduced Planck constant

%% Projection operators

QS=1/4*eye(size(SASB))-SASB; % S
QT=3/4*eye(size(SASB))+SASB; % T+,T0,T- or eye(size(SASB))-PS
QTp=(2*SzA^2+SzA)*(2*SzB^2+SzB); % T+
QTm=(2*SzA^2-SzA)*(2*SzB^2-SzB); % T-
QT0=QT-QTp-QTm; % T0
QTpm=QTp+QTm;

%% Hamiltonian

a=ge*hfc; % Hyperfine coupling constant
omega0=ge*B0; % Electron Larmor frequency
omega0n=-gn*B0; % Nuclear Larmor frequency
Jcoup=ge*J; % J-coupling constant

Hzee=omega0.*(SzA+SzB)+omega0n.*IzA; % Zeeman Hamiltonian
Hhyper=a*SAIA; % Hyperfine Hamiltonian
Hex=-Jcoup*SASB; % Heisenberg-Dirac-van Vleck (HDVV) spin Hamiltonian
H=Hzee+Hhyper+Hex; % Full Hamiltonian

%% Initial density matrices

rho0QS=QS/trace(QS); % Singlet
rho0QT=QT/trace(QT); % Triplet
rho0QTp=QTp/trace(QTp); % T+
```

```
rho0QTm=QTm/trace(QTm); % T-
rho0QT0=QT0/trace(QT0); % T0
rho0QTpm=((QTp/trace(QTp))/2)+((QTm/trace(QTm))/2); % T+-
% Equilibrium state
beta=hbar/(kb*temp);
rho0eq=expm(-1i*H*beta);
rho0eq=rho0eq/trace(rho0eq);

%% Propagator matrices

Um=expm(-1i*H*dt); Up=expm(1i*H*dt);
rho0p=rho0QS; %spin density at the previous timestep

%% Observables on the density matrix

obsQS=real(trace(QS*rho0QS)); %singlet yield
obsQT=1-real(trace(QS*rho0QS)); %triplet yield
obsQTp=real(trace(QTp*rho0QTp)); %T+ yield
obsQTm=real(trace(QTm*rho0QTm)); %T- yield
obsQT0=real(trace(QT0*rho0QT0)); %T0 yield
obsQTpm=real(trace(QTpm*rho0QTpm)); %T+- yield

%% Calculate the time evolution

sig=zeros(1,length(T)); sig2=NaN(1,length(T));% Prealocate the matrix for the
signal
sig(1)=obsQS; % Calculate the observable of the initial density matrix
sig2(1)=obsQS;

rsig=5e-10; % Recombination distance
r0=9e-10; % Created separation distance
D=1e-5/10000; % m^2/s Relative diffusion coefficient
tauD=rsig^2/D; % Diffusional lifetime
a=(rsig*(r0-rsig))/(r0*sqrt(4*pi*D));
b=((r0-rsig)^2)/(4*D);

cm=viridis;

for i=1:length(T)
    % Propagate the density matrix by dt
    rhot=Um*rho0p*Up;
    rhot=rhot/trace(rhot);
    rho0p=rhot;

    % Calculate the observable at time t
    % sig(i)=real(trace(QT*rhot)); % No recombination
    f=exp(-kr*T(i)); % Exponential model
    sig2(i)=(real(trace(QT*rhot)).*f) ;
end

%% Calculate the yield of the RP2 species

YieldRP2=cumtrapz(T,sig2).*kr;
YieldRP2sum=sum(sig2,2).*dt.*kr;

%% Plotting

figure(2)
plot(1e6*T,sig2,'r','LineWidth',2)
```

```
hold on
area(1e6*T,YieldRP2,'FaceColor',[0 .7 1],'EdgeColor','none','FaceAlpha',0.5)
%'FaceColor',[0 .7 1]
xlabel('\itt\rm\bf  / \mus')
ylabel('{\itP}_{T}(\itt\rm\bf)');
set(gca,'box','off','FontSize',14,'LineWidth',2);
ylim([0 1]);
```

Appendix B

Spherical Shape of Droplets and Minimisation of Surface Area

B.1 Second Law of Thermodynamics

For closed systems that cannot exchange matter but can transfer other forms of energy, the second law of thermodynamics states that heat transfers energy spontaneously from higher- to lower-temperature objects, but never spontaneously in the other direction. This is usually expressed using *entropy* for a given internal energy [128]:

$$\Delta S = \frac{Q_{rev}}{T}, \tag{B.1}$$

where ΔS is the total change in entropy, Q_{rev} is the reversible heat transfer and T is the temperature at which the heat is transferred. For an isolated system which can neither exchange matter, nor transfer any type of energy with its surroundings [128]:

$$\Delta S_{total} \geq 0, \tag{B.2}$$

meaning that the total entropy of the system can only increase in the case of irreversible processes or remain constant if a reversible process is implied.

B.2 Principle of Minimum Energy

The principle of minimum energy is basically a reformulation of the second law of thermodynamics. It implies that the internal energy of a closed system, with constant external parameters and entropy, is minimal at equilibrium [128].

In thermodynamics, equilibrium is considered to be a state in which entropy is at a maximum. To derive this condition, it is useful to evaluate entropy as a function of internal energy, U,

and other extensive parameters[1] of the system, ϕ_i:

$$S = S(U, \phi_1, \phi_2, ...). \tag{B.3}$$

The first law of thermodynamics, in its differential form, states that internal energy of a closed system can be written as follows [128]:

$$\begin{aligned} dU &= \delta Q_{rev} - \delta W \\ &= TdS - PdV, \end{aligned} \tag{B.4}$$

where W is the amount of work done by the system, P is the pressure and dV is the infinitesimal change in volume.

By using the definition of S as stated in **Equation B.3**, we can evaluate S as a function of U and ϕ using the first law of thermodynamics [128]:

$$dS = \left(\frac{\partial S}{\partial U}\right)_{\phi} dU + \left(\frac{\partial S}{\partial \phi}\right)_{U} d\phi. \tag{B.5}$$

At equilibrium, U is constant [189], meaning that the first term of **Equation B.5** disappears. In addition, S is at an extremum at equilibrium [189], which mathematically means the following:

$$\left(\frac{\partial S}{\partial \phi}\right)_{U} = 0. \tag{B.6}$$

To evaluate whether this extremum is a maximum or a minimum, the second derivative of **Equation B.6** has to be considered. Based on the second law of thermodynamics, S can only increase or remain constant, meaning that this extremum is a maximum [189]:

$$\left(\frac{\partial^2 S}{\partial \phi^2}\right)_{U} < 0. \tag{B.7}$$

Using the same analogy, the extremum of U can be considered by using the properties of an exact differential [189]:

$$\left(\frac{\partial U}{\partial \phi}\right)_{S} = -\frac{\left(\frac{\partial S}{\partial \phi}\right)_{U}}{\left(\frac{\partial S}{\partial U}\right)_{\phi}} = 0. \tag{B.8}$$

[1] In thermodynamics, an extensive parameter is a property of a system which depends on the size of the system, *e.g.* volume, mass, energy. This means that if you combine or reduce the size of such a system, its extensive parameters will vary accordingly.

By definition:

$$\frac{1}{T} = \left(\frac{\partial S}{\partial U}\right)_{\phi}, \tag{B.9}$$

which means that **Equation B.8** can be rewritten as follows:

$$\left(\frac{\partial U}{\partial \phi}\right)_{S} = -T\left(\frac{\partial S}{\partial \phi}\right)_{U} = 0, \tag{B.10}$$

which shows that U is at an extremum at equilibrium. We can now evaluate its second derivative:

$$\left(\frac{\partial^2 U}{\partial \phi^2}\right)_{S} = -T\left(\frac{\partial^2 S}{\partial \phi^2}\right)_{U}. \tag{B.11}$$

Using **Equation B.7**, we can thus write the following:

$$\left(\frac{\partial^2 U}{\partial \phi^2}\right)_{S} > 0, \tag{B.12}$$

which mathematically constitutes that U is at its minimum at equilibrium [189].

B.3 Surface Tension and Geometrical Surface Energy Minimisation

The principle of minimal energy, which stems from the second law of thermodynamics, states that a system will adjust itself to minimise its total energy. This can be applied in fluid mechanics to explain the formation of shapes that minimise the surface area for a given volume, as reducing the surface area decreases the surface energy.

When a liquid droplet is formed, the system's natural response is to achieve greater stability with a state of lower energy. At the interface of a droplet, molecules are not surrounded equally from all sides as they are inside of the droplet (see **Figure 3.3**). This creates an imbalance in the overall forces of the system and an inward pull towards the centre of the droplet, known as *surface tension*. The surface of the droplet is subjected to contractions until a perfectly spherical shape is achieved, which represents a configuration with the lowest energy associated with the surface of the liquid:

$$E_{surface} = \gamma A, \tag{B.13}$$

where γ is the surface tension and A is the surface area of the liquid.

The spherical shape gives the smallest surface energy, $E_{surface}$, to the system out of any other given shapes [190]. This can be demonstrated analytically by comparing the surface area of a sphere with that of any other geometrical shape for a given volume. For a sphere of a radius r, its volume is given by:

$$V_{sphere} = \frac{4}{3}\pi r^3, \tag{B.14}$$

which gives the following surface area:

$$A_{sphere} = 4\pi r^2. \tag{B.15}$$

If we express the radius, r, from **Equation B.14** and substitute it into **Equation B.15**, the following can be obtained:

$$\begin{aligned} A_{sphere} &= 4\pi \left(\frac{3V}{4\pi}\right)^{\frac{2}{3}} \\ &= \left(\frac{9}{2\sqrt{\pi}}\right)^{\frac{1}{3}} V^{\frac{2}{3}} \\ &\approx 1.36V^{\frac{2}{3}} \end{aligned} \tag{B.16}$$

In comparison, for a cube with an edge length a, its volume is given by:

$$V_{cube} = a^3, \tag{B.17}$$

which yields the following surface area:

$$A_{cube} = 6a^2 = 6V^{\frac{2}{3}}. \tag{B.18}$$

Therefore, $A_{sphere} < A_{cube}$ if the volumes of a sphere and cube are both equal. This means a sphere will yield lower surface energy than a cube, providing more stability to the system.

Note that the same analogy can be applied to any other geometrical shape; the surface-area-to-volume ratio will always be the smallest for a sphere [190].

Appendix C

Supplementary Material for Chapter 4

C.1 Applied Flow Pressures for the FMN−$AscH_2$ Model System

The applied flow pressures using the Elveflow OB1 pressure flow controller during the MARY experiment for the first 22 hours of the experiment are reported in **Figure C.1** and **Table C.1**. The flow rates were recorded using the Elveflow software. Experimental results show a stable pressure output throughout the experiment. It is, therefore, possible to assume that microdroplets are flowed at constant speed once produced inside the microchannel.

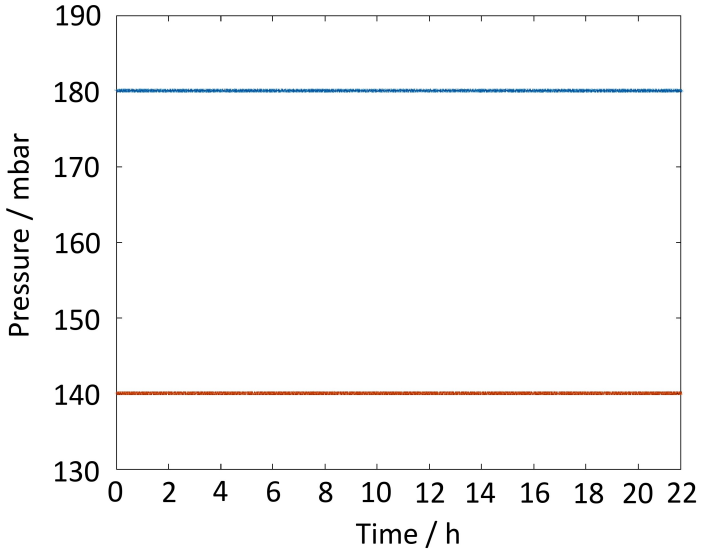


Figure C.1 Applied pressures to the dispersed (orange) and carrier (blue) phases, recorded for the first 22 hours of the MARY experiment on FMN−$AscH_2$ microdroplets.

Phase	Applied flow pressure / mbar
Dispersed	139.85 ± 0.03
Carrier	179.53 ± 0.04

Table C.1 Experimental results of the averaged applied flow rates for FMN−$AscH_2$.

C.2 Fluorescence Spectra of RF−TrpH Model System

To evaluate whether the RF−TrpH model system fluoresces more than the COC polymer that the experimentally used flow-focusing microfluidic chip is made of, a fluorescence emission spectrum was recorded using a spectrograph. Initial illumination of the RF−TrpH system in microdroplets revealed a spike at 513 nm (shown in **Figure C.2a**), which was attributed to the fluorescence of COC polymer present in the microfluidic chip. The same issue was identified for the FMN−$AscH_2$ (see **Section 4.2.4**) but not the F−AH_2^+ model systems. Comparing **Figures C.2** and **4.6** with **Figure 4.2** for the RF−TrpH, FMN−$AscH_2$ and F−AH_2^+ model systems, respectively, it is possible to distinguish experimentally that FAD provides considerably more counts of fluorescence emission than the two other systems, which is why the fluorescence of the COC polymer inside the microfluidic chip did not impact the experimental acquisition of data for F−AH_2^+. Hence, the application of a 550 nm long-pass filter was necessary to remove the emission resulting from the COC polymer for the RF−TrpH system. Once microdroplets were reilluminated, a peak at 560 nm was revealed (see **Figure C.2b**), aligning with the points presented in **Section 4.2.4**.

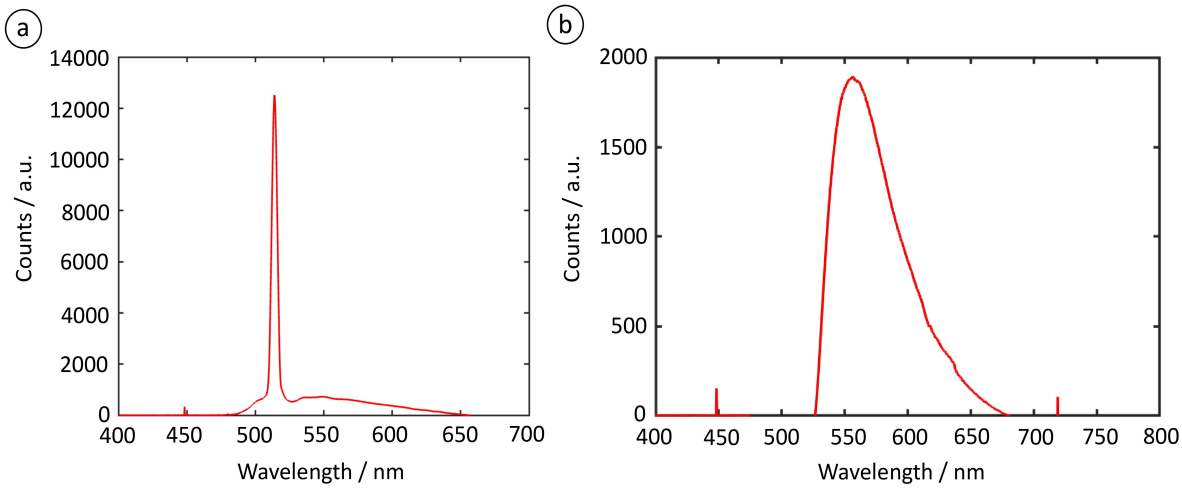


Figure C.2 (a) Fluorescence spectra of RF and Trp with the emission of the microfluidic chip (spike at 513 nm), identical to the one depicted in **Figure 4.6a**. (b) RF and Trp fluorescence peaking at 560 nm with the microfluidic chip signal removed by a 550 nm long-pass filter.

Appendix D

Poster for the Conference "Lab-on-a-Chip and Microfluidics Asia 2023"

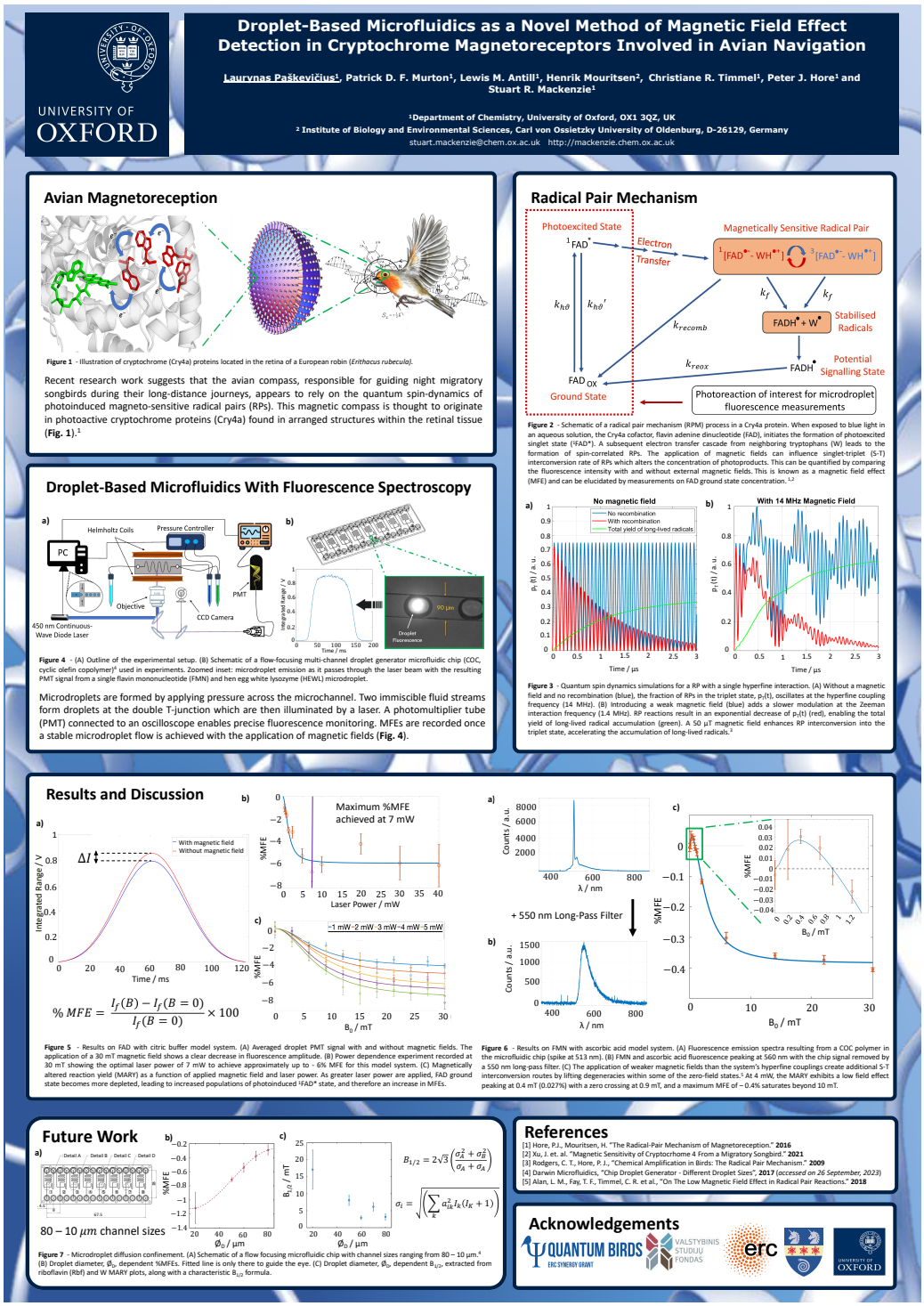


Figure 1 - Illustration of cryptochrome (Cry4a) proteins located in the retina of a European robin (*Erithacus rubecula*).

Figure 2 - Schematic of a radical pair mechanism (RPM) process in a Cry4a protein. When exposed to blue light in an aqueous solution, the Cry4a cofactor, flavin adenine dinucleotide (FAD), initiates the formation of photoexcited singlet state (^{1}FAD*). A subsequent electron transfer cascade from neighboring tryptophans (W) leads to the formation of spin-correlated RPs. The application of magnetic fields can influence singlet-triplet (S-T) interconversion rate of RPs which alters the concentration of photoproducts. This can be quantified by comparing the fluorescence intensity with and without external magnetic fields. This is known as a magnetic field effect (MFE) and can be elucidated by measurements on FAD ground state concentration.[1,2]

Figure 3 - Quantum spin dynamics simulations for a RP with a single hyperfine interaction. (A) Without a magnetic field and no recombination (blue), the fraction of RPs in the triplet state, $p_T(t)$, oscillates at the hyperfine coupling frequency (14 MHz). (B) Introducing a weak magnetic field (blue) adds a slower modulation at the Zeeman interaction frequency (1.4 MHz). RP reactions result in an exponential decrease of $p_T(t)$ (red), enabling the total yield of long-lived radical accumulation (green). A 50 μT magnetic field enhances RP interconversion into the triplet state, accelerating the accumulation of long-lived radicals.[3]

Figure 4 - (A) Outline of the experimental setup. (B) Schematic of a flow-focusing multi-channel droplet generator microfluidic chip (COC, cyclic olefin copolymer)[4] used in experiments. Zoomed inset: microdroplet emission as it passes through the laser beam with the resulting PMT signal from a single flavin mononucleotide (FMN) and hen egg white lysozyme (HEWL) microdroplet.

Figure 5 - Results on FAD with citric buffer model system. (A) Averaged droplet PMT signal with and without magnetic fields. The application of a 30 mT magnetic field shows a clear decrease in fluorescence amplitude. (B) Power dependence experiment recorded at 30 mT showing the optimal laser power of 7 mW to achieve approximately up to - 6% MFE for this model system. (C) Magnetically altered reaction yield (MARY) as a function of applied magnetic field and laser power. As greater laser power are applied, FAD ground state becomes more depleted, leading to increased populations of photoinduced ^{1}FAD* state, and therefore an increase in MFEs.

$$\%MFE = \frac{I_f(B) - I_f(B=0)}{I_f(B=0)} \times 100$$

Figure 6 - Results on FMN with ascorbic acid model system. (A) Fluorescence emission spectra resulting from a COC polymer in the microfluidic chip (spike at 513 nm). (B) FMN and ascorbic acid fluorescence peaking at 560 nm with the chip signal removed by a 550 nm long-pass filter. (C) The application of weaker magnetic fields than the system's hyperfine couplings create additional S-T interconversion routes by lifting degeneracies within some of the zero-field states.[5] At 4 mW, the MARY exhibits a low field effect peaking at 0.4 mT (0.027%) with a zero crossing at 0.9 mT, and a maximum MFE of – 0.4% saturates beyond 10 mT.

Figure 7 - Microdroplet diffusion confinement. (A) Schematic of a flow focusing microfluidic chip with channel sizes ranging from 80 – 10 μm.[4] (B) Droplet diameter, $\emptyset_D$, dependent %MFEs. Fitted line is only there to guide the eye. (C) Droplet diameter, $\emptyset_D$, dependent $B_{1/2}$, extracted from riboflavin (Rbf) and W MARY plots, along with a characteristic $B_{1/2}$ formula.

$$B_{1/2} = 2\sqrt{3}\left(\frac{\sigma_A^2 + \sigma_B^2}{\sigma_A + \sigma_A}\right)$$

$$\sigma_i = \sqrt{\left(\sum_k a_{ik}^2 I_k (I_k + 1)\right)}$$

Appendix E

Poster for the Conference "18th Symposium on Magnetic Field and Spin Effects in Chemistry and Related Phenomena"

